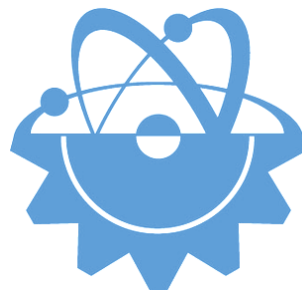


ISSN-Printed: 2536-5010
ISSN-Online: 2536-5134

Volume 8, No 2, 2018

EJT

EUROPEAN JOURNAL OF TECHNIC



Copyright © 2017

International Engineering, Science & Education Group

Email (for orders and customer services enquiries): info@ineseg.org, ejt@ineseg.org

Visit our home page on www.ineseg.org

All Rights Reserved. No part of this publication may be reproduced, stored in a retrieval system or transmitted in any form or by any means, electronic, mechanical, photocopying, recording, scanning or otherwise, except under the terms of the Copyright, under the terms of a license issued by the Copyright International Engineering, Science & Education Group (INESEG), without the permission in writing of the Publisher. Requests to the Publisher should be addressed to the Permissions Department, International Engineering, Science & Education Group (INESEG), or emailed to info@ineseg.org

Designations used by companies to distinguish their products are often claimed as trademarks. All brand names and product names used in this journal are trade names, service marks, trademarks or registered trademarks of their respective owners. The Publisher is not associated with any product or vendor mentioned in this journal.

This publication is designed to provide accurate and authoritative information in regard to the subject matter covered. It is sold on the understanding that the Publisher is not engaged in rendering professional services. If professional advice or other expert assistance is required, the services of a competent professional should be sought.



EUROPEAN JOURNAL OF TECHNIQUE (EJT)

ISSN-Printed: 2536-5010

ISSN-Online: 2536-5134

Scope: European Journal of Technique (EJT) established in 2010. It is a peer –reviewed international journal to be of interest and use to all those concerned with research in various fields of, or closely related to, Engineering disciplines. European Journal of Technique (EJT) aims to provide a highly readable and valuable addition to the literature which will serve as an indispensable reference tool for years to come. The coverage of the journal includes all new theoretical and experimental findings in the fields of Engineering or any closely related fields. The journal also encourages the submission of critical review articles covering advances in recent research of such fields as well as technical notes.

The scopes include:

- Mechanical Engineering
- Textile Engineering
- Electrical-Electronics Engineering
- Computer and Informatics Engineering
- Civil and Architecture Engineering
- Mining Engineering
- Chemical Engineering
- Metallurgical and Materials Engineering
- Environmental Engineering
- Food Engineering
- Geological Engineering
- Industrial Engineering
- Renewable Energy

EDITORIAL BOARD MEMBERS

Editor-in-Chief

- Musa YILMAZ

Publisher Of Journal

- Heybet KILIÇ

ETHICS and POLICIES

European Journal of Technique (EJT) is committed to following the [Code of Conduct](#) and [Best Practice Guidelines](#) of COPE (Committee on Publication Ethics). It is a duty of our editors to follow [Cope Guidance for Editors](#) and our peer-reviewers must follow [COPE Ethical Guidelines for Peer Reviewers](#). We expect all prospective authors to read and understand our Ethics Policy before submitting any manuscripts to our journals.

Please note that submitted manuscripts may be subject to checks using the iThenticate service, in conjunction with CrossCheck, in order to detect instances of overlapping and similar text.

The [iThenticate](#) software checks submissions against millions of published research papers, documents on the web, and other relevant sources. If plagiarism or misconduct is found, consequences are detailed in the policy.

The chief goal of our policy is threefold: to provide advice for our authors, to maintain the scholarly integrity of our journals and their content, and to detail the ethical responsibilities of EJT, our editors and authors.

We expect all authors to read and understand our ethics policy before submitting to any of our journals. This is in accordance with our commitment to the prevention of ethical misconduct, which we recognise to be a growing problem in academic and professional publications. It is important to note that most incidents of plagiarism, redundant publication, copyright infringement or similar occur because of a lack of understanding, and not through fraudulent intent. Our policy is one of prevention and not persecution.

If you have any questions, please contact the relevant editorial office, or European Journal of Technique (EJT)' ethics representative: ejtineseg@gmail.com

Download a PDF version of the Ethics and Policies [PDF,392KB].

Authors' Responsibilities

Authors should:

- Ensure that all researched work submitted is original, fully referenced and that all authors are represented accurately. The submission must be exclusive and not under consideration elsewhere.
- Provide accurate contact details for a designated corresponding author, who shall be deemed by the publisher and editor as fully responsible for the authorship of the paper and all communications concerning the ethical status and originality of the paper. This includes any queries or investigations that may arise, pre- or post publication.
- Openly disclose the source of all data and third party material, including previously unpublished work by the authors themselves. Anything that could compromise the originality of the submission should be expressly avoided and/or discussed with the editorial office in the first instance.
- Identify any third party material that they intend to include in their article, and obtain written permission for re-use in each instance from the relevant copyright holders. Such permissions should be submitted once the manuscript is accepted, or requires small changes to be accepted. For further guidance on seeking permission to use 3rd party material please see the Rights and Permissions section.
- Openly disclose any conflict of interest - for example, if publication were to benefit a company or services in which the author(s) has a vested interest.

- Expect to formally agree publication terms which defines the author and the publishers rights for the work. Visit our website for further information.
- Expect the editor to scan submissions using plagiarism detection software at [iThenticate](#) to check a paper's originality before sending out for review.
- Fully correspond and comply with the editor and publisher in any requests for source data, proof of authorship or originality in a timely manner, providing reasonable explanation for discrepancies or failures to disclose vital information.
- Fully co-operate with any consequent investigations if the editor and/or publisher are dissatisfied with the evidence available or the explanations provided.
- Expect transparency, efficiency and respect from the publisher and the editor during the submissions process.
- Remain in good communication with both the publisher and the editor.
- When necessary, submit corrigenda in a timely and responsible fashion.
- Co-operate fully with the publication of errata and with the retraction of articles found to be unethical, misleading or damaging.
- Remain in good communication with the editor(s), the publisher and any co-authors.

Editors' Responsibilities

Editors should:

- Read and understand COPE guidelines as well as EJT's ethics policy, and follow them during all editorial processes.
- Protect the reputation of their journal(s) and published work by only publishing content of the highest quality and relevance in a timely and responsible manner.
- Carry out thorough, objective and confidential peer review for original article submissions that pass the initial quality check and editorial assessment, in adherence with COPE guidelines and EJT' ethics policy.
- Detail and justify any article types which will not be peer reviewed (e.g. editorials, opinion pieces etc.).
- Provide a transparent review and publication process as far as is possible, with full respect and care paid to the author(s).
- Provide advice and give reasonable explanation and updates to authors during the submissions process and once a decision has been made.
- Allow authors the right to appeal any editorial decision.
- Only accept papers based on the original merit, quality and relevance of their content.
- Support authors in queries concerning the originality of their submissions and request the support of EJT if necessary.
- Advise the publisher of any third party material which has been included for which they do not believe sufficient permission has been cleared.

- Be ready and prepared to publish corrections, corrigenda, errata when necessary, as well as retract articles that (the editor and EJT) deem unethical, misleading or damaging.
- Remain in good communication with both the publisher and the author(s).

Reviewers' Responsibilities

Reviewers should:

- Adhere to EJT's policy of confidential peer review of their journals. This includes, but is not restricted to, keeping their identity hidden from authors and not externally distributing any work that is passed to them for their eyes only.
- Only accept invitations to review work that is relevant to their own expertise and speciality.
- Review submitted work in a responsible, impartial and timely manner.
- Report any suspected ethical misconduct as part of a thorough and honest review of the work.
- Avoid the use of unnecessarily inflammatory or offensive language in their appraisal of the work.
- Accept the commitment to review future versions of the work and provide 'follow up' advice to the editor(s), if requested.
- Seek advice from the editor if anything is unclear at the time of invitation.
- Remain in good communication with both the publisher and the editor.

EJT's Responsibilities

EJT will:

- Protect the reputation of our journals and published work by only publishing content of the highest quality and relevance in a timely and responsible manner.
- Provide detailed information concerning both our understanding of publication ethics and our implementation of the same. Emphasise a desire for prevention, not eventual detection, of ethical misconduct.
- Uphold our COPE membership (or of such similar organisations) and keep our editorial offices, publishing staff and society partners up-to-date with their guidelines and policies, adapting our own where appropriate (and publicising any update).
- When necessary, request proof of originality/accuracy from the corresponding author of any work submitted to any of our journals.
- Use plagiarism detection software when necessary for any submission to any journal at any stage of the submissions and publication process.
- Provide a transparent submissions and publication process, with full respect and care paid to the author. This includes detailed and dedicated instructions to authors for each journal, outlining referencing style, accepted article types and submission processes.
- Investigate thoroughly any suggestion of ethical misconduct detected during any stage of the submissions process. This can include, but is not restricted to, the following: plagiarism, redundant publication, fabrication or misuse of data and authorial disputes.

- When necessary, retract articles that we deem to be unethical, misleading or damaging.
- When necessary, publish errata, corrigenda and retractions in a timely and responsible fashion, detailing the decision online in an open access format and publishing in print as soon as possible.
- Remain in good communication with editors, authors, reviewers and society partners (where applicable).

Further reading

- Authorship of the paper: Authorship should be limited to those who have made a significant contribution to the conception, design, execution, or interpretation of the reported study.
- Originality and plagiarism: The authors should ensure that they have written entirely original works, and if the authors have used the work and/or words of others that this has been appropriately cited or quoted.
- Data access and retention: Authors may be asked to provide the raw data in connection with a paper for editorial review, and should be prepared to provide public access to such data.
- Multiple, redundant or concurrent publication: An author should not in general publish manuscripts describing essentially the same research in more than one journal or primary publication. EJT do not view the following uses of a work as prior publication: publication in the form of an abstract; publication as an academic thesis; publication as an electronic preprint. Information on prior publication is included within each EJT and its journal Guideline for Authors.
- Acknowledgement of sources: Proper acknowledgment.
- Disclosure and conflicts of interest: All submissions must include disclosure of all relationships that could be viewed as presenting a potential conflict of interest.
- Fundamental errors in published works: When an author discovers a significant error or inaccuracy in his/her own published work, it is the author's obligation to promptly notify the journal editor or publisher and cooperate with the editor to retract or correct the paper.
- Reporting standards: Authors of reports of original research should present an accurate account of the work performed as well as an objective discussion of its significance.
- Hazards and human or animal subjects: Statements of compliance are required if the work involves chemicals, procedures or equipment that have any unusual hazards inherent in their use, or if it involves the use of animal or human subjects.
- Use of patient images or case details: Studies on patients or volunteers require ethics committee approval and informed consent, which should be documented in the paper.

EJT has also accessed and learned from the existing policies of other publishers and leading experts as well as open access articles that detail and define ethical misconduct.

- 'Plagiarism and the law', Joss Saunders, Learned Publishing, 23:279-202: <http://www.ingentaconnect.com/content/alpsp/lp/2010/00000023/00000004/art00002>
- iThenticate Plagiarism Resources: <http://www.ithenticate.com/resources/6-consequences-of-plagiarism>

EDITORIAL BOARD MEMBERS

Editor-in-Chief : Musa Yilmaz

International Editorial Board

Aayush Shrivastava	University of Petroleum and Energy Studies, Dehradun
Adelino Pereira	Engineering Institute of Coimbra, Portugal.
Ahmad Fakharian	Islamic Azad University, Qazvin, Iran
Ahmed Saber	Cairo University, Egypt
Arvind Kumar Jain	Rustam Ji Institute of Technology, India
Aydogan Ozdemir	Istanbul Technical University
Baseem Khan	Hawassa University, Hawassa, Ethiopia
Behnam Mohammadi-ivatloo	University of Tabriz, Tabriz, Iran
Bharti Dwivedi	Electrical Eng, Institute of Eng & Technology, Lucknow, UP, India
Carlos A. Castro	University of Campinas – UNICAMP
Deepak Kumar	University of Petroleum & Energy Studies (UPES)
Ernesto Vazquez	University of Nuevo Leon, Mexico
Faisal Khan	COMSATS Institute of Information Technology, Pakistan
Farhad Shahnia	Murdoch University, Perth, Australia
Farrokh Aminifar	University of Tehran
Fiaz Ahmad	National University of Computer and Emerging Sciences Pakistan
Gouthamkumar Nadakuditi	V R Siddhartha Engineering College Vijayawada, India
Hafiz Ahmed	Aerospace and Automotive Eng, Coventry Univ, United Kingdom.
Hamed Pourgharibshahi	Lamar University, USA
Hassan Bevrani	University of Kurdistan, Iran
Hemant Kumar Gianey	Thapar University, Patiala, Punjab, India
Hessam Golmohamadi	Semnan University, Semnan, Iran
Hilmy Awad	Helwan University, Cairo, Egypt.
Jamshed Ahmed Ansari	Sukkur IBA University Pakistan
José A. Dominguez-Navarro	University of Zaragoza, Spain.
Kalpana Chauhan	Galgotias College of Engineering and Technology Greater Noida, India
Khaled Ellithy	Qatar University, Doha, Qatar
Kim-Doang Nguyen	South Dakota State University, USA
Kundan Kumar	KIIT University, India
Lalit Kumar	GBPIET Pauri, India
Linquan Bai	ABB Inc. (USA)
Linquan Bai	Consulting Engineer at ABB Inc. (USA)
Md Shafiullah	King Fahd University of Petroleum & Minerals, SA
Mohammed Albadi	Sultan Qaboos University, Oman
Mohammed Albadi	Sultan Qaboos University, Oman
Mohd Tariq	Aligarh Muslim University
Mousa Marzband	Northumbria Univ, Newcastle upon Tyne, NE1 8ST, United Kingdom
Neeraj Kanwar	Manipal University Jaipur, India
Nishant Kumar	Indian Institute of Technology Delhi, New Delhi
Nitin Kumar Saxena	Wolaita Sodo University Ethiopia
Omar Hafez	Umm Al-Qura University, Makkah, Saudi Arabia
Omveer Singh	Gautam Buddha University, India
Payam Teimourzadeh Baboli	University of Mazandaran (UMZ), Iran
Payman Dehghanian	George Washington University, USA
Ragab A. El Sehiemy	Kafrelsheikh Univrsity, Egypt
Rajiv Singh	G.B. Pant University of Agriculture & Technology, Uttarakhand, India
Reza Sharifi	Amir Kabir university Tehran, Iran
Rudranarayan Senapati	Kalinga Institute of Industrial Technology, India
Saleh Y. Abujarad	Universiti Teknologi Malaysia
Sanjay Dambhare	Department of Electrical Engineering College of Engineering, INDIA
Saptarshi Roy	NIT Warangal, India
Shailendra Kumar	Indian Institute of Technology Delhi, India
Shailendra Kumar	Indian Institute of Technology Delhi
Shariq Riaz	The University of Sydney, Australia
Shengen Chen	University of Maine, USA
Syafaruddin	Universitas Hasanuddin, Indonesia
T. Sudhakar Babu	VIT University, Vellore, India
Thamer Alquthami	King Abdulaziz University
Theofilos Papadopoulos	Democritus University of Thrace, Greece
Uday P. Mhaskar	CSA Group, USA
Yogesh Rohilla	K Lakshmi Pat University, Jaipur, India
Yunfeng Wen	School of Electrical Engineering, Chongqing University, China
Zbigniew M. Leonowicz	Wroclaw University of Sci and Tech, Politechnika Wroclawska, Poland



CONTENTS

MATHEMATICAL MODELS TO DETERMINE OF THIN LAYER DRYING KINETIC OF GINGER SLICES	110 - 123
MECHANICAL PROPERTIES OF THE COMPOSITE MATERIAL PRODUCED BY THE MIXTURE OF EXPANDED PERLITE, WASTE MARBLE DUST AND TRAGACANTH	124 - 133
INVESTIGATION OF EXTERNAL BONDED PATCH REPAIR OF LAMINATED COMPOSITE MATERIALS EXPERIMENTALY	134 - 140
DYNAMIC MODEL AND CONTROL OF 2-DOF ROBOTIC ARM	141 - 150
COMPARATIVE PERFORMANCE ANALYSIS OF PHASE DIVISION MULTIPLEXING TECHNIQUES	151 - 159
ENERGY POTENTIAL OF ANIMAL BIOMASS IN TURKEY	160 - 167
TRIANGLE FUZZY TRANSFORM BASED AUTOMATIC NOISE AND COLOR IMAGE REDUCTION METHODS	168 - 178
CLASSIFICATION OF AMYOTROPHIC LATERAL SCLEROSIS AND HEALTHY ELECTROMYOGRAPHY SIGNALS BASED ON TRANSFER LEARNING	179 - 185
RECOGNITION OF IRREGULARLY SHAPED WORDS BY USING FRACTAL DIMENSION	186 - 195
NEW SWARM INTELLIGENCE BASED OPTIMIZATION ALGORITHMS FOR THE OPTIMIZATION OF MICROGRIDS	196 - 208



MATHEMATICAL MODELS TO DETERMINE OF THIN LAYER DRYING KINETIC OF GINGER SLICES

*Ebru KAVAK AKPINAR**, *Seda DEMİRCİ*

Mechanical Engineering Department, Firat University, 23279, Elazig, Turkey

*Corresponding author; E-mail: ebruakpinar@firat.edu.tr

Received: 25 January 2018; Accepted: 1 March 2018

In the present work, the effects of some parametric values on the thin layer drying process of ginger slices were investigated. Drying was done in the laboratory by using cyclone type convective dryer. The drying air temperature was varied as 40, 50, 60 and 70 °C and the air velocity is 0.8, 1.5 and 3 m/s. All drying experiments had only falling rate period. The drying data were fitted to the twelve mathematical models and performance of these models was investigated by comparing the determination of coefficient (R^2), reduced chi-square (χ^2) and root mean square error (RMSE) between the observed and predicted moisture ratios. Among these models, drying model developed by Midilli et al. model showed good agreement with the data obtained from the experiments. From the Midilli et al. model for ginger slices, R^2 , χ^2 and RMSE were determined between 0.99587 and 0.99971, 0.0006156 and 0.00003721 and, 0.019792 and 0.005597, respectively. Using regression analysis, the relationship between the coefficients of Midilli et al. model with drying air temperature and velocity was investigated.

Key Words: *Ginger, Drying kinetic, Thin layer drying, Mathematical models, Regression analysis*

1. Introduction

Fresh ginger is rich in oleoresins, a volatile antioxidant that has wide use in food as well as medicines. Similarly, dried ginger has also wide use as spice and medicine, thus has a potential for domestic and export market. Therefore, drying of ginger needs special attention to preserve the quality in the end product by suitable technique [1].

Drying of materials having high moisture content is a complicated process involving simultaneous heat and mass transfer [2]. The materials are dried by thin layer drying due to faster drying with minimum loss of nutrients. Thin-layer drying describes the process of drying in a single layer of sample particles. Three types of thin-layer drying models are used to describe the drying phenomenon of farm product. The theoretical model considers only the internal resistance to moisture transfer between product and heating air whereas semi-theoretical and empirical models consider only the external resistance [3-4]. Theoretical model needs assumptions of geometry of a typical food, its mass diffusivity and conductivity [5-6]; empirical model neglects the fundamentals of drying process and presents a direct relationship between average moisture and drying time by means of regression analysis [7-8], and semi-theoretical model is a tradeoff between the theoretical and empirical ones, derived from simplification of Fick's second law of diffusion or modification of the simplified model, which are widely used, such as the Lewis, Page, Modified Page, Henderson and Pabis, Logarithmic, Two term, Two term exponential, Diffusion approach, Modified Henderson and Pabis, Verma and Midilli *et al.* models [9-10]. Recently, very little studies have been conducted on the investigation of drying behavior of ginger using different drying methods and systems [1, 11-18]. Determination of drying kinetics and convective heat transfer coefficients of ginger slices was introduced in the literature in a previous work by authors [17-18]. The main objective of this study was to describe the thin layer drying kinetics of ginger at each experimental condition, using twelve empirical models. Relations between experimental conditions with coefficients of the selected model were to investigate.

2. Material and methods

2.1. Experimental set up

Figure 1 illustrates the schematic diagram of the cyclone type dryer, developed for experimental work [19]. The system was introduced in the literature [20]. Briefly, it consists of fan, resistance and heating control systems, air-duct, drying chamber in cyclone type, and measurement instruments.

In the measurements of temperatures, J type iron-constantan thermocouples were used with a manually controlled 20-channel automatic digital thermometer (Elimko 6400, Ankara, Turkey), with reading accuracy of ± 0.1 °C. A thermo hygrometer (Extech 444731, Shenzhen, China) was used to measure humidity levels at various locations in the system. Moisture loss was recorded at 20-minute intervals during drying by means of a digital balance (Bel, Mark 3100, Monza, Italy) an accuracy of ± 0.01 g (Fig. 1).

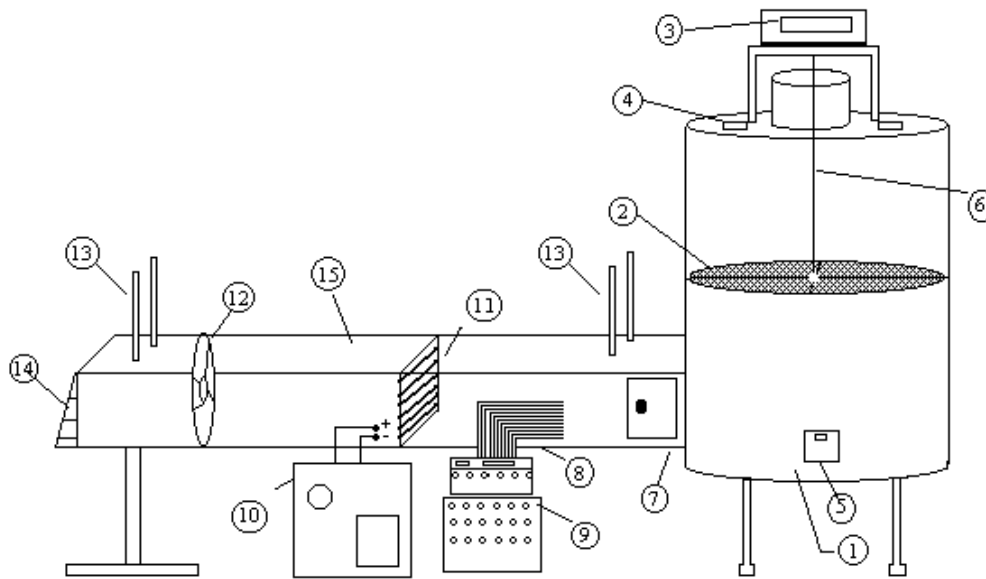


Figure 1. Experimental set-up (1- drying chamber, 2- tray, 3- digital balance, 4- observation windows, 5- digital thermometer, 6-the balance suspension bar, 7- control panel, 8- thermocouples, 9- digital thermometer and channel selector, 10-rheostat, 11- heater, 12- fan, 13- wet and dry thermometers, 14- adjustable flap, 15- duct)

2.2. Experimental procedure

Fresh ginger slices were used in the experiments. Before the drying process, the gingers were cut into slices of 4 mm thickness and 30 mm in diameter with a mechanical cutter. After the dryer had reached steady state temperature conditions for operation, 150 g ginger slices are put on the tray of dryer and dried there. The initial and final moisture contents of the ginger slices were determined at 80 °C using an infrared moisture analyzer (Mettler LJ16, Greifensee, Switzerland).

Drying experiments were carried out at 40, 50, 60, and 70°C drying air temperatures and 0.8, 1.5 and 3 m/s air velocities. Drying was continued until the average final moisture content (0.06 g water/g dry matter) from the average initial moisture content (4.8 g water/g dry matter). During the experiments, ambient temperature and relative humidity, and the inlet and outlet temperatures of the drying air in the dryer chamber were recorded.

2.3. Mathematical modelling of drying curves

The moisture ratio (MR) of the ginger slices during the thin layer drying experiments was calculated using the following equation:

$$MR = \frac{M_t - M_e}{M_o - M_e} \quad (1)$$

where M_t , M_o and M_e are the anytime, the initial and equilibrium moisture contents (% dry basis) respectively [21].

Table 1. Thin layer drying curve models for the variation of moisture ratio (MR) with time (t)

Model no	Model name	Model	References
1	Newton	$MR = \exp(-kt)$	[22]
2	Page	$MR = \exp(-kt^n)$	[23]
3	Modified Page	$MR = \exp[-(kt)^n]$	[24]
4	Henderson and Pabis	$MR = a.\exp(-kt)$	[25]
5	Logarithmic	$MR = a.\exp(-kt)+c$	[26]
6	Two term	$MR = a\exp(-k_o t)+b\exp(-k_1 t)$	[27]
7	Two-term exponential	$MR = a\exp(-k t)+(1-a)\exp(-k a t)$	[28]
8	Wang and Singh	$MR = 1 + at + bt^2$	[8]
9	Diffusion approach	$MR = a\exp(-kt)+(1-a)\exp(-k b t)$	[26]
10	Modified Henderson and Pabis	$MR = a\exp(-kt)+b\exp(-g t)+c\exp(-ht)$	[29]
11	Verma <i>et al.</i>	$MR = a\exp(-kt)+(1-a)\exp(-g t)$	[30]
12	Midilli <i>et al.</i>	$MR = a.\exp(-kt^n) + bt$	[3]

The experimental moisture ratio data of ginger obtained were fitted to the 12 commonly used thin-layer drying models in Tab. 1 [8, 22-30]. Non-linear least square regression analysis was performed using Levenberg-Marquardt procedure in Statistica 6.0 computer program. The goodness of fit of the selected mathematical models to the experimental data was evaluated with the correlation coefficient (R^2), the reduced chi-square (χ^2) and the root mean square error (RMSE). The goodness of fit will be better, if R^2 values are higher and χ^2 and RMSE values are lower. These can be calculated as:

$$R^2 = \frac{\sum_{i=1}^n (MR_i - MR_{pre,i}) \cdot \sum_{i=1}^n (MR_i - MR_{exp,i})}{\sqrt{\left[\sum_{i=1}^n (MR_i - MR_{pre,i})^2 \right] \cdot \left[\sum_{i=1}^n (MR_i - MR_{exp,i})^2 \right]}} \quad (2)$$

$$\chi^2 = \frac{\sum_{i=1}^n (MR_{exp,i} - MR_{pre,i})^2}{N - n} \quad (3)$$

$$RMSE = \left[\frac{1}{N} \sum_{i=1}^N (MR_{pre,i} - MR_{exp,i})^2 \right]^{1/2} \quad (4)$$

where, $MR_{exp,i}$ is the i th experimentally observed moisture ratio, $MR_{pre,i}$ the i th predicted moisture ratio, N the number of observations and n is the number constants [7, 31, 32].

3. Results and discussion

The times to reach the final moisture content from the initial moisture content at the various drying air temperature and velocity of the ginger slices were found to be between 8700 and 24900 seconds. The temperature is the major effect on the drying process, and, air velocity has less important effect on the drying of ginger slices. In order to normalize the drying curves, the data involving dry basis moisture content versus time were transformed to a dimensionless parameter called as moisture ratio versus time (Fig. 2). The moisture content data at the different experimental mode were converted to the most useful moisture ratio expression and then curve fitting computations with the drying time were carried on the 12 drying models evaluated by the different researches (Tab. 1). The results of statistical analyses undertaken on these models for the thin layer drying of ginger slices (Tabs. 2-4) were evaluated based on R^2 , χ^2 and $RMSE$. Generally, the R^2 , χ^2 and $RMSE$ values changed between 0.91989 and 0.99971, 0.00003721 and 0.0124073, and 0.005597 and 0.086280, respectively. For the thin layer drying of ginger slices, the Midilli et al. model was the best descriptive model (Tabs. 2-4). From the Midilli *et al.* model for ginger slices, R^2 , χ^2 and $RMSE$ were determined between 0.99587 and 0.99971, 0.0006156 and 0.00003721 and, 0.019792 and 0.005597, respectively. The Midilli et al. model gave a higher R^2 and lower χ^2 , $RMSE$ (Tables 2-4) all the experimental conditions and, thus, was selected to represent the thin layer drying behaviour of the ginger slices. According to the statistical indicators, the worst results were obtained with Page model (all temperature at $V=0.8$ m/s, $T= 70$ °C and 60 °C at $V=1.5$ m/s, $T= 60$ °C at $V=3$ m/s), Wang and Singh model ($V=1.5$ m/s and 3 m/s at $T= 50$ °C), Modified Henderson and Pabis model ($V=1.5$ m/s and 3 m/s at $T= 40$ °C) and Two term model ($T= 70$ °C at $V=3$ m/s).

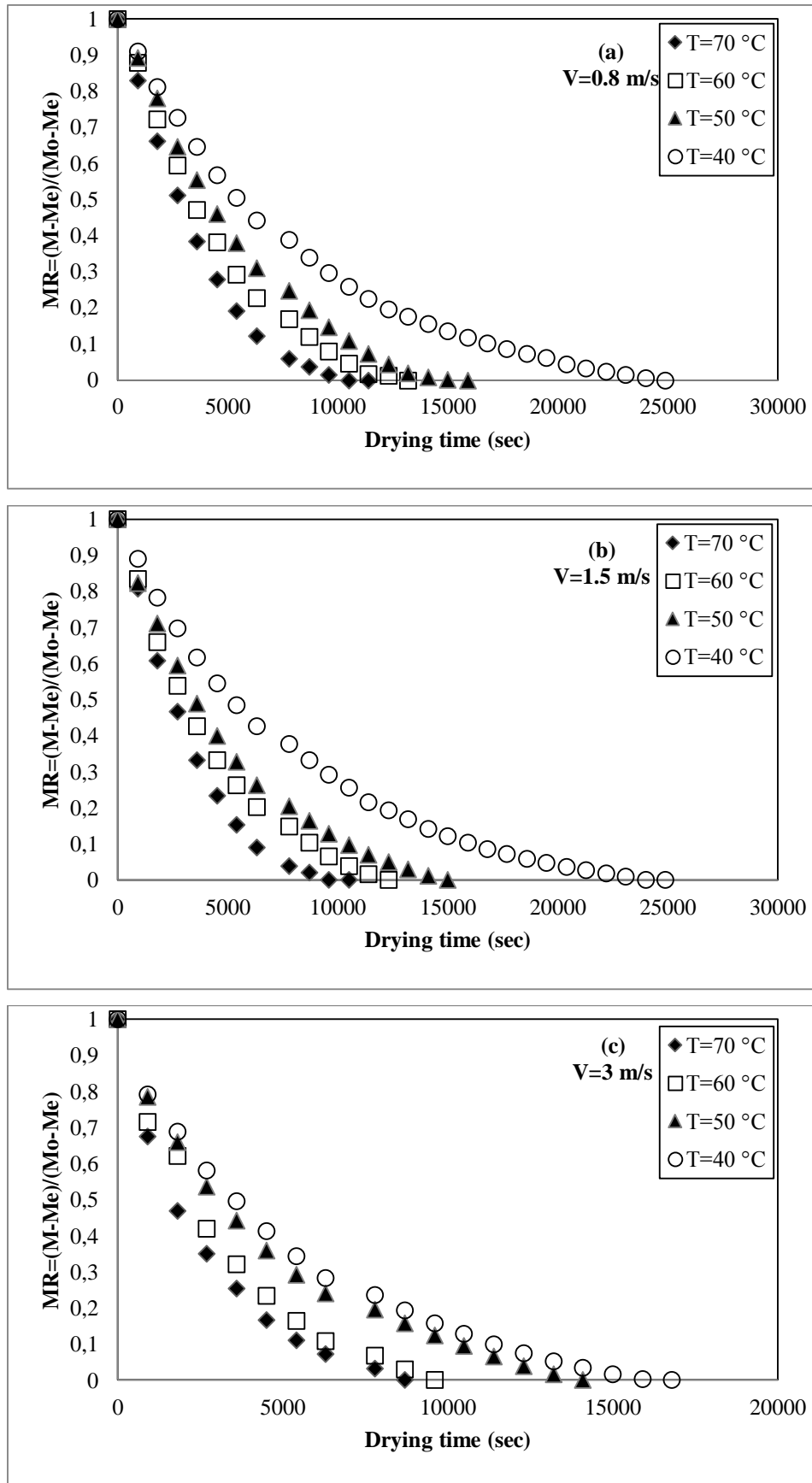


Figure 2. Variation of moisture ratio with drying time at different air temperatures and constant air velocities

The values of the selected model coefficients (a , k , n and b of Midilli *et al.* model) are reported in Tab. 1. The regression analysis was used to set up the relations between these parameters with the temperatures and velocities. Thus, the regression equations of these parameters against drying temperature, T ($^{\circ}\text{C}$) and V (m/s) for accepted model using linear equation are as follows:

$a, k, n, b = f$

$$a = 1.01746 + 0.000916V - 0.00029T \quad R^2 = 0.50 \quad (5)$$

$$k = -0.000220 + 0.000417V - 0.000002T \quad R^2 = 0.82 \quad (6)$$

$$n = 0.887897 - 0.12359V + 0.00624T \quad R^2 = 0.93 \quad (7)$$

$$b = -0.000000497 - 0.00000226V + 1.10^{-19}T \quad R^2 = 0.82 \quad (8)$$

k , n , b coefficients were dependent on drying air temperature and velocity. But, the values of “ a ” coefficient varied between 1.00 and 0.99 at all drying air velocities and temperatures. Therefore, “ a ” coefficient was not affected by drying air velocity and temperature. It remained stable. The R^2 values for k , n , b equations were between 0.82 and 0.93, thus the coefficients of selected model could be calculated using these equations to estimate moisture ratio of ginger.

Validation of the established model was made by comparing the computed moisture contents with the measured moisture contents in any particular drying run under certain conditions. The performance of the model for the thin layer drying of ginger slices was illustrated in Fig. 3. The experimental data are generally banded around the straight line representing data found by computation, which indicates the suitability of the mathematical model in describing drying behavior of ginger slices.



Table 2. Modelling of moisture ratio according to the drying time at 40, 50, 60, and 70 °C drying air temperatures and 3 m/s air velocity

Model no	Constants	V=3 m/s, T=70 °C				V=3 m/s, T=60°C				V=3 m/s, T=50°C				V=3 m/s, T=40°C			
		Constants	R ²	χ ²	RMSE	Constants	R ²	χ ²	RMSE	Constants	R ²	χ ²	RMSE	Constants	R ²	χ ²	RMSE
1	k	0.00041	0.99751	0.0002569	0.015206	0.00033	0.99191	0.0008447	0.027712	0.00023	0.99543	0.0004059	0.01950	0.00019	0.99359	0.0005560	0.022952
2	k n	0.00068 0.93371	0.99697	0.0003515	0.016769	0.000532 0.93976	0.98840	0.0013452	0.033176	0.000582 0.89018	0.99252	0.0007116	0.02495	0.000566 0.88202	0.98968	0.0009482	0.029127
3	k n	0.00041 0.97573	0.99760	0.0002781	0.014918	0.00032 1.08629	0.99362	0.0007399	0.024605	0.00023 0.98961	0.99584	0.0003959	0.01861	0.00020 0.98038	0.99460	0.0004957	0.021060
4	a k	0.99718 0.00041	0.99751	0.0002897	0.015225	1.01479 0.00033	0.99178	0.0009529	0.027922	1.00372 0.00023	0.99559	0.0004199	0.01916	0.98187 0.00020	0.99496	0.0004625	0.020344
5	a k c	0.00244 0.00039 -0.01056	0.99805	0.0002591	0.013469	1.06033 0.00029 -0.05220	0.99539	0.0006020	0.020924	0.99208 0.00025 0.021784	0.99301	0.0007160	0.02411	1.00331 0.00021 0.009205	0.99317	0.000666	0.023689
6	a ko b k ₁	0.428445 0.000215 0.428444 0.00104	0.91989	0.0124073	0.086280	0.300440 0.000313 0.714003 0.000340	0.99186	0.0012133	0.027786	0.590417 0.000247 0.406408 0.000211	0.99568	0.0004793	0.01896	0.670941 0.000199 0.316897 0.000199	0.99509	0.0005111	0.020088
7	a k	0.032905 0.011950	0.99788	0.0002457	0.014020	0.009119 0.035261	0.99169	0.0009636	0.028078	0.025142 0.008855	0.99625	0.0271496	0.15412	0.023351 0.008418	0.99528	0.0004334	0.019693
8	a b	-0.0003 0.00000002	0.97072	0.0034011	0.052162	-0.0002 0.00000001	0.98595	0.0016292	0.036510	-0.0001635 0.000000007	0.97012	0.0003568	0.01766	-0.0001 0.00000001	0.97138	0.0026289	0.048499
9	a k b	0.032908 0.019897 0.019763	0.99788	0.0002808	0.014020	-0.134117 0.001020 0.350979	0.99343	0.0008574	0.024972	0.025943 0.027390 0.008124	0.99625	0.0003841	0.01766	0.024709 0.012465 0.015751	0.99528	0.0004603	0.019690
10	a k b g c h	0.257540 0.001304 0.386343 0.000318 0.386343 0.000318	0.99242	0.0017608	0.026539	-0.151314 0.001232 0.577350 0.000369 0.565309 0.000361	0.99313	0.0014337	0.025528	0.315149 0.000209 0.315149 0.000207 0.315149 0.000209	0.99245	0.0010056	0.02507	0.302676 0.000089 0.305973 0.000485 0.305973 0.000212	0.95450	0.0054654	0.061151
11	a k g	-1.94983 0.000487 0.000457	0.99748	0.0003339	0.015288	-1.83309 0.000447 0.000402	0.99281	0.0009385	0.026126	-2.21304 0.000182 0.000195	0.99596	0.000414214	0.01834	-0.771462 0.000147 0.000174	0.99553	0.0004365	0.019173
12	a k n b	1.007039 0.001423 0.830290 -0.000009	0.99932	0.0001060	0.007977	0.993331 0.000330 0.986345 -0.000006	0.99587	0.0006156	0.019792	1.001472 0.000681 0.858524 -0.000005	0.99903	0.0001081	0.00900	1.01886 0.001323 0.76493 -0.00001	0.99833	0.0001740	0.011720



Table 3. Modelling of moisture ratio according to the drying time at 40, 50, 60, and 70 °C drying air temperatures and 1.5 m/s air velocity

Model no	Constants	V=1.5 m/s, T=70 °C				V=1.5 m/s, T=60 °C				V=1.5 m/s, T=50 °C				V=1.5 m/s, T=40 °C			
		Constants	R ²	χ ²	RMSE	Constants	R ²	χ ²	RMSE	Constants	R ²	χ ²	RMSE	Constants	R ²	χ ²	RMSE
1	k	0.00032	0.98654	0.0015488	0.037680	0.00024	0.99288	0.0007296	0.026028	0.00020	0.99357	0.0006125	0.02401	0.00014	0.99517	0.0004087	0.019854
2	k n	0.000384 0.97628	0.98381	0.0020483	0.041315	0.000333 0.966188	0.99057	0.0010466	0.029951	0.00026 0.974723	0.99308	0.0007033	0.02491	0.000468 0.866752	0.98330	0.0014674	0.036914
3	k n	0.00031 1.25280	0.99865	0.0001714	0.011952	0.00025 1.11608	0.99712	0.0003198	0.016558	0.00021 1.08236	0.99689	0.0003155	0.01668	0.00014 0.97522	0.99203	0.0007004	0.025503
4	a k	1.05414 0.00034	0.98901	0.0013907	0.034044	1.03912 0.00026	0.99430	0.0006328	0.023289	1.03077 0.00022	0.99474	0.0005346	0.02172	1.02955 0.00014	0.99493	0.0004450	0.020329
5	a k c	1.09832 0.00029 -0.06576	0.99684	0.0004440	0.018250	1.07147 0.00023 -0.05510	0.99891	0.0001325	0.010205	1.05714 0.00022 -0.003207	0.99391	0.000663	0.02336	1.06894 0.00015 -0.004938	0.99215	0.0007170	0.025303
6	a ko b k _i	1.826842 0.00046 -0.81942 0.000814	0.99781	0.0003463	0.015194	-0.093563 0.000366 1.133483 0.000266	0.99470	0.0007068	0.022469	0.511996 0.000219 0.511996 0.000221	0.99476	0.0006145	0.02167	0.511125 0.000139 0.511125 0.000139	0.99546	0.000431	0.019240
7	a k	0.002693 0.118472	0.98625	0.0017401	0.038080	0.002447 0.101508	0.99313	0.000763	0.025579	0.004844 0.043302	0.99448	0.000560	0.02224	0.005825 0.023317	0.99520	0.0004220	0.019795
8	a b	-0.00022689 0.00000001	0.99706	0.0003721	0.017611	-0.00018056 0.000000008	0.99106	0.0009932	0.029177	-0.0001512 0.00000001	0.98742	0.001278	0.03358	-0.00009559 0.000000002	0.98195	0.0015859	0.038374
9	a k b	-0.157991 0.019359 0.018969	0.99483	0.0007272	0.023354	-0.078678 0.012659 0.021209	0.99630	0.0004478	0.018758	-0.039406 0.015704 0.013950	0.99563	0.0004760	0.01979	-0.021106 0.012453 0.011208	0.99570	0.0003930	0.018732
10	a k b g c h	2.197149 0.000479 -0.787999 0.000912 -0.408693 0.000556	0.99721	0.0005878	0.017144	0.433591 0.000257 1.143389 0.000257 0.453699 0.000257	0.99451	0.0009148	0.022863	0.352955 0.000221 0.352955 0.000221 0.352955 0.000221	0.99307	0.0009598	0.02492	0.361445 0.000448 0.361445 0.000109 0.361445 0.000109	0.97929	0.0021508	0.041109
11	a k g	-2.85701 0.000713 0.000548	0.99620	0.0005340	0.020014	-2.79873 0.00045 0.00038	0.99480	0.0006295	0.022239	-1.60525 0.000115 0.000143	0.99895	0.00011471	0.00971	-1.09901 0.000064 0.000093	0.99453	0.0004996	0.021121
12	a k n b	0.997348 0.000057 1.203643 -0.000003	0.99960	0.0000628	0.006474	1.002727 0.000168 1.036276 -0.000004	0.99945	0.0000727	0.007208	0.997912 0.000202 0.993314 -0.000004	0.99947	0.00006199	0.00688	1.001703 0.000186 0.955617 -0.000002	0.99951	0.00004647	0.006311



Table 4. Modelling of moisture ratio according to the drying time at 40, 50, 60, and 70°C drying air temperatures and 0.8 m/s air velocity.

Model no	Constants	V=0.8 m/s, T=70 °C				V=0.8 m/s, T=60 °C				V=0.8 m/s, T=50 °C				V=0.8 m/s, T=40 °C			
		Constants	R ²	χ ²	RMSE	Constants	R ²	χ ²	RMSE	Constants	R ²	χ ²	RMSE	Constants	R ²	χ ²	RMSE
1	k	0.00029	0.98278	0.0019857	0.042813	0.00023	0.98446	0.0016982	0.039812	0.00017	0.97721	0.0024287	0.04789	0.00012	0.98998	0.000872	0.029009
2	k n	0.000299 0.99344	0.98193	0.0022736	0.043862	0.000365 0.943322	0.97677	0.0027334	0.048672	0.000326 0.93564	0.97210	0.0031586	0.05298	0.000227 0.91869	0.95136	0.0044011	0.063927
3	k n	0.00028 1.32422	0.99855	0.0001828	0.012437	0.00022 1.24845	0.99757	0.0002860	0.015743	0.00018 1.27243	0.99651	0.0003948	0.01873	0.00013 0.93744	0.98999	0.0009058	0.029002
4	a k	1.06646 0.00031	0.98615	0.0017423	0.038396	1.08252 0.00024	0.98829	0.0013780	0.034559	1.08153 0.00020	0.98617	0.0015653	0.03730	1.03025 0.00013	0.99638	0.0003275	0.017439
5	a k c	1.10837 0.00026 -0.05773	0.99496	0.0006975	0.023164	1.15574 0.00020 -0.08890	0.99640	0.0004590	0.019162	1.13930 0.000199 -0.037992	0.98870	0.0013644	0.03371	1.03225 0.00015 0.030236	0.99037	0.0009058	0.028439
6	a ko b ki	0.528448 0.000301 0.528448 0.000301	0.98561	0.0020750	0.037901	0.212004 0.000217 0.861260 0.000251	0.98844	0.0016081	0.034340	0.534480 0.000201 0.534480 0.000200	0.98649	0.0017486	0.03687	0.519899 0.000137 0.51989 0.000137	0.99624	0.0003682	0.017765
7	a k	0.000022 12.76146	0.98281	0.0021633	0.042784	0.002749 0.081617	0.98417	0.0018626	0.040178	0.002776 0.067483	0.98144	0.002101	0.04322	0.003375 0.038500	0.99507	0.0004459	0.020348
8	a b	-0.0002045 0.00000001	0.99811	0.0002376	0.014181	-0.0001634 0.00000001	0.99627	0.0004383	0.019491	-0.00013474 0.000000005	0.99722	0.0003142	0.01671	-0.00009299 0.000000002	0.98718	0.0011605	0.032826
9	a k b	-0.169596 0.021105 0.015716	0.99331	0.0009256	0.026684	-0.144924 0.060982 0.004216	0.99454	0.0006964	0.023604	-0.131699 0.024650 0.008604	0.99114	0.0010705	0.02986	-0.049925 0.012030 0.011376	0.99704	0.0002787	0.015777
10	a k b g c h	0.022357 0.000208 1.473202 0.000392 -0.504322 0.001000	0.99685	0.0006225	0.018308	0.553523 0.000240 0.255082 0.000243 0.255117 0.000245	0.98878	0.0019078	0.033833	0.354767 0.000200 0.354708 0.000200 0.354770 0.000200	0.98651	0.0020362	0.03684	0.343493 0.000134 0.341936 0.000134 0.345333 0.000134	0.99639	0.0003864	0.017425
11	a k g	-2.97038 0.000709 0.000530	0.99341	0.0009125	0.026494	-1.14587 0.000160 0.000184	0.98594	0.0017925	0.037868	-1.27293 0.000068 0.000107	0.99820	0.0002170	0.01344	-0.80896 0.000027 0.00006	0.97917	0.0019601	0.041834
12	a k n b	0.995118 0.000033 1.252341 -0.000002	0.99971	0.00003721	0.005597	1.007890 0.000059 1.148874 -0.000003	0.99926	0.0001029	0.008688	1.006970 0.000062 1.114616 -0.000004	0.99903	0.0001254	0.00987	1.007395 0.000112 1.009843 -0.000002	0.99962	0.00004524	0.005648

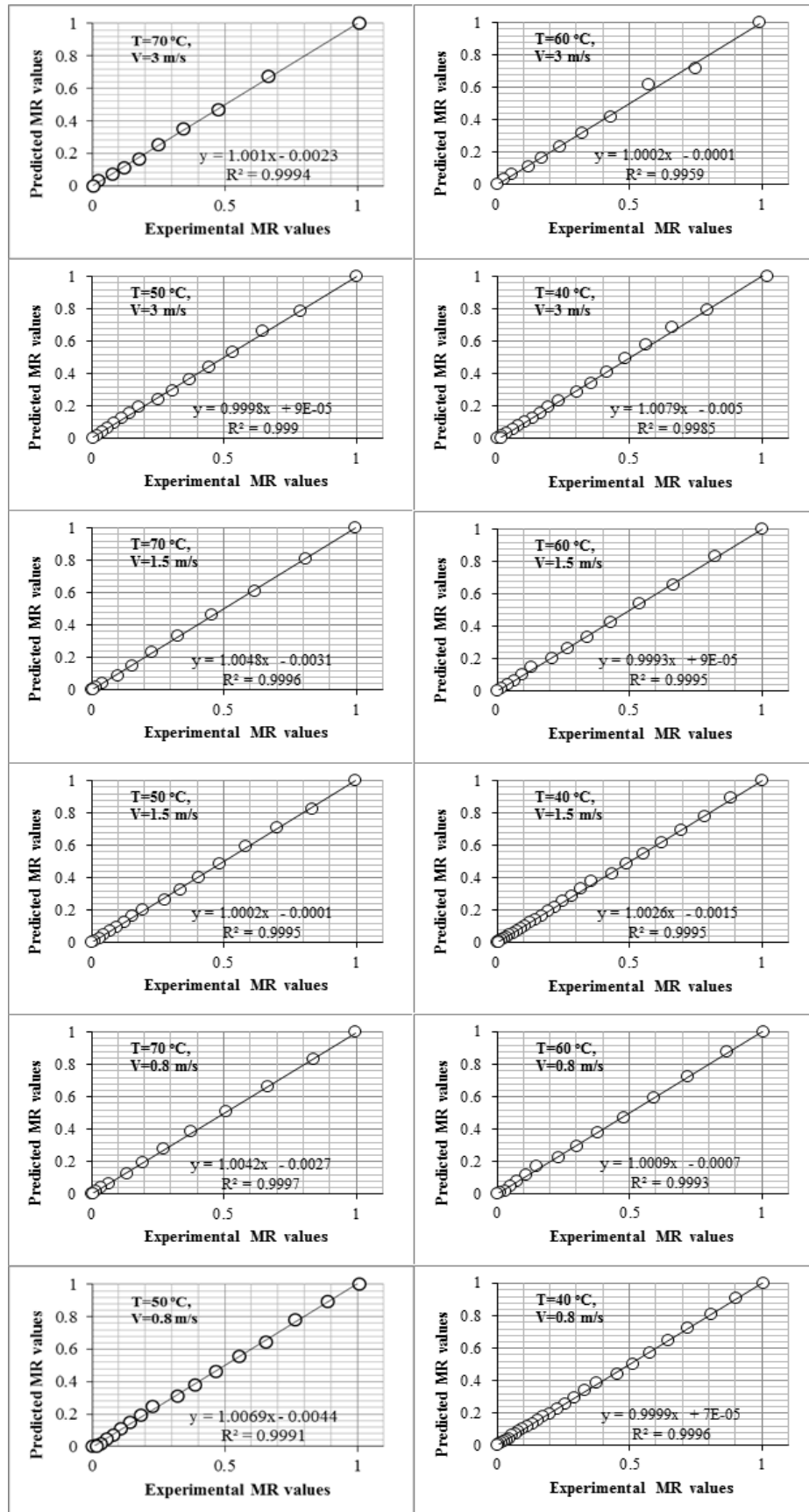


Figure 3. Comparison of experimental moisture ratios with those predicted from the Midilli *et al.* model for each one of the experimental conditions



4. Conclusions

The influence of drying air temperature and velocity on modeling of drying of ginger slices was investigated in this study. Drying of ginger slices occurred in falling rate period; no constant rate period of drying was observed for the present study, which implies that moisture removal from the material was governed by diffusion phenomenon. In order to explain the drying behaviour and to develop the mathematical modeling of ginger slices, 12 models were applied to thin layer forced drying processes. According to the statistical indicators, *Midilli et al. model* was found to be the most suitable for describing drying curve of the thin layer forced drying process of ginger slices. Among the twelve empirical models investigated in this study, the worst results were obtained with *Page, Wang and Singh, Modified Henderson and Pabis and Two term models* while the *Midilli et al. model* reasonably described the processes.

Nomenclature

a, b, c, g, h, n empirical constants in the drying models

k, k_o, k₁ empirical coefficients in the drying models (s⁻¹)

n number constants

N number of observations

M_e moisture content in equilibrium state (dry basis)

M_o moisture content at *t = 0* (dry basis)

M_t moisture content at *t* (dry basis)

MR moisture ratio (dimensionless)

MR_{exp} experimental moisture ratio (dimensionless)

MR_{pre} predicted moisture ratio (dimensionless)

R² regression coefficient

RMSE root mean square error

t time (s, hr, min)

V velocity (m/s)

T temperature (°C)

χ² chi-square

References

- [1] Nema, P. K., Mohapatra, D., Daniel, A., Mishra, S., Modeling Pulse Microwave Drying Kinetics of Ginger (*Zingiber officinale R.*), *Journal of Food Research and Technology*, 1(2) (2013), pp.46-58.
- [2] Yilbas, B.S., Hussain, M.M., Dincer, I., Heat and Moisture Diffusion in Slab Products to Convective Boundary Condition, *Heat Mass Transf.*, 39 (2003), pp.471–476.



- [3] Midilli, A., Kucuk, H., Yapar, Z., A New Model for Single Layer Drying, *Drying Technology*, 20(7) (2002), pp.1503-1513.
- [4] Panchariya, P.C., Popovic. D., Sharma, A.L., Thin-layer Modelling of Black Tea Drying Process, *J Food Eng.* 52 (2002), pp.349–357. doi: 10.1016/S0260-8774(01)00126-1.
- [5] Demirtas, C., Ayhan, T., Kaygusuz, K., Drying Behavior of Hazelnuts, *J Sci Food Agric.*, 76 (1998), pp.559–564. doi: 10.1002/(SICI)1097-0010(199804)
- [6] Ece, M.C., Cihan, A., A Liquid Diffusion Model for Drying Rough Rice, *Trans Am Soc Agric Eng.*, 36 (1993), pp.837–840.
- [7] Ozdemir, M., Devres, Y.O., The Thin Layer Drying Characteristics of Hazelnuts During Roasting, *J Food Eng.*, 42 (1999), pp.225–233. doi: 10.1016/S0260-8774(99)00126-0.
- [8] Wang, C.Y., Singh, R.P., A Single Layer Drying Equation for Rough Rice, *ASAE Paper no: 3001* (1978).
- [9] Kumar, N., Sarkar, B.C., Sharma, H.K., Mathematical Modelling of Thin Layer Hot Air Drying of Carrot Pomace, *J Food Sci Technol.*, 49(1) (2012), pp.33–41.
- [10] Silva, W.P., Silva, C.M.D.P.S., Gama, F.J.A., Gomes, J.P., Mathematical Models to Describe Thin-Layer Drying and to Determine Drying Rate of Whole Bananas, *Journal of the Saudi Society of Agricultural Sciences*, 13 (2014), pp.67–74.
- [11] Parlak, N., Fluidized Bed Drying Characteristics and Modeling of Ginger (*zingiber officinale*) slices, *Heat Mass Transfer*, 51 (2015), pp.1085–1095.
- [12] Schweiggert, U., Hofmann, S., Reichel, M., Schieber, A., Carle, R., Enzyme-assisted Liquefaction of Ginger Rhizomes (*Zingiber officinale* Rosc.) for the Production of Spray-Dried and Paste-Like Ginger Condiments, *Journal of Food Engineering*, 84 (2008), pp.28–38.
- [13] Singhanat, P., Saentaweasuk, S., Effect of Two Stage, Tray And Heat Pump Assisted-Dehumidified Drying on Drying Characteristics and Qualities of Dried Ginger, *Food and Bioproducts Processing*, 89 (2011), pp.429–437.
- [14] Eze, J.I., Agbo, K., Comparative Studies of Sun and Solar Drying of Peeled and Unpeeled Ginger, *Am. J. Sci. Ind. Res.*, 2(2) (2011), pp.136-143.
- [15] Prasad, J., Vijay, V.K., Experimental Studies on Drying of *Zingiber Officinale*, *Curcuma longa* L. and *Tinospora Cordifolia* in Solar-Biomass Hybrid Drier, *Renewable Energy*, 30 (2005), pp.2097–2109.
- [16] Thorat, I.D., Mohapatra, D., Sutar, R.F., Kapdi, S.S., Jagtap, D.D., Mathematical Modeling and Experimental Study on Thin-Layer Vacuum Drying of Ginger (*Zingiber Officinale* R.) Slices, *Food Bioprocess Technol*, DOI 10.1007/s11947-010-0429-y, 2010.
- [17] Akpınar, E.K., Toraman, S., Estimation of The Moisture Diffusivity and Activation Energy in Thin Layer Drying of Ginger Slices, *World Academy of Science, Engineering and Technology*, 78 (2013) 2013-06-27.



- [18] Akpınar, E.K., Toraman, S., Determination of Drying Kinetics and Convective Heat Transfer Coefficients of Ginger Slices, *Heat Mass Transfer*, 2015, DOI 10.1007/s00231-015-1729-6.
- [19] Akpınar, E.K. The Development of a Cyclone Type Dryer for Agricultural Products, PhD Thesis, Firat University, Elazığ, Turkey, 2002.
- [20] Akpınar, E., Midilli, A., Bicer, Y., Single Layer Drying Behavior of Potato Slices in a Convective Cyclone Dryer and Mathematical Modeling, *Energy Conversion and Management*, 44 (2003), pp.1689-1705.
- [21] Doymaz, I., Evaluation of Some Thin-Layer Drying Models of Persimmon Slices (*Diospyros kaki* L.), *Energy Conversion and Management*, 56 (2012), pp.199-205.
- [22] Mujumdar, A.S., Handbook of Industrial Drying, Marcel Dekker, New York, 1987.
- [23] Diamante, L.M., Munro, P.A., Mathematical Modelling of Thin Layer Solar Drying of Sweet Potato Slices, *Solar Energy*, 51 (1993), pp.271-276.
- [24] Overhults, D.G., White, H.E., Hamilton, H.E., Ross, I.J., Drying Soybeans with Heated Air, *Transactions of the ASAE*, 16 (1973), pp.112-113.
- [25] Zhang, Q., Litchfield, J.B., An Optimization of Intermittent Corn Drying in A Laboratory Scale Thin Layer Dryer, *Drying Technology*, 9 (1991), pp.383-395.
- [26] Yıldız, O., Ertekin, C., Thin Layer Solar Drying of Some Vegetables, *Drying Technology*, 19 (2001), pp.583-596.
- [27] Henderson, S.M., Progress in Developing The Thin Layer Drying Equation, *Transactions of the ASAE*, 17 (1974), pp.1167-1172.
- [28] Sharaf-Eldeen, Y.I., Blaisdell, J.L., Hamdy, M.Y., A Model For Ear Corn Drying, *Transaction of the ASAE*, 23 (1980), pp.1261-1271.
- [29] Karathanos, V.T., Determination of Water Content of Dried Fruits by Drying Kinetics, *Journal of Food Engineering*, 39 (1999), pp.337-344.
- [30] Verma, L.R., Bucklin, R.A., Endan, J.B., Wratten, F.T., Effects of Drying Air Parameters on Rice Drying Models, *Transaction of the ASAE*, 28 (1985), pp.296-301.
- [31] Akpınar, E.K., Determination of Suitable Thin Layer Drying Curve Model For Some Vegetables And Fruits, *Journal of Food Engineering*, 73(1) (2006), pp.75-84.
- [32] Gunhan, T., Demir, V., Hancıoğlu, E., Hepbaşlı, A., Mathematical Modelling of Drying of Bay Leaves, *Energy Conversion and Management*, 46(11-12) (2005), pp.1667-1679.



MECHANICAL PROPERTIES OF THE COMPOSITE MATERIAL PRODUCED BY THE MIXTURE OF EXPANDED PERLITE, WASTE MARBLE DUST AND TRAGACANTH

Şermin KOÇYİĞİT^{1}, Vedat Veli ÇAY²,*

¹ Technical Sciences Vocational School, Dicle University, Diyarbakır, Turkey

² Civil Aviation High School, Dicle University, Diyarbakır, Turkey

Corresponding author; sermin.kocyigit@dicle.edu.tr

Received: 10 November 2018; Accepted: 29 December 2018

In this study, the strength characteristics of the expanded perlite aggregate, waste marble dust and tragacanth added cement based composite material were investigated. A composite construction material was prepared using expanded perlite aggregate with a particle size of 0-2 mm and 2-4 mm at the ratio of 10%, 30% and 50% by weight, waste marble powder produced by sieving through 0.25 mm sieve at the ratio of 10% and 20%, tragacanth at the ratio of 0%, 0.5% and 1% and CEMI 42.5 N type Portland cement. Density, compressive strength, abrasion loss, water absorption tests were performed on these prepared composite samples. It was seen that compressive strength and density values have decreased and abrasion loss and water absorption values have increased as expanded perlite particle size, expanded perlite ratio, tragacanth ratio have increased and waste marble powder ratio has decreased on the prepared samples.

Key words: expanded perlite, waste marble dust, tragacanth, mechanical properties

1. Introduction

It is clear that increasing population density, resource consumption and environmental pollution across the world negatively affect the ecology of our planet. The construction sector is responsible for 50% of the material resources in nature, 40% of energy consumption and 50% of total waste. This will further increase due to the increasing number of buildings in parallel with the increase in world population and will cause irrecoverable damage to the ecosystem [1]. Low-density, in other words, lightweight concretes should be used for earthquake resistant buildings. [2]. The density of lightweight concretes produced by adding low density aggregates to it is between 0.8 g/cm³ and 2 g/cm³. The use and investigation of lightweight concretes are increasing with each passing day due their low density,

low thermal conductivity coefficient value and architectural flexibility characteristics. Lightweight concretes with superior properties such as heat and sound insulation have significant advantages over normal concretes due to energy saving and comfort they provide. These studies have mainly focused on the addition of different aggregates into the cement [3]. One of the materials used as an aggregate in the production of lightweight concrete is the expanded perlite. The thermal conductivity coefficient of expanded perlite is given as 0.40-0.45 W/mK. It is important to keep the internal temperatures of indoor spaces at the desired level, to save energy in heating cooling operations against external climatic conditions, to solve environmental problems, to reduce air pollution, and most importantly, to take heat insulation measures in the structures with expanded perlite. [4]. Due to its high heat and sound insulation and economy, the market share of expanded perlite in our country's construction sector has increased by 4 times in the last 10 years [5-7]. For mortar or concrete production, great numbers of worldwide studies have been carried out on natural (such as diatomite, pumice, slag, sawdust, palm oil shells and lower ash) or artificial (such as expanded clay, gravel, slate, perlite and vermiculite) aggregates. [8–14]. Tragacanth has an adhesion property and is used as a binding material when it is mixed with cement and waste marble powder. The utilization of marble wastes, which have technological and economic value, along with expanded perlite is an important raw material in the production of composite constructional components in terms of the compliance of our country with the environment and recycling strategies. An increase is observed in the number of marble processing plants in our country in order to meet the increasing demand for marble. As a natural consequence of this, it is seen that the marble waste sites, which form a negative reaction in the public eye due to environmentalism and since it destroys natural beauty, has become widespread in the regions where the marble processing plants have become intense [15-17]. Powder wastes that arise from marble factories as production wastes cannot be evaluated in general, and their storage or disposal into the natural environment may lead to environmental pollution and the problems such as the pollution of natural resources. Waste marble powders, which can be used in various industrial branches, can be a much cheaper input when they are used instead of their alternatives. Powder wastes reduced to different size fractions are used in many areas apart from their use as a construction material in the literature studies on the utilization of materials thrown to waste sites in marble processing plants [18]. Soykan and Özel [19] investigated the use of marble waste as an aggregate in polymer concrete technology. Gündüz et al. [20] mixed various waste marble powders with doped Portland cement at various dosages and investigated the techno-mechanical properties of the obtained samples at different curing times. Türker et al. [21] examined the effects of waste marble powders on hydration and microstructure of cement. In their experimental study, Şengül et al. [22] replaced expanded perlite with natural aggregate in lightweight concrete mixtures and investigated its effect on heat insulation property. Since the tragacanth used in the experiments was a natural and local resin, its effects in the samples desired to be produced at different ratios and the thermal and mechanical behavior with different proportions of expanded perlite aggregate were examined, and its effect on the strength of the samples was investigated with waste marble powder substitution.

2. Material and method

For the preparation of samples, raw perlite was obtained from perlite deposits in Izmir Bergama region, and it was made usable by crushing in the business and expanding at 800°C in the factory furnaces and sieving at the desired ratios. The samples were divided into two groups in 0-2 and 2-4, mm grain size, as it is seen Figure 1. As a waste marble powder additive, the aqueous wastes obtained during

the production of marble types produced by Diyarbakır Beden Mermer ve Maden İşletmesi San. ve Tic. A.Ş. were used by drying and grinding them. CEM I 42.5 N Portland cement produced in Diyarbakır Ölmezler Concrete Plant was used as the cement. Diyarbakır's city water supply was used as the mixing water in accordance with the standards specified in TS EN 1008. In the study, the leaf tragacanth was powdered with an electric motor grinder for a better and faster melting. In the preliminary studies carried out, it was determined that 100 g tragacanth was fully soluble in approximately 5 liters of water. 100 g powdered tragacanth, which was weighed with precision scales, was placed in a 5 liter water container and 2 liters of water was added to the beaker and mixed thoroughly. The mixing process was maintained at certain intervals for 1 day. After the tragacanth was thoroughly cracked and swelled, 1 liter of water was added to the mixture at intervals of 1-2 hours with beaker and it was continued to mix it. After the completion of 5 liters of water, the tragacanth mix was filtered 2 times and transferred to another container [23]. The samples produced were evaluated as a new building material and their usage areas were determined according to the test results. The expanded perlite aggregates which were divided into three groups of with a particle size of 0-2 mm, 2-4 mm at the ratio of 10%, 30% and 50% by weight, waste marble powders produced by sieving through 0.25 mm sieve at the ratio of 10% and 20%, and 0%, 0.5% and 1% tragacanth and cements were added into the mixtures for the preparation of samples



Figure 1. Expanded Perlite Aggregates Sized as 0-2 and 2-4 mm



Figure 2. Samples Cast into Plywood Molds

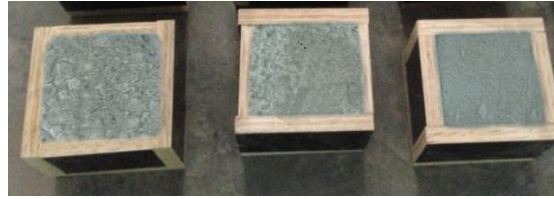


Figure 3. Samples Prepared for Compressive Strength, Abrasion Loss, High Temperature and Freezing-Thawing Compressive Strength Tests

The waste marble powder sieved through 0.25 mm sieve that was used in the experiments is presented in Figure 4. The leaf form of tragacanth used in the experiments and its appearance after it was melt in water and filtered is seen in Figure 5



Figure 4. Waste Marble Powder Sieved Through 0.25 mm Sieve



Figure 5. Leaf Form of Tragacanth (a) Its Appearance After it (b) was Filtered

2.1. Mechanical Tests

The compressive strength and abrasion loss tests were applied to the samples obtained from cube shaped plywood molds with dimensions of 100x100x100 mm. Ele International brand device, used for compressive strength tests applied to samples, is equipped with a capacity of 3000 kN, with a digital control panel, with adjustable loading speed and a single-axis force. In the determination of the abrasion loss by friction in the samples, the measurement of weight reduction was preferred and it was done with the Böhme instrument. Abrasion loss (AL) values were calculated using formula (1).[23-25]

$$\% AL = \frac{Firstmass - Lastmass}{Firstmass} \times 100 \quad (1)$$

While water absorption test was performed, 20x60x150 mm test samples were first placed in drying oven set at (105±5)°C temperature and dried until constant weight was achieved. The powders on the samples, which were provided to be in constant weight in this way, were cleaned with a brush and then weighed at a precision of 0.1 g, and then dry sample weights (W_d) were determined. Thus, the dried samples were placed in a container with water at a depth of $\frac{1}{4}$ of the sample height and at room temperature. Water was added to the container so that samples would be in water by half an hour later and $\frac{3}{4}$ water at the end of the second hour. Water was added 24 hours after the beginning of the experiments so that the samples were completely in water.[26-28]. In this case, the samples, which were removed from the water after 24 hours, were wiped with a piece of wetted cloth, weighed at a precision of 0.1 g, and water-soaked weights were found (W_w). By taking the ratio of these two weights, the percentage of water absorption was calculated by formula (2) in % with the following expression.

$$WA \% = \frac{W_w - W_d}{W_d} \times 100 \quad (2)$$

The density measurement of 20x60x150 mm samples was made with Isomet 2104 heat transfer analyzer of Applied Precision Company. The device has been developed especially for the determination of the thermophysical properties of constructional components, natural stone and soil. The device works according to the hot wire method.

3. Result and discussion

Density is one of the important parameters that can control the amount of construction materials and many physical properties in the production of lightweight concrete. It was determined that density values decreased from 1.889 to 0.939 depending on the ratio of expanded perlite aggregates in the samples produced, the expanded perlite particle size and tragacanth ratio, and the waste marble powder ratio. The results of density, porosity, compressive strength, abrasion loss, and water absorption rate measurements are presented in Table 1. The pressure values decreased in the samples in which the expanded perlite particle size, the expanded perlite ratio and tragacanth ratio were same but the waste marble powder ratio increased. This is due to the fact that the waste marble powder filled the porosities in the sample and that the amount of cement decreased. The excess of these porosities makes it possible to produce samples with lower density. However, this causes the gases in porosities to be replaced by water or water vapor in humid environments. The increase in expanded perlite particle size, expanded perlite ratio and tragacanth ratio and the decrease in waste marble powder ratio increased the amount of porosity.

Lower porous samples will be produced depending on the decrease in expanded perlite particle size and expanded perlite ratio as the waste marble powder and cement ratio used in the sample increase. The compressive strengths, abrasion loss ratios and water absorption rates of the samples with expanded perlite with 0-2 and 2-4 mm particle sizes, waste marble powder and tragacanth-cement binder are presented in Table 1. When Table 1 is examined, it is seen that the compressive strength of the samples with 0-2 mm particle size varies between 17.36 - 31.67 MPa and that the compressive strength of the samples with 2-4 mm particle size varies between 15.97 - 29.60 MPa.

The sample encodings in Table 1 are as the following.

Number One expanded perlite diameter

X: (0–2) mm.

Y: (2–4) mm.

Z: Cement

Number three waste marble % mixture ratio

1: 10%

2: 20%

Number two expanded perlite % mixture ratio

1: 10% expanded perlite (\cong 80% cement ratio)

3: 30% expanded perlite (\cong 60% cement ratio)

5: 50% expanded perlite (\cong 40% cement ratio)

Number four tragacanth % mixture ratio

0: 0.0%

1: 0.5%

2: 1%

Table 1. Mechanical Test Results Of The Composite Samples Produced

Sample code	Density (g/cm ³)	Porosity (%)	Compressive strength (MPa)	Abrasion loss (%)	Water absorption (%)
Samples with 0 % tragacanth ratio					
X110	1.789	0.305	31.67	0.65	19.57
X310	1.567	0.321	27.82	0.82	19.85
X510	1.517	0.352	25.05	1.01	21.26
X120	1.889	0.251	28.94	0.75	18.63
X320	1.678	0.271	26.01	0.92	19.76
X520	1.583	0.293	24.41	1.11	20.17
Y110	1.611	0.414	29.60	0.74	20.48
Y310	1.489	0.442	25.92	0.94	21.25
Y510	1.439	0.465	24.10	1.15	22.26
Y120	1.661	0.339	27.90	0.81	20.19
Y320	1.567	0.392	25.18	0.96	20.98
Y520	1.517	0.408	23.02	1.24	21.43
Samples with 0.5 % tragacanth ratio					
X111	1.639	0.311	26.75	0.87	24.17
X311	1.539	0.329	22.90	1.04	24.45
X511	1.394	0.368	20.13	1.23	25.86
X121	1.694	0.259	24.02	0.97	23.23
X321	1.556	0.283	21.09	1.14	24.36
X521	1.456	0.299	19.49	1.33	24.77
Y111	1.444	0.421	24.68	0.96	25.08
Y311	1.406	0.450	21.00	1.16	25.85
Y511	1.283	0.477	19.18	1.37	26.86
Y121	1.550	0.348	22.98	1.03	24.79
Y321	1.478	0.404	20.26	1.18	25.58
Y521	1.378	0.415	18.10	1.46	26.03
Samples with 1 % tragacanth ratio					
X112	1.500	0.317	23.62	1.05	29.84
X312	1.400	0.338	20.77	1.22	30.12
X512	1.256	0.379	18.00	1.41	31.53
X122	1.556	0.263	21.89	1.15	28.90
X322	1.417	0.294	18.96	1.32	30.03
X522	1.317	0.303	17.36	1.51	30.44
Y112	1.306	0.429	22.55	1.14	30.75
Y312	1.267	0.461	18.87	1.34	31.52
Y512	1.144	0.488	17.05	1.55	32.53
Y122	1.411	0.353	20.85	1.21	30.46
Y322	1.339	0.417	18.13	1.36	31.25
Y522	1.239	0.423	15.97	1.64	31.70

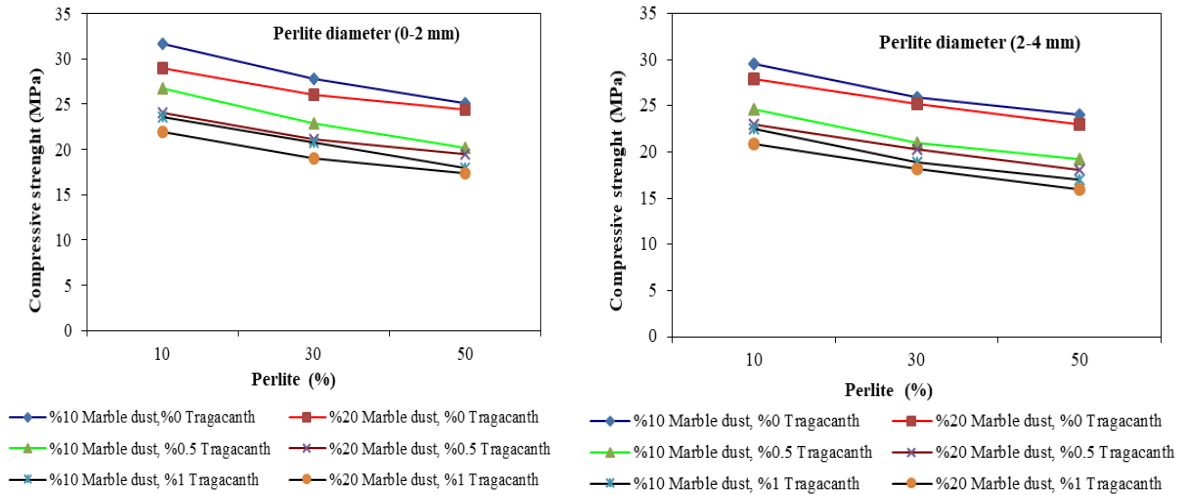


Figure 6. Change in compressive strength depending on the expanded perlite, waste marble powder and tragacanth ratios

When Figure 6 was examined, it was seen that the expanded perlite in the samples could not provide an adequate adhesion with the waste marble powder and decreased the compressive strength by increasing the waste marble powder ratio in the sample for all three types. Furthermore, compressive strength decreased depending on the increase in tragacanth ratio in the sample. This shows that the waste marble powder with low particle size increased the pore ratio in the sample and decreased the strength values and that the compressive strength of the samples decreased along with the increase in expanded perlite particle size.

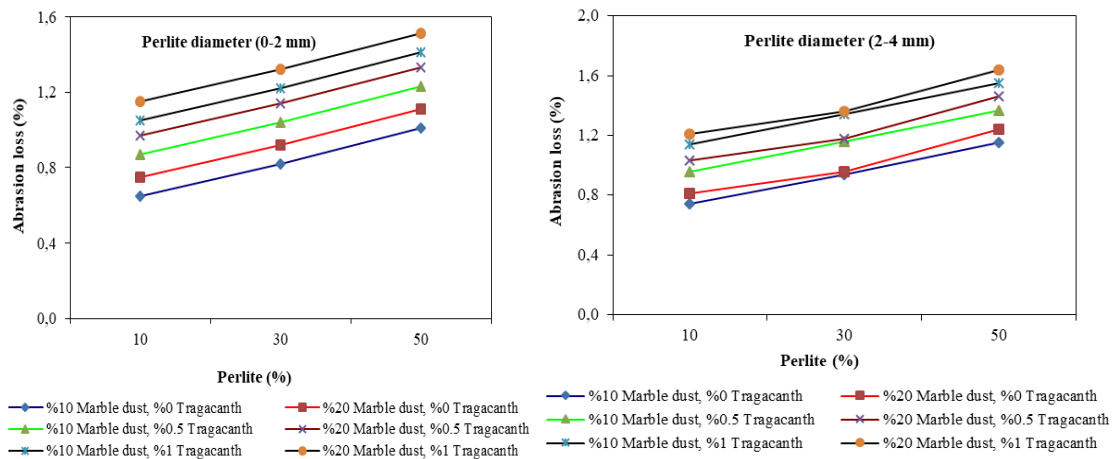


Figure 7. Abrasion Loss Change depending on the expanded perlite, waste marble powder and tragacanth ratios

The results in Table 1 show that the samples with a large expanded perlite particle size and high waste marble powder ratio and tragacanth ratio are not resistant to abrasion. It is seen that the abrasion resistance decreased along with the increase in waste marble powder ratio. The abrasion loss with friction was compared in Figure 7, and the effect of expanded perlite, waste marble powder and tragacanth on abrasion loss with friction was investigated. It was determined that the samples with an expanded perlite particle size of 0-2 and 2-4 mm and the sample with tragacanth ratio of 1%, expanded perlite ratio of 50% and waste marble powder ratio of 20% had no resistance to abrasion. The abrasion

loss ratio of the samples produced with expanded perlite aggregates with a 0-2 mm particle size varied between 0.65 and 1.51. The abrasion loss of the samples produced with expanded perlite aggregates with a 2-4 mm particle size varied between 0.74 and 1.64. The abrasion loss of the samples produced with expanded perlite aggregates with a -8 mm particle size varied between 0.88 and 1.95. The water absorption ratios of some of the produced samples were determined to be above 30% of the critical value. The samples produced have a porous structure, and the porosity ratio varies within the whole structure depending on the expanded perlite particle size, expanded perlite ratio, and waste marble powder ratio. This increases the water absorption capacity and the water absorption values of the samples by allowing water to be retained in these pores when the samples come into contact with water. When the samples' water absorption ratios according to the changes in expanded perlite particle size, expanded perlite ratio, waste marble powder ratio, and tragacanth ratio in Figure 8 are examined, the water absorption ratio increases as the expanded perlite particle size, expanded perlite ratio and tragacanth ratio increase, and the water absorption ratio increases as the waste marble powder ratio increases since the waste marble powder will fill the pores in the sample.

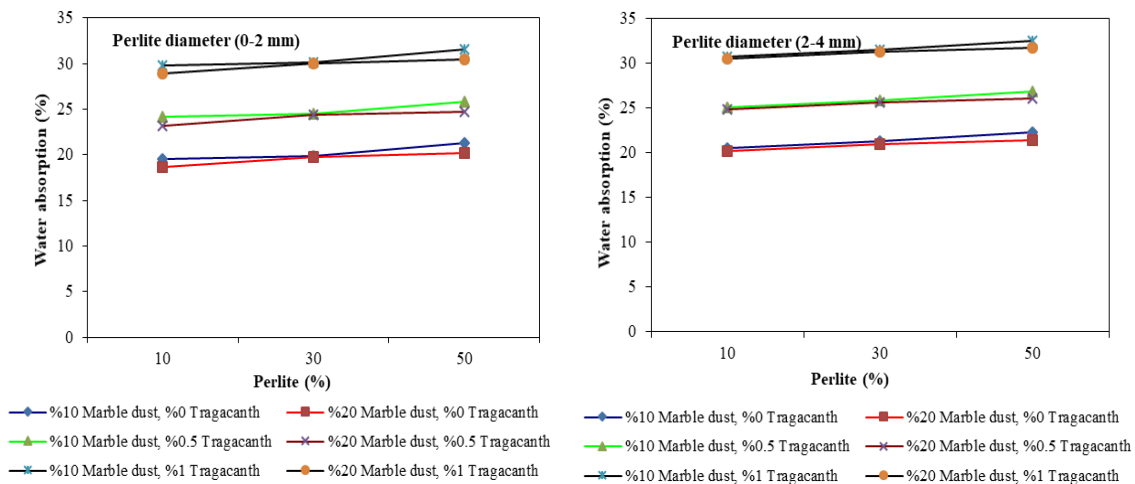


Figure 8. Change in Water Absorption Ratio depending on the expanded perlite, waste marble powder and tragacanth ratios

As it is seen in water absorption graphics, the water absorption ratios of the samples with a particle size of 0-2 mm vary between 18.63% - 22.64% and the water absorption ratios of the samples with a particle size of 2-4 mm vary between 23.23% - 27.24%.

4. Conclusions

In this study, density, water absorption, compressive strength and abrasion loss were performed respectively on the composite samples prepared, and the following conclusions were obtained.

- ✓ The amount of porosity in the sample changed depending on the waste marble powder ratio. The waste marble powder filled the pores caused by the expanded perlite and tragacanth in the samples and increased the abrasion loss since it could not provide adhesion, and it reduced the compressive strengths. The abrasion loss can be significantly improved by the addition of cement. The water absorption ratio increased by the reduction of waste marble powder. Because water easily reached these pores through capillary channels since the pores could not be filled by decreasing the waste marble powder ratio.

- ✓ As the expanded perlite particle size, expanded perlite ratio, tragacanth ratio and waste marble powder ratio in the composite samples prepared decreased, the compressive strength and the abrasion loss and water absorption values increased.

In conclusion, expanded perlite, waste marble powder and tragacanth can be used as alternative raw material sources for the production of porous construction materials. It should be considered that these type of lightweight concretes produced are weaker under load compared to normal concretes. They cannot be used in the places that are directly exposed to water. To coat the surfaces of the samples produced with waterproofing materials may inhibit the capillary absorption of water, and it should not be forgotten that such measures lead to additional costs.

Referances

- [1] <http://ec.europa.eu/enterprise/construction/suscon/tgs/tgl/efcmfin.htm>
- [2] Neville, A.M., 1975. "Properties of concrete", Pitman publishing, London, 606-607
- [3] Ortak Geleceğimiz, 1987. London: Oxford Üniv. Yayınları, WCED Raporu, <http://www.worldsummit2002.org/guide/brundtland.htm>.
- [4] Doğan, H., Şener, F., 2004. Hafif Yapı Malzemeleri (Pomza - Perlit - Ytong - Gazbeton) Kullanımının Yaygınlaştırılmasına Yönelik Sonuç ve Öneriler, Haber Bülteni, 1, 51-53.
- [5] Çiçek, Y. E., 2002. Pişmiş toprak tuğla, bimsbeton, gazbeton ve perlitli yapı malzemelerinin fiziksel, kimyasal ve mekanik özelliklerinin karşılaştırmalı olarak incelenmesi, Yüksek Lisans Tezi, İTÜ Fen Bilimleri Enstitüsü, İstanbul.
- [6] TS 3681, 1982. Genleştirilmiş perlit agregası, Türk Standartları Enstitüsü, Ankara.
- [7] Azizi, S., 2015, Perlit Katkılı Hafif Betonların Mekanik Özellikleri ve Isı Yalıtımı. (Yüksek Lisans Tezi). İstanbul Teknik Üniversitesi, Fen Bilimleri Enstitüsü. İstanbul.
- [8] Bouguerra A, Ledhem A, De Barquin F, et al. Effect of microstructure on the mechanical and thermal properties of lightweight concrete prepared from clay, cement, and wood aggregates. *Cem. Concr. Res.* 1998;28:1179–1190.
- [9] Hossain KMA. Blended cement using volcanic ash and pumice. *Cem. Concr. Res.* 2003;33:1601–1605.
- [10] Hossain KMA, Lachemi M. Development of volcanic ash concrete: strength, durability and micro-structural investigations. *ACI Mater. J.* 2006;103:11–17
- [11] Hossain KMA, Ahmed S, Lachemi M. Lightweight concrete incorporating pumice based blended cement and aggregate: Mechanical and durability characteristics. *Constr. Build. Mater.* 2011;25:1186–1195.
- [12] Gavligi HA, Tragacanth gum: structural composition, natural functionality and enzymatic conversion as source of potential prebiotic activity [PhD thesis]. Technical University of Denmark, Department of Chemical and Biochemical Engineering; 2012.
- [13] Hemmings RT, Cornelius BJ, Yuran P, et al. Comparative study of lightweight aggregates. In: *Proceedings of the World of Coal Ash (WOCA); 2009 May 4–7; Lexington (KY): Ash Library; 2009.*
- [14] Bicer Y, Yılmaz S. Producing new composite materials by using tragacanth and waste ash. *World Acad. Sci. Eng. Technol.* 2013;7:5–24.
- [15] Töre I. Uses of pumice as alternative flux for floor tile products. *Int. J. Sci. Mod. Eng. (IJISME)*2013;1: 16–19. ISSN: 2319-6386.
- [16] Serin, G., 1999. "Pomza'nın hafif beton blok duvar elemanı olarak kullanılmasının araştırılması", Yüksek Lisans Tezi, Süleyman Demirel Üniversitesi Fen Bilimleri Enstitüsü, Isparta, 100.
- [17] Ağırır, L.M., 1989. "Altınapa bims agregasından TS 3234'e uygun hafif beton briket imali", Yüksek Lisans Tezi., Selçuk Üniversitesi Fen Bilimleri Enstitüsü, Konya, 69.
- [18] Dincer, İ., (2002), "Thermal energy storage and phase-change materials", Course on Porous Media, Evora, Portugal.



- [19] Soykan, O. ve Özel, C., 2012. Mermer Tozu Tane Boyutunun Polimer Beton Özelliklerine Etkisi, International Construction Congress-ICOCNC2012, October 11-13, Isparta/Turkey.
- [20] Gündüz, L., Sarıışık, A., Davraz, M.U. ve Çankıran, O., 1998. Pomza Teknolojisi, Cilt 3, SDÜ-ISBAS, 14-31, Isparta.
- [21] Türker, P., Erdoğan, B., Katnaş, F. ve Yağınobalı, A., 2003. Türkiye’deki uçucu küllerin sınıflandırılması ve özellikleri, Türkiye Çimento Müstahsilleri Birliği Yayınları, Ankara, 76 s.
- [22] Sengül O., Azizi S., Karaosmanoglu F., Tasdemir M. A., 2011. Effect of expanded perlite on the mechanical properties and thermal conductivity of lightweight concrete, Energy and Buildings. 43: 671–676.
- [23] Demirboğa, R. ve Gül R., 2003. Thermal conductivity and compressive strength of expanded perlite aggregate concrete with mineral admixtures. Energy and Buildings. 35: 1155-1159.
- [24] Öztürk M., 2012. Pomza ve Perlit İçerikli Hafif Betonların Fiziksel ve Mekanik Özelliklerin İncelenmesi. (Yüksek Lisans Tezi). Namık Kemal Üniversitesi, Fen Bilimleri Enstitüsü, Tekirdağ.
- [25] Demirboğa, R. ve Gül, R., 2003. “The effects of expanded perlite aggregate, silica fume and fly ash on the thermal conductivity of lightweight concrete”, Cement and Concrete Research, 33, (5): 723-727.
- [26] Kocıyigit F. Kitre Katkılı Bims ve Çimento Karışımlarının Yeni Bir Yapı Malzemesi Olarak Değerlendirilmesi [Evaluation of pumice and cement mixture with tragacanth as a new building materials] [PhD thesis]. Firat University; 2012. Turkish.
- [27] Beden Mermer ve Maden İşletmeleri San. ve Tic. A.Ş.
- [28] Mehta, P.K., 1986. Concrete, structure properties and materials, Printice Hall, USA 152-158.



INVESTIGATION OF EXTERNAL BONDED PATCH REPAIR OF LAMINATED COMPOSITE MATERIALS EXPERIMENTALY

Şükrü ÇETİNKAYA¹, Haşim PIHTILI², Hayri YILDIRIM^{3*}

¹Mechanical Engineering Department / Dicle University, Turkey

²Mechanical Engineering Department / Fırat University, Turkey

³Diyarbakır Technical Science Vocational School / Dicle University

* Corresponding author; E-mail: hyildirim@dicle.edu.tr

Received: 17 October 2018; Accepted: 18 December 2018

For this study, woven glass and carbon fibres reinforced composite materials were produced. Composite materials have been produced with eight laminates. For experimental study, specimens with 10 mm internal hole were prepared. Then, these specimens were repaired by using adhesive and composite patches with different repair parameters. Two different bonding patch type were used for external bonding patch repair of the specimens. These were wet lay out patches and prepreg patches. Test specimens were prepared in necessary curing temperatures and laboratory conditions. By performing the unidirectional tensile test to these specimens, the ultimate failure loads of these repaired specimens were indicated. By comparing these ultimate failure loads of repaired specimens that prepared with various parameters, the effects of several repair parameters on the ultimate failure strength are investigated. These repair parameters are patch bonding area (D/W ratio), bonding length, adhesive thickness and patch thickness.

Key words: Laminate Composite Materials, bonded repair, patch, adhesive, failure strength

1. Introduction

With technological improvements, applications of composite materials have been increased both commercial and military aircraft structures applications in recent years. For such applications, composite materials have excellent properties. Due to high cost of these materials, maintenance of them, have been

important. In industry, spare parts repair of these composite materials, have been preferred than replacement of spare parts. Sometimes, replacements of the damaged spare parts are costly and unnecessary. Nowadays, more structures that prepared by composite materials with a few defects or local damages can be repaired successfully.

In industry, various repair techniques have been successfully applied. Among them, adhesively bonded structural repair has gained more favour than mechanically fastened structural repair for the reason that fiber reinforced composites are essentially bonded in nature. Therefore, in recent years, considerable experimental and numerical studies have been conducted to investigate the influence of different repair parameters on the stress distributions, ultimate strength and stress intensity factor of the bonded repaired structures [1]. A number of authors [1-9,11,16] have studied the analysis of failure mechanism of the bonded patch repair in laminated composite materials. Wisnom M.R. [10] has reviewed the size effects in the testing of fibre-composite materials. Predictive fracture model for composite bonded joints has been proposed by Goyal V.K. and et al. [12]. Principles and practices of adhesive bonded structural joints and repairs have studied by Davis M. [13]. Little research has been carried out to analyse the ultimate failure load of repaired structures with various repair parameters.

In aircraft applications, less weight is the important criteria for the maintenance of the parts. For such repair applications in laminated composite materials, external bonded patch repair technique has been more preferable than using mechanical fastened repair. Because, using mechanical fasteners increase the weight and the stress concentration factor of the repaired structures. Also, in external patch bonding repair, the optimum quantity of repair materials must be used in order to protect weight increment of the repaired structure. These main repair materials are adhesives and composite patches. The adhesives and patches should have been used in minimum quantity in repairs without decrease the load carrying capacity of the structures. Also, in adhesively bonded repairs, the stresses that occur in bonded joints are more uniform than that of pinned joints. These stress representations for various connections are illustrated in Fig. 1.

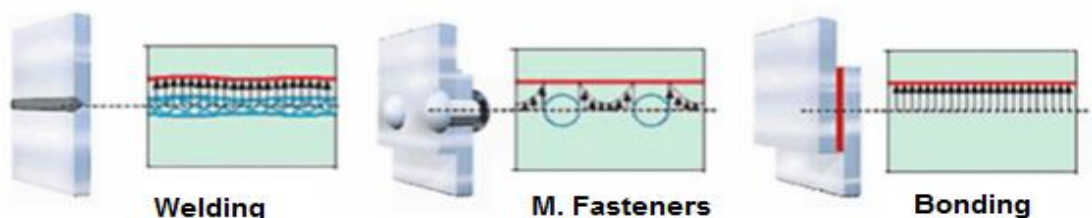


Figure 1. Stress concentration effects for various joints [15].

In this study, various experimental specimens have produced with different repair parameters. Then, by performing unidirectional tensile testing to these prepared specimens, the ultimate failure loads of them

were indicated. By analysing these failure loads of the specimens, the effects of repair parameters have been specified.

2. Experimental

The current work investigated the performance of the external bonded patch repairs under tensile loading by indicating the ultimate failure loads of repaired laminated composite structures. For this study, eight plies laminated woven glass and carbon fibres reinforced parent plates were used. By using these parent plates, experimental specimens were prepared. 10 mm holes were drilled in the centre of the parent plates to simulate the damages in the structures. Then, these damaged specimens were repaired by using adhesive and composite patches with different parameters in laboratory conditions. Two different bonding patch type were used for external bonding patch repair of the specimens. These were wet lay out patches and prepreg patches. Test specimens were prepared in necessary curing temperatures and laboratory conditions. By performing the unidirectional tensile test to these specimens, the ultimate failure loads of these repaired specimens were indicated. The repaired experimental specimens were shown in Fig. 2. The materials that used for parent plate specimens, adhesives and patches in repair were listed in Table1. During the tests, specimens were subjected to longitudinal tensile loads on tensile testing machine in order to indicate the failure loads of repaired structures.

Table 1. Materials that were used in repair of laminated composite materials

Bonding type	Parent Materials	Adhesive	Patch Material
W.L.	Woven carbon fibres	Hysol EA9396	0020989
	Woven glass fibres	Hysol EA9396	0021438-09
Prepreg	Woven carbon fibres	C992275 ADH FILM	C992268-14
	Woven glass fibres	C991957-37 ADH FILM	C992270



Figure 2. Presentation of repaired experimental specimens

3. Results and discussion

3.1. Effect of patch thickness

The effect of the patch thickness to the ultimate failure loads of repaired structure was indicated in Fig. 3. The ultimate failure loads of the structures repaired with prepreg bonding technique were increased by increasing the patch thickness (increase the ply number). But, for the structure that repaired with W.L. bonding technique, the failure loads have increased gradually to the patch thickness of the 3 plies values and after that, the peeling effect has occurred in repaired structure than, the failure load decrease dramatically. Increase the bonded patch thickness after a certain value (3 plies) in repair of the laminate composite materials does not improve the ultimate failure load. Increase the patch thickness further in

repair of air craft structures may cause the weight stability effect. This is the main drawback in repairs of such applications.

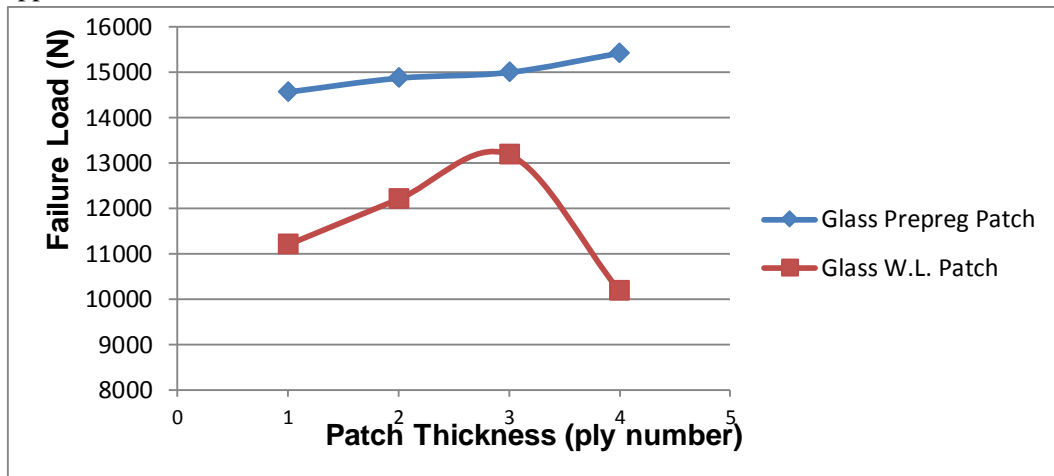


Figure 3. Effect of patch thickness to the failure load of repaired structures with glass prepreg and wet layout patches.

3.2.Effect of bonding length

In external bonded patch repairs, if the patch overlap length or bond length too short, the entire adhesive layer is under high shear stress. In the case of longer bond length, most of the load is carried at the ends of the bonded overlap which is the reason for why too large patches fails to enhance the expected ultimate strength [14]. Effect of bonding length of the patch to failure loads in repaired structures has presented in Fig. 4. The failure loads of structures repaired with glass prepreg patches bonding were increased gradually by increasing the bonding length in repair. In that repair with glass W.L. patch bonding; the failure loads were increased to the bonding length of 40 mm gradually, than decrease dramatically to the 5850 N value due to peeling effect that presented in W.L. applications. In bonded patch repair, for both W.L. and prepreg patches, 40 mm value of bonding length, was seen as the optimum value.

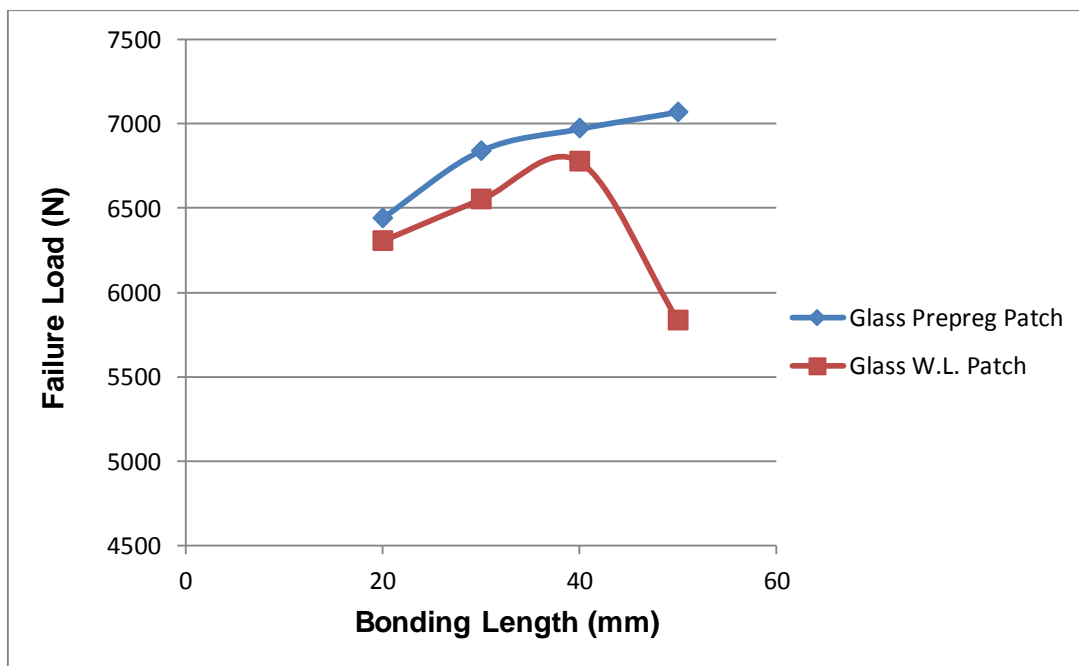


Figure 4. Presentation of the effect of bonding length to the failure load of W/D=2 glass repaired structures with glass prepreg and wet layout patches.

3.3. Effect of bonding area (W/D ratio)

Effect of bonding area (W/D ratio) to the ultimate failure loads was presented in Fig. 5. By changing the W/D ratio from 2 to 4 in repair with carbon fibres prepreg, the failure loads of the repaired laminated plates have been changed from 20000 N to 50000 N value. In repair of woven laminated composite materials, the change of W/D ratio has major effect in ultimate failure loads of repaired parent plate materials. Increase the W/D ratio further in repair of structures may cause the weight stability effect. For this reason, in repair of laminated composite materials the W/D ratio should be in optimum value.

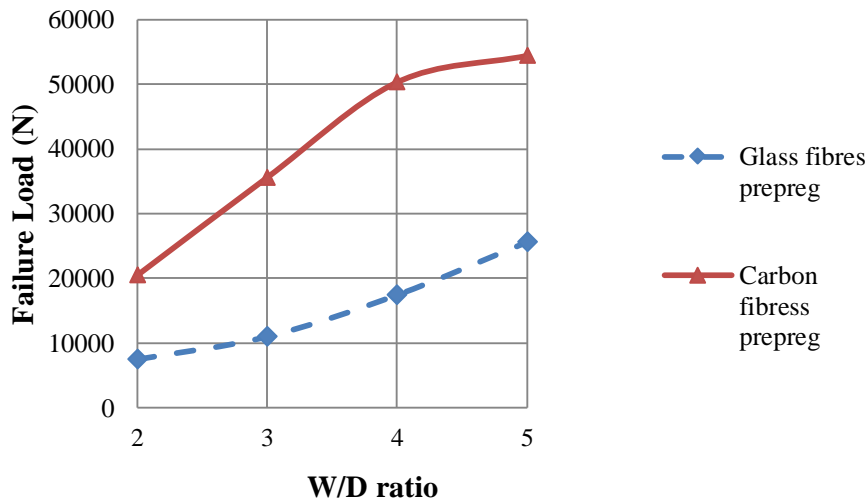


Figure 5. Presentation of the effect of W/D ratio to the failure load glass and carbon fibres reinforced plates repaired structures with glass and carbon prepreg patches.

3.4. Effect of adhesive thickness

The adhesives, which bond the patches and parent plates together, are always regarded as the weakest chain in the bonded repair, and play an essential role. Therefore, careful selection of its parameters is very important [1]. In this study, effects of adhesive thickness were studied with the W/D=3 carbon parents laminated composite specimens that repaired with carbon prepreg patches by using various adhesive film thicknesses. The effect of adhesive thickness in repair of laminated composite materials with external bonded patch to the ultimate failure loads was illustrated in Fig. 6. For each adhesive film ply thickness was taken as 0.2 mm. The maximum ultimate failure load (40750N) was obtained with 3 plies adhesive thickness (0.6 mm) in repair of woven carbon fibres laminated parent plates with external carbon prepreg bonded patches.

The adhesive material which bonds the patch to the parent laminate is considered as the most important factor in the patch bonding repair design. If the adhesive layer is too thin, it will be stiff and brittle which can result to a shear failure initiation in high stress regions near the patch and hole edges, causing the damage propagates across the entire overlap region. However, if the adhesive layer is too thick, it will be too plastic and under loading it is expected to deform quickly which weakens the effectiveness of load transfer between the parent laminate and patches [14].

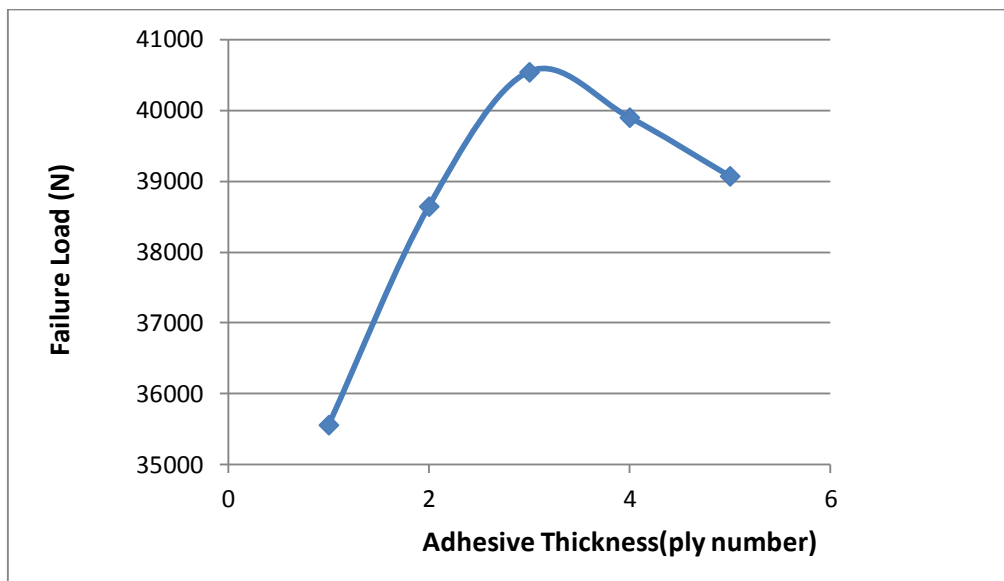


Figure 6. Presentation of the effect of adhesive thickness to the failure load of W/D=3 carbon parent laminated composite that repaired with carbon prepreg patches.

4. Conclusions

In the present study, experimental study is carried out to investigate the effect of different repair parameters on the ultimate failure load of adhesively bonded repaired structures, and the following conclusions can be drawn from this study.

1. The ultimate failure loads of the structures repaired with prepreg patches bonding technique were increased by increasing the patch thickness. But, for the structure that repaired with W.L. bonding technique, the failure loads have increased gradually to the patch thickness of the 3 plies values and after that, the peeling effect has occurred easily and this decrease the failure loads of repaired structures.
2. In external bonded patch repair, for both W.L. and prepreg patches, 40 mm value of bonding length, was seen as the optimum value for obtaining maximum ultimate failure load of repaired specimens.
3. Ultimate failure loads of repaired structures can be increased by choosing the optimum repair parameters, such as patch dimensions, adhesive thickness, bonded area and bonding length.
4. In repair of air craft structures, due to weight stability, optimum quantity of repair materials should be used.

References

- [1] Liu X., Wang G. (2007). Progressive failure analysis of bonded composite repairs. *Composite Structures*, 81, 331-340.
- [2] Papanikos P., Tserpes K.I., Pantelakis Sp.(2007). Initiation and progression of composite patch debonding in adhesively repaired cracked metallic sheets. *Composite Structures*, 81, 303-311.
- [3] Xiaoquan C., Baig Y., Renwei H., Yujian G., Jikui Z., (2013). Study of tensile failure mechanisms in scarf repaired CFRP laminates. *International Journal of Adhesion & Adhesives*, 41, 177-185.



- [4] Breitzman T.D., Larve E.V., Cook B.M., Schoeppner G.A., Lipton R.P. (2009), Optimization of a composite scarf repair patch under tensile loading. *Composites: Part A*, 40, 1921-1930.
- [5] Tse P.C., Lau K.J., Wong W.H. (2002), Stress and failure analysis of woven composite plates with adhesive patch-reinforced circular hole. *Composites: Part B*, 33, 57-65.
- [6] Jones R., Chiu W.K. and Smith R., (1995), Airworthiness of Composite Repairs: Failure Mechanisms. *Engineering Failure Analysis*, 2, 117-128.
- [7] Cheng P., Gong X. J. , Hearn D., Aivazzadeh S., (2011), Tensile behaviour of patch-repaired CFRP laminates. *Composite Structures*, 93, 582-589.
- [8] Her S. C. (1999), Stress analysis of adhesively-bonded lap joints. *Composite Structures*, 47, 673-678.
- [9] Campilho R.D.S.G., Moura M.F.S.F., Domingues J.J.M.S., (2009), Numerical prediction on the tensile residual strength of repaired CFRP under different geometric changes. *International Journal of Adhesion & Adhesives*, 29, 195-205.
- [10] Wisnom M. R., (1999), Size effects in the testing of fibre-composite materials. *Composites Science and Technology*, 59, 1937-1957.
- [11] Madani K., Touzain S., Feugas X., Cohendouz S., Ratwani M., (2010), Experimental and numerical study of repair techniques for panels with geometrical discontinuities. *Computational Materials Science*, 48, 83-93.
- [12] Goyal V.K., Johnson E.R., Goyal V.K., (2008), Predictive strength-fracture model for composite bonded joints. *Composite Structures*, 82, 434-446.
- [13] Davis M., Bond D., (1999), Principles and practices of adhesive bonded structural joints and repairs. *International Journal of Adhesion & Adhesives*, 19, 91-105.
- [14] Caminero M.A., Pavlopoulou S., Lopez-Pedrosa M., Nicolaisson B.G., Pinna C., Soutis C., (2013), Analysis of adhesively bonded repairs in composites: Damage detection and prognosis. *Composite Structures*, 95, 500-517.
- [15] Loctite Worldwide Design Handbook, (1988).
- [16] Turan K., Kaman M.O.,(2016), Experimental Failure Analysis of Wet-Patch-Repaired U Notched Composite Plates. *European Journal of Technic*, 6, 91-98.



DYNAMIC MODEL AND CONTROL OF 2-DOF ROBOTIC ARM

*Mesut HÜSEYİNOĞLU^{*1}, Tayfun ABUT²*

^{*1} Department of Mechanical Engineering, Dicle University, Diyarbakır, Turkey

² Department of Mechanical Engineering, Mus Alparslan University, Mus, Turkey

*Corresponding author; mesuth@dicle.edu.tr

Received: 15 December 2018; Accepted: 29 December 2018

Robotic is a relatively young field of modern technology that exceeds traditional engineering boundaries. Control of the robots is important due to the fact that it has a usage area in many areas. In this study, modelling and control of two degrees of freedom (2-DOF) robotic arm were carried out. Lagrange-Euler method was used to obtain the dynamic equations of the robot. The system was controlled in the simulation environment. Sliding-Mode Control (SMC) and Proportional-Integral-Derivative (PID) control methods were proposed to control the 2 DOF robotic arm. The saturation function is used for the chattering problem of the sliding mode control method. Both process noise and measurement noise have been applied to control the robot in conditions close to the actual ambient conditions. The control methods applied according to the results of the simulation environment were compared and the results were examined.

Key words: Sliding Mode Control, PID Control, Dynamic Model, 2-DOF Robotic Arm

1. Introduction

Robotic applications are widely used in engineering and technology. It is well known that industrial robots are complex, dynamically coupled, high time-dependent and high nonlinear systems. These robots are commonly used in tasks such as welding, paint spraying, correct positioning systems, etc. In these tasks, the gripper of the robotic manipulators is required to move from one place to another or to follow certain trajectories as closely as possible. The motion control of robots is difficult due to uncertainties such as load changes, friction and external disturbances, and a highly non-linear mapped and time-varying system. Therefore, the trajectory tracking problem is the most important and fundamental task in the control of robot manipulators. Many methodologies and controllers in the literature [1-5] have been developed and implemented in order to maintain precise position control and

stability in industrial robots. Hsu and Fu [6] proposed an adaptive decentralized controller for trajectory monitoring of robots. The controller cannot be fully designed for every robot joint as the control inputs and all robot connections are interconnected. Yang et al. [7] have added a disturbance monitor to the adaptive decentralized controller to compensate for the combined uncertainties for each joint. The limitation of the control system has been achieved by using only some special nonlinear damping terms. The fuzzy logic-based generalized prediction control structure is applied for a robotic arm in which a study fuzzy logic-based control algorithms are preferred [8]. A robust adaptive synchronization motion controller for a 2-DOF manipulator is proposed by Dou and Wang [9]. Yao et al. [10] developed a robust adaptive controller but neglected the effects of external disturbances and non-linear friction forces. Wijesoma [11] combined variable torque control and variable structure control to implement monitoring control. Mendes and Neto [12] introduce an adaptive fuzzy control that is integrated into a hybrid force/motion control system of an industrial robot to deal with a scenario of contact between the end-effector of the robot and a given surface. Although the improved controller has relatively high stability and robustness, the controller requires a high calculation load for practical application and cannot be used for trajectory monitoring control. He et al. [13] developed an adaptive controller based on artificial neural networks to address exogenous disorders and model uncertainties of an n-DOF robot manipulator. An adaptive neural impedance controller with input saturation was designed in [14] to satisfy the model uncertainties of a robotic manipulator. Nikdel et al. [15] developed an adaptive controller to improve the tracking performance of a robotic manipulator. The proposed controller also guarantees the system stability in the existence of nonlinearity and parameter uncertainties.

The main targets in designing robot control systems are stability and low tracking error. In this study, dynamic modelling and control of a 2-DOF robotic arm were carried out. Lagrange-Euler method [16] is used to obtain the dynamic equations. The Sliding-Mode Control (SMC) and Proportional-Integral-Derivative (PID) control methods are proposed to control the robotic arm. The control methods applied according to the results of the simulation environment were compared and their results were examined. In the next chapter, the dynamic model of the robotic arm is developed. Then, the controller design is demonstrated with numerical simulations. Finally, an overall evaluation of the results obtained is presented.

2. Dynamic model

The dynamic model is important as it is used in robot design, simulation and control. It is necessary to obtain the dynamic equations to implement high-performance controllers in the control of a robot. The robot which is considered in this study consists of 2 rotary joints. The dynamic model obtained by using Lagrange-Euler [16] method is given below in closed form.

$$M(q)[\ddot{q}] + C(q, \dot{q})[\dot{q}] + G(q)[q] = \tau - \tau_e \quad (1)$$

$$\tau_e = J^T F_{tot} \quad (2)$$

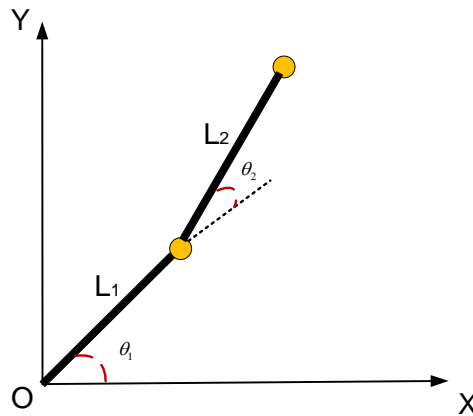


Figure 1. The model of the 2-DOF robotic arm

where, q , \dot{q} , \ddot{q} and τ represent position, velocity, acceleration and control torque, respectively. $M(q) \in R^{3 \times 3}$, $C(q) \in R^{3 \times 3}$ and $G(q) \in R^{3 \times 3}$ show inertial, forces of Coriolis-centrifugal and gravity matrices, respectively. τ_e represents the torque corresponding to the disturbing forces acting on the system from the environment. J shows the Jacobian matrix and F_{tot} shows the disturbing forces affecting the system. The model of the 2-DOF robotic arm is shown in Fig. 1.

3. Controller design

The SMC and PID control methods were used in the position control. These methods were used in various studies in the literature [17-18]. The aim of the control systems is that the output value of the system follows the reference value. The difference between reference and output values in the system is called the error value. Controllers are tried to minimize the error.

3.1. PID control

PID control method shows the best performance although it is an old method used in many control applications [19]. In Eq. (3), the fundamental mathematical expression of the PID method is seen [19].

$$u(t) = K_p e(t) + K_I \int_0^{\tau} e(t) dt + K_D \frac{d}{dt} e(t) \quad (3)$$

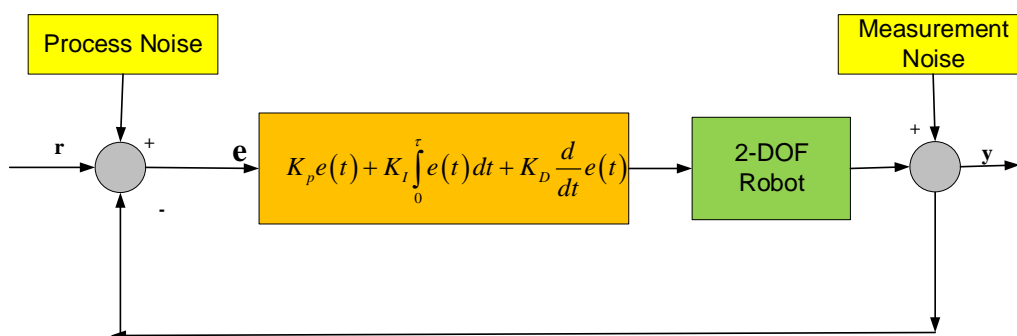


Figure 2. Block diagram of the PID feedback system

where, u , K_p , K_i , K_d and e are called the controller output, proportional gain, integral gain, differential gain and the error signal, respectively. Block diagram of the PID feedback system is shown in Fig. 2.

Ziegler-Nichols method was used to find the PID coefficients and closed-loop control type was used in this study. The control parameters obtained by the Ziegler-Nichols method are given in T ab. 1.

Table 1. Control parameters obtained by the Ziegler-Nichols method

Control	K_P	K_I	K_D
P	$0.5 \cdot K_{cr}$	∞	0
PI	$0.4 \cdot K_{cr}$	$0.8 \cdot P_{cr}$	0
PID	$0.6 \cdot K_{cr}$	$0.5 \cdot P_{cr}$	$0.125 \cdot P_{cr}$

Each period of the output system oscillation and the maximum gain of the oscillation are shown P_{cr} and K_{cr} , respectively.

3.2. SMC method

SMC method which is used for the control of robots in various studies [20-23] was also used in this study. The joint angles of the robot were taken into account as the control variables of the system. The joint angles of the robot were checked in the presence of disturbing effects. Fig. 3 shows the block diagram of the SMC method.

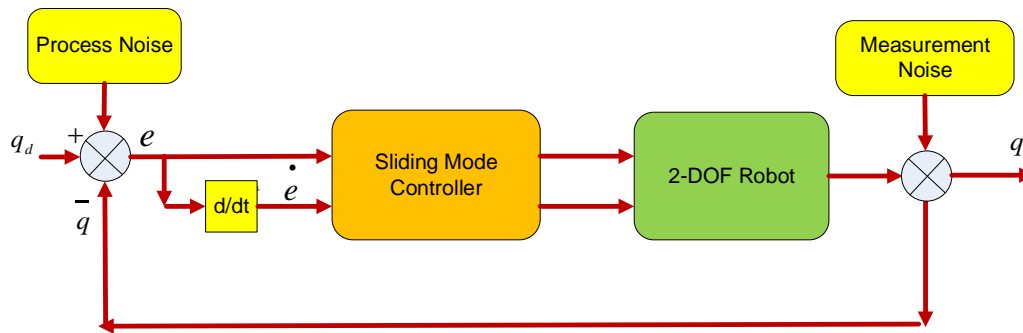


Figure 3. Control structure of the SMC method.

Error and time derivative of the error are given in Eq. (4) and Eq. (5), respectively.

$$e(t) = q_d(t) - q(t) \quad (4)$$

$$\dot{e}(t) = \dot{q}_d(t) - \dot{q}(t) \quad (5)$$

In the above equation, q_d denotes the desired joint trajectory and q shows the true trajectory. The first and second degree derivatives were used for the Eq. (4).

$$S = \dot{e} - \lambda e \quad (6)$$

$$\dot{S} = \ddot{e} - \lambda \dot{e} \quad (7)$$

where, S represents the sliding surface and λ is a positive defined symmetric matrix, u control signal is given in Eq. 8. The concept of sliding surface is shown in Fig. 4.

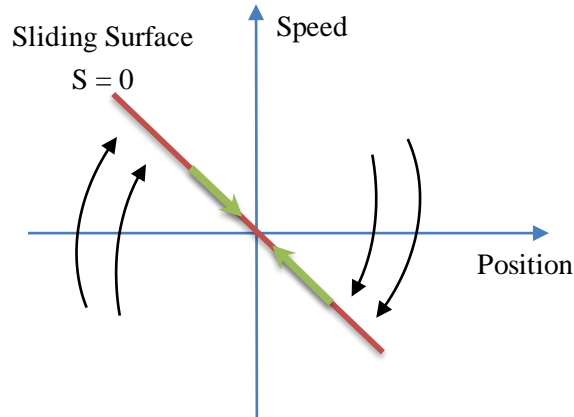


Figure 4. The concept of sliding surface.

$$u = -k \times \text{sign}(s)$$

$$\text{sat}(s/\phi) = \begin{cases} \frac{s}{\phi} & \text{if } \left| \frac{s}{\phi} \right| \leq 1 \\ \text{sign}\left(\frac{s}{\phi}\right) & \text{if } \left| \frac{s}{\phi} \right| > 1 \end{cases} \quad (8)$$

Saturation function is used to solve the chattering problem, ϕ shows the thickness of the boundary layer, k is the constant parameter and sign is a signal function and s functions as a switch. Lyapunov criteria was used for the stability of the system.

4. Simulations

In this section, simulation studies were performed by using the dynamic equations and the performance values of the control methods are given graphically. The SMC and PID control methods are tested for their performance. Control variables are angles of θ_1 and θ_2 which are the basic axes of the 2-DOF robotic arm. The simulation run time was selected 30 seconds. Uncontrolled graphics of θ_1 and θ_2 are given in Fig. 5 and Fig. 6.

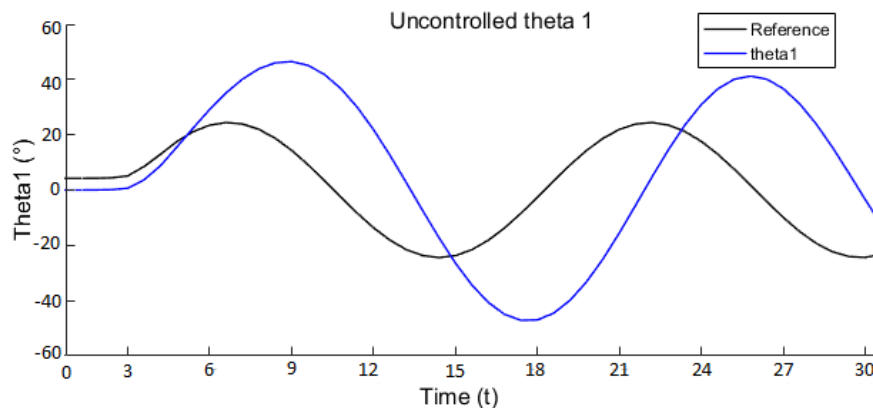


Figure 5. Uncontrolled graphic of θ_1

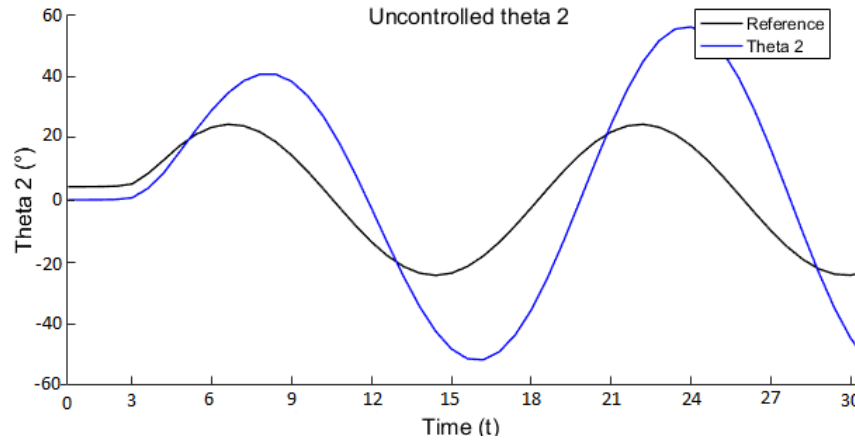


Figure 6. Uncontrolled graphic of θ_2

As seen in the Fig. 5 and Fig. 6, θ_1 and θ_2 don't follow the reference inputs. Responses of θ_1 and θ_2 belong to PID and SMC control methods and error graphics are shown in Figs. 7-14, respectively.

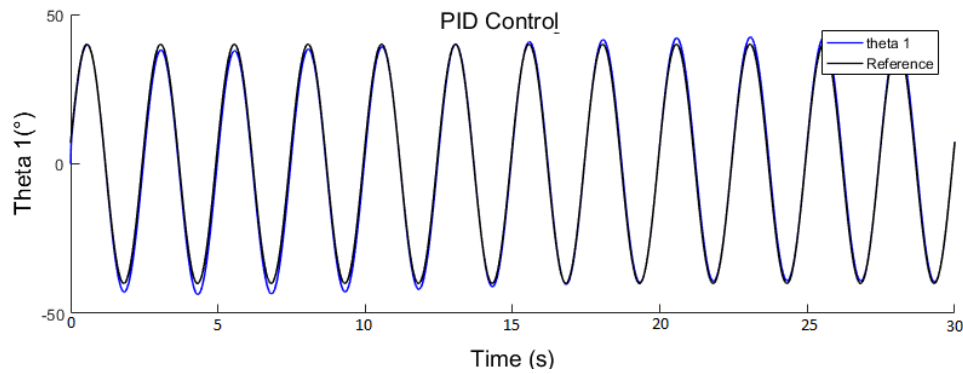


Figure 7. θ_1 angle response obtained through the PID control method

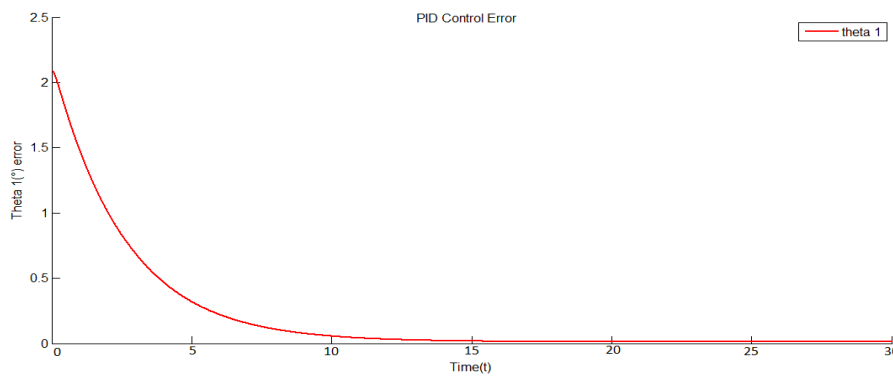


Figure 8. θ_1 angle error response obtained through the PID control method

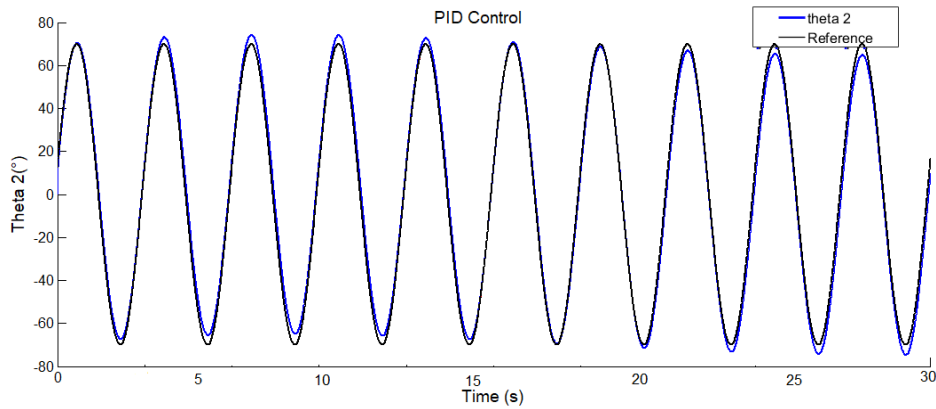


Figure 9. θ_2 angle response obtained through the PID control method

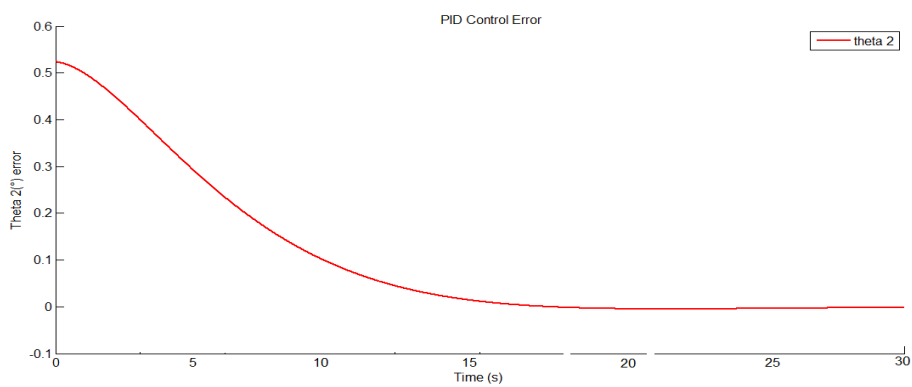


Figure 10. θ_2 angle error response obtained through the PID control method

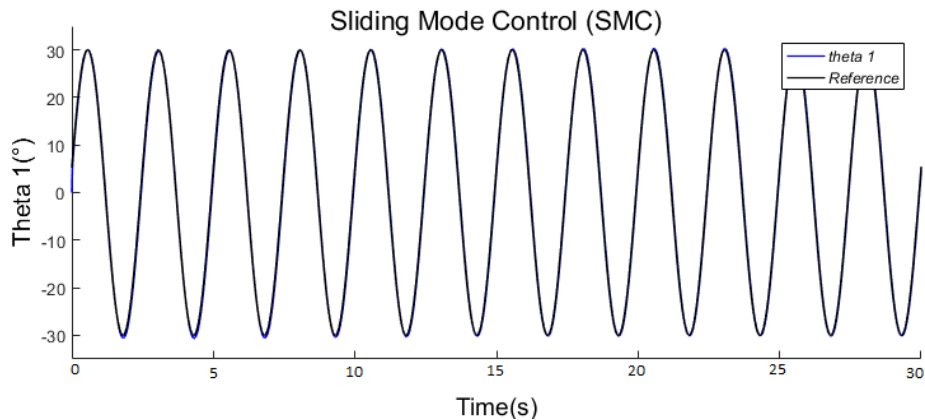


Figure 11. θ_1 angle response obtained through the SMC method

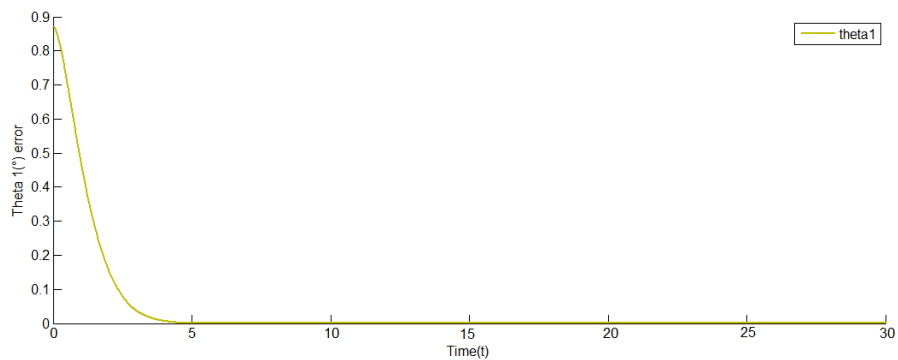


Figure 12. θ_1 angle error response through the SMC method

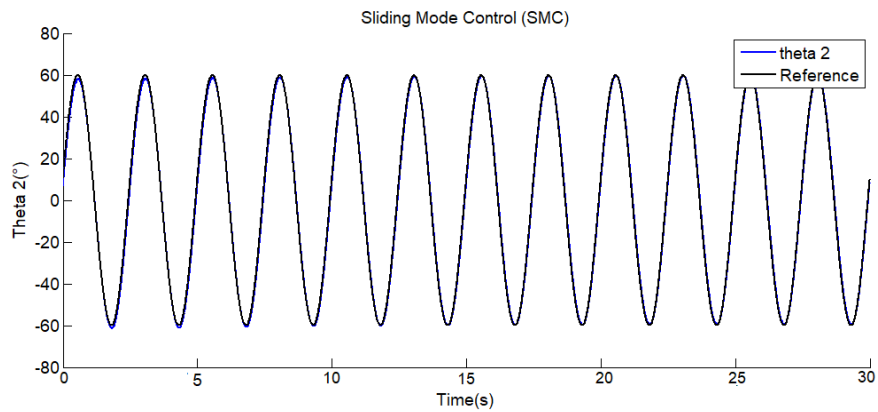


Figure 13. θ_2 angle response obtained through the SMC method

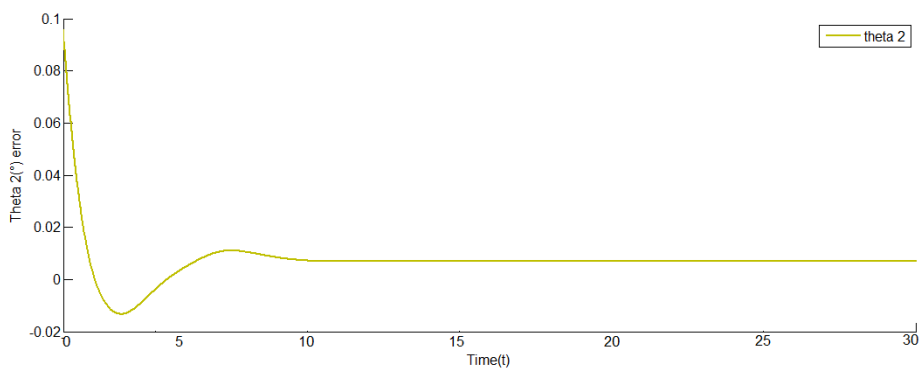


Figure 14. θ_2 angle error response obtained through the SMC method

Fig. 15 and Fig. 16 show the torque graphics required for the 1st joint and the 2nd joint.

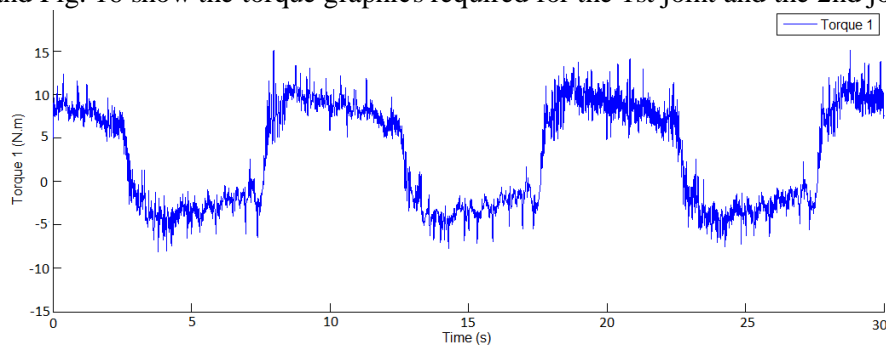


Figure 15. Torque graphic for θ_1 angle

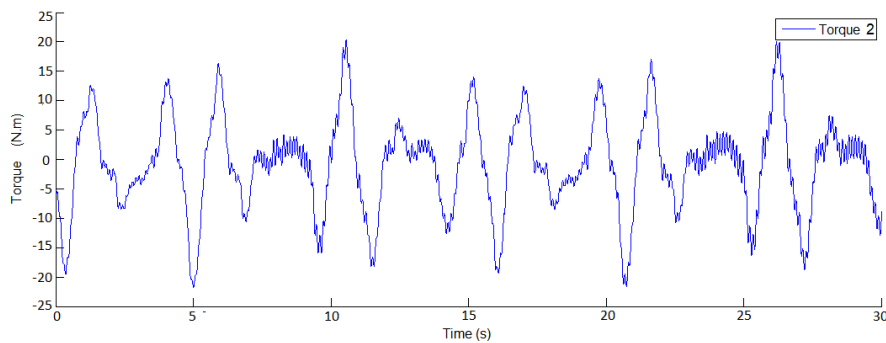


Figure 16. Torque graphic for θ_2 angle

As seen in figures, the PID control method generally followed the reference with greater amplitude. The PID control method has a greater settling time when considering error graphics. Similarly, as can be seen from the error graphs, SMC method gives good performance results according to PID control method.

5. Results and discussions

In this study, dynamic model of 2-DOF robotic arm was obtained by using Lagrange-Euler method. SMC and PID control methods were used for the control of the robotic arm. The performance of these control methods is shown in numerical studies that are performed in simulation environment. It has been seen that the chattering problem of SMC method is solved by saturation function. Both the signal noise and the measurement noise were applied to the signals in order to simulate the actual ambient conditions. A second order low pass filter is applied to increase the performance of the controllers in the noise environment. The cut-off frequency, damping ratio and initial run for the second order low pass filter are taken into account as 100 rad/s, 1 and 0, respectively.

As a result of the comparison of the control methods, it was observed that the controllers gave satisfactory results. The SMC method gave the best results. It is aimed to apply the proposed methods and a real system in future studies.

References

- [1] Pan, L., Gao, T., Xu, F., Zhang, L., Enhanced Robust Motion Tracking Control for 6 Degree-of-freedom Industrial Assembly Robot with Disturbance Adaption, *International Journal of Control, Automation and Systems*, 16 (2018), 2, pp. 921-928
- [2] Meng, D., Moore, K. L., Robust Iterative Learning Control for Nonrepetitive Uncertain Systems, *IEEE Transactions on Automatic Control*, 62 (2017), 2, pp. 907-913
- [3] Chaudhary, H., Panwar, V., Prasad, R., Sukavanam, N., Adaptive Neuro Fuzzy Based Hybrid Force/Position Control for an Industrial Robot Manipulator, *Journal of Intelligent Manufacturing*, 27 (2016), 6, pp. 1299-1308
- [4] Lochan, K., Roy, B. K., Control of Two-link 2-DOF Robot Manipulator Using Fuzzy Logic Techniques: A Review, *Proceedings*, 4th International Conference on Soft Computing for Problem Solving, Warsaw, Poland, 2014
- [5] Piltan, F., Nabae, A., Ebrahimi, M., Bazregar, M., Design robust fuzzy sliding mode control technique for robot manipulator systems with modeling uncertainties, *International Journal of Information Technology and Computer Science*, 5 (2013), 123-135
- [6] Hsu, S. H., Fu, L. C., Adaptive decentralized control of robot manipulators driven by current-fed induction motors, *IEEE/ASME Trans. Mechatronic*, 10 (2005), 4, pp. 465-468
- [7] Yang, Z. J., Fukushima, Y., Qin, P., Decentralized adaptive robust control of robot manipulators using disturbance observers, *IEEE Transactions on Control Systems Technology*, 20 (2012), 5, pp. 1357-1365



- [8] Cronin, J., Escano, J. M., Roshany-Yamchi, S., Canty, N., Fuzzy-Based Generalized Predictive Control of a Robotic Arm, *Proceedings, 25th IET Irish Signals & Systems Conference*, 2014
- [9] Dou H. B., Wang, S. P., Robust adaptive motion/force control formation synchronization of multiple uncertain two-link manipulators, *Mechanism and Machine Theory*, 67 (2013), pp. 77-93
- [10] Yao, J. Y., Jiao, Z. X., Yao, B., Shang, Y. X., Dong, W. B., Nonlinear adaptive robust force control of hydraulic load simulator, *Chinese Journal of Aeronautics*, 25 (2012), pp.766-775
- [11] Wijesoma, S. W., Richards, R. J., Robust Trajectory Following of Robots Using Computed Torque Structures with VSS, *International Journal of Control*, 52 (1990), 4, pp. 935-962
- [12] Mendes, N., Neto, P., Indirect adaptive fuzzy control for industrial robots: a solution for contact applications, *Expert Systems with Applications*, 42 (2015), 22, pp. 929-935
- [13] He, W., Chen, Y., Yin, Z., Adaptive neural network control of an uncertain robot with full-state constraints, *IEEE Trans. Cybern.*, 46 (2016), 3, pp. 620-629
- [14] He, W., Dong, Y., Sun, C., Adaptive neural impedance control of a robotic manipulator with input saturation, *IEEE Trans. Syst. Man Cybern.: Syst.*, 46 (2016), 3, pp. 334-344
- [15] Nikdel, N., Badamchizadeh, M. A., Azimirad, V., Nazari, M. A., Adaptive backstepping control for an n-degree of freedom robotic manipulator based on combined state augmentation, *Robotics and Computer-Integrated Manufacturing*, 30 (2017), 44, pp. 129-143
- [16] Hazewinkel, M., *Lagrange equations (in mechanics)-Encyclopedia of Mathematics*, Springer, Netherlands, 1990
- [17] Abut, T., Modeling and Optimal Control of a DC Motor, *Int. J. Eng. Trends Technol.*, 32 (2016), 3, pp. 146-150
- [18] Ziegler, G., Nichols, N. B., Optimum settings for automatic controllers, *Journal of Dynamic Systems, Measurement, and Control*, 115 (1993), 2B, pp. 220-222
- [19] Aström, K. J., Hägglund, T., *PID controllers: theory, design, and tuning*, Instrument Society of USA, 1995
- [20] Bailey, E., Arapostathis, A., Simple sliding mode control scheme applied to robot manipulators, *International journal of Control*, 45 (1987), 4, pp. 1197-1209
- [21] Utkin, V. I., Sliding mode control design principles and applications to electric drives, *IEEE transactions on industrial electronics*, 40 (1993), 1, pp. 23-36
- [22] Utkin, V. I., Chang, H. C., Sliding mode control in electro-mechanical systems, *Mathematical Problems in Engineering*, 8 (2002), 4-5, pp. 451-473
- [23] Bartolini, G., Pisano, A., Punta, E., Usai, E., A survey of applications of second-order sliding mode control to mechanical systems, *International Journal of control*, 76 (2003), 9-10, pp. 875-892



COMPARATIVE PERFORMANCE ANALYSIS OF PHASE DIVISION MULTIPLEXING TECHNIQUES

*Musa ÇIBUK^{*1}, Munip GEYLANI²*

^{*1}Bitlis Eren University, Department of Computer Engineering, Bitlis/Turkey

²Bitlis Eren University, Department of Informatics, Bitlis/Turkey

* Corresponding author; E-mail: mcibuk@beu.edu.tr

Received: 16 December 2018; Accepted: 29 December 2018

The Phase Division Multiplexing (PDM) technique developed for more efficient use of communication resources has recently gain popularity in wireless communication systems. The PDM technique contributes to parallel communication with the multi-channel structure it supports. Unlike the FDM and TDM techniques, which are frequently used in wireless communication, the PDM has two and four channel structures and multiplexes the phase of the signal. It is thought that the performance analyses of the proposed 2 and 4-channel structures will give the researchers an idea of which aspects are superior and where they can be used. In this study, phase division multiplexing structures are analysed and comparative performance analysis are performed and the results are shared.

When PDM structures are analysed, it is seen that 2-channel PDM-BPSK, 2-channel PDM-QPSK and 4-channel PDM-BPSK structures have been developed. In order to compare these structures with each other, graphical user interface has been designed by using MATLAB program and constellation diagrams of each structure have been obtained. Simulation studies of these three structures have been performed by using MATLAB / Simulink program. Simulations have been run with the same system parameters and Bit Error Rate (BER) curves have been obtained. Tolerance ranges have been compared over constellation diagrams and bit error rate curves obtained by simulations have been shared.

As a result of the comparing performed in this study; the 2-channel PDM-BPSK structure is the simplest and least energy required structure. The 4-channel PDM-BPSK structure is advantageous with the number of channels it provides, but it needs the most energy. The 2-channel PDM-QPSK stands out with its symbol / bit rate. It also requires an energy value in the energy range of the other two techniques.

Key words: *PDM-BPSK, PDM-QPSK, phase division multiplexing*



1. Introduction

The multiplexing process is frequently used in communication systems to deliver communication resources to more than one user and to use communication costs more efficiently. In wireless communication, multiplexing is seen mainly by using FDM (Frequency Division Multiplexing) [1-4], TDM (Time Division Multiplexing) [1, 2, 4, 5] or using these two multiplexing techniques together [1, 5, 6]. While the FDM offers multiple communication channels to the users by dividing the frequency band, the TDM makes multiplexing by allocating the communication path to different users at different times by dividing in time. Apart from these two basic approaches, OFDM (Orthogonal Frequency Division Multiplexing) [7-12], which is a derivative of the FDM technique, and CDM (Code Division Multiplexing) which is a logical multiplexing technique [13-15] is used.

Unlike the general multiplexing techniques used in wireless communication systems, phase division multiplexing (PDM) [16-18] is a new multiplexing technique which multiplexing in the phase of the signal. When the PDM technique is examined, it is seen that there are two- and four-channel structures based on BPSK and QPSK modulations. As it is a new technique, making comparative analyses of these structures of PDM would be useful for researchers.

The rest of the work is organized as follows. In the second chapter, PDM structures are mentioned briefly. The simulation studies prepared for PDM structures are shared and comparative analyzes are made. In Chapter 4, the results obtained are shared.

2. Phase Division Multiplexing

Phase Division Multiplexing (PDM) is a new multiplexing technique developed for use in wireless communication systems, which can be used independently or together with multiplexing techniques commonly used [18]. With Phase Division Multiplexing, phase channels are formed by dividing in the signal phase. These phase channels can be assigned separately to users.

The developed PDM has a structure dependent on the type of modulation to be used. The modulation to be used in PDM has a fixed amplitude value such as PSK [19, 20] modulation and is generated by using pairs of signals with a phase difference of 180° from each other. With the PDM, the signal phase of 360° is divided by the number of channels desired to obtain. The constellation diagrams are generated according to the number of phase channels, the modulation level and the possible input conditions. Data communication is performed according to these constellation diagrams.

In the structure formed by symmetric partitioning, signals with different phase values are allocated to each channel. The each channel uses these special signals according to its own data. Because these signals emitted from the channels have the same frequency value, they overlap and a single symbol is received by receiver, which is the vector sum of all these symbols. The PDM is based on the computations and calculation of these overlapping signals, at which point overlap or neutralization may occur. In order to avoid such collision or neutralization, a phase channel is formed in two or multiples of two. In addition, increasing the number of phase channels to be created means that the number of symbols will increase. The large number of symbols to be processed means system complexity and cost. For these reasons, Dual-channel PDM-BPSK, Dual-channel PDM-QPSK and Quad-channel PDM-BPSK structures have been developed.

In the PDM, there is a third "-" state indicating the non-use status of the channels in addition to the "1" and "0" data in the input state. All possible combinations of 3 different input states in

PDM-BPSK structure are $3n$, with " n = number of channels". That is, $3n$ symbol signals are processed. In PDM-QPSK, there are 5 different possible input states such as "00", "01", "10" "11" and the non-use condition of the channel "--". This means that $5n$ symbol signals are processed, which are different from each other as the phase and amplitude to represent all possible input states.

In the Dual-channel PDM-BPSK, the signal phase with 360° is divided into 4 equal parts and the signals opposite to each other are allocated to the same channel. The channels emit these signals according to the data they want to transmit. The sum of these signals forms the constellation diagrams of the PDM structure since both channels simultaneously emit signals. The Dual-channel PDM-BPSK has 9 different input states and each symbol represents a 2-bit data set. The first bit of each symbol represents the 1st channel data and the second bit represents the 2nd channel data. The receiver makes sense of the symbol signal according to the tolerance intervals and separates the data of the channels.

The difference of PDM-QPSK from PDM-BPSK structure is to assign 4 signal values to the generated channels. Thus, 2-bit data can be transmitted from each channel in the QPSK structure. In the Dual-channel PDM-QPSK, the signal phase of 360° is divided into 8 and 4 signals are allocated per channel to each other. In this structure, communication is provided via 4-bit data groups. The first two digits of these data groups represent the data for the first channel and the last two digits represent the data for the second channel. Each symbol in the constellation diagram represents 4-digit data groups consisting of "0", "1" and "-". While all possible combinations of 4-bit data can create 16 different states, 25 different input states are observed due to the non-use of the channel in the Dual-channel PDM-QPSK structure. These 25 different input states are represented by 25 symbol signals each with different amplitude and phase values.

In the Quad-channel PDM-BPSK, the signal phase of 360° is divided into 8 equal parts. The signal pairs with opposite angles are assigned to the same channel. In the Quad-channel PDM-BPSK structure, the 4-bit data groups belonging to a different channel of each digit are communicated. Each symbol in the constellation diagram represents the 4-digit data group consisting of "0", "1" and "-", and 81 different input states are observed. These 81 different input states are represented by 81 symbol signals, each with different amplitude and phase values. The receiver determines which signal is received by the amplitude and phase value of the signal to be received.

3. Simulation

3.1. Graphical User Interface

In this study, a graphical user interface (GUI) has been designed to compare PDM techniques with constellation diagrams and tolerance ranges. This GUI generates the constellation diagram according to the desired input values and determines the tolerance intervals. The Quad-channel PDM-BPSK constellation diagram and the tolerance interval analysis are shown by means of the GUI designed in Figure 1.

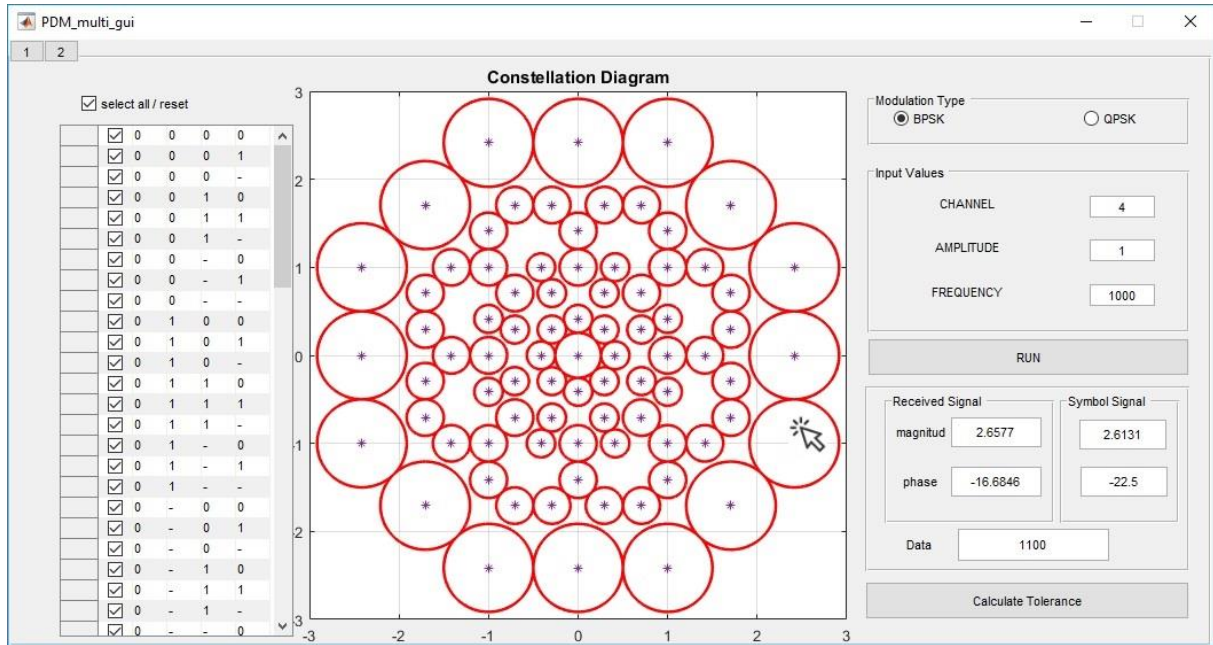


Figure 1. Constellation diagram and tolerance analysis

3.2. Simulation and Comparison

In order to test the performance of PDM structures, dual and quad channel PDM modulators and demodulators have been designed in MATLAB / Simulink environment and simulations have been performed by adding noise factor to the transmission medium. Figure 2, Figure 3 and Figure 4 show the Dual-channel PDM-BPSK, Dual-channel PDM-QPSK and Quad-channel PDM-BPSK simulation models respectively. In addition to the use of ready blocks of Simulink program for simulations, special blocks and functions have been developed to represent the study-specific PDM structure.

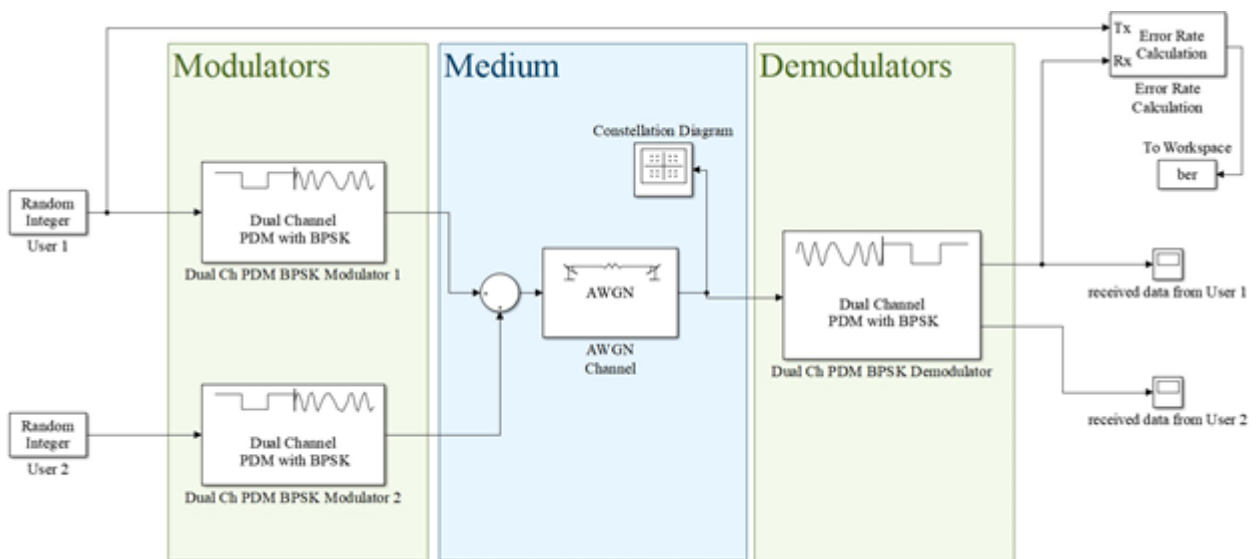


Figure 2. Dual-channel PDM-BPSK simulation

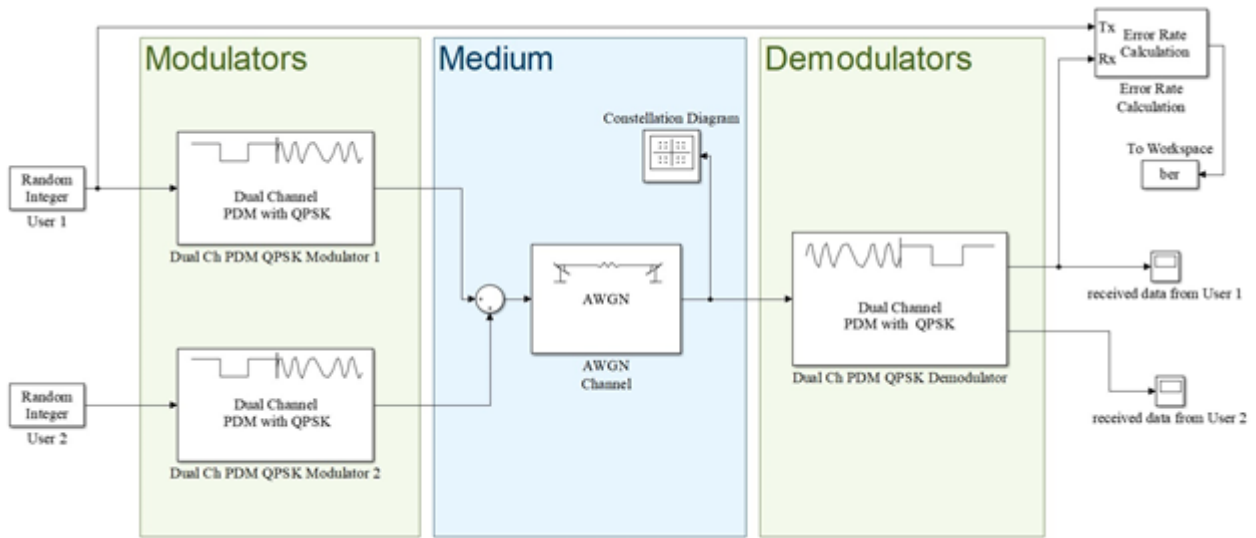


Figure 3. Dual-channel PDM-QPSK simulation

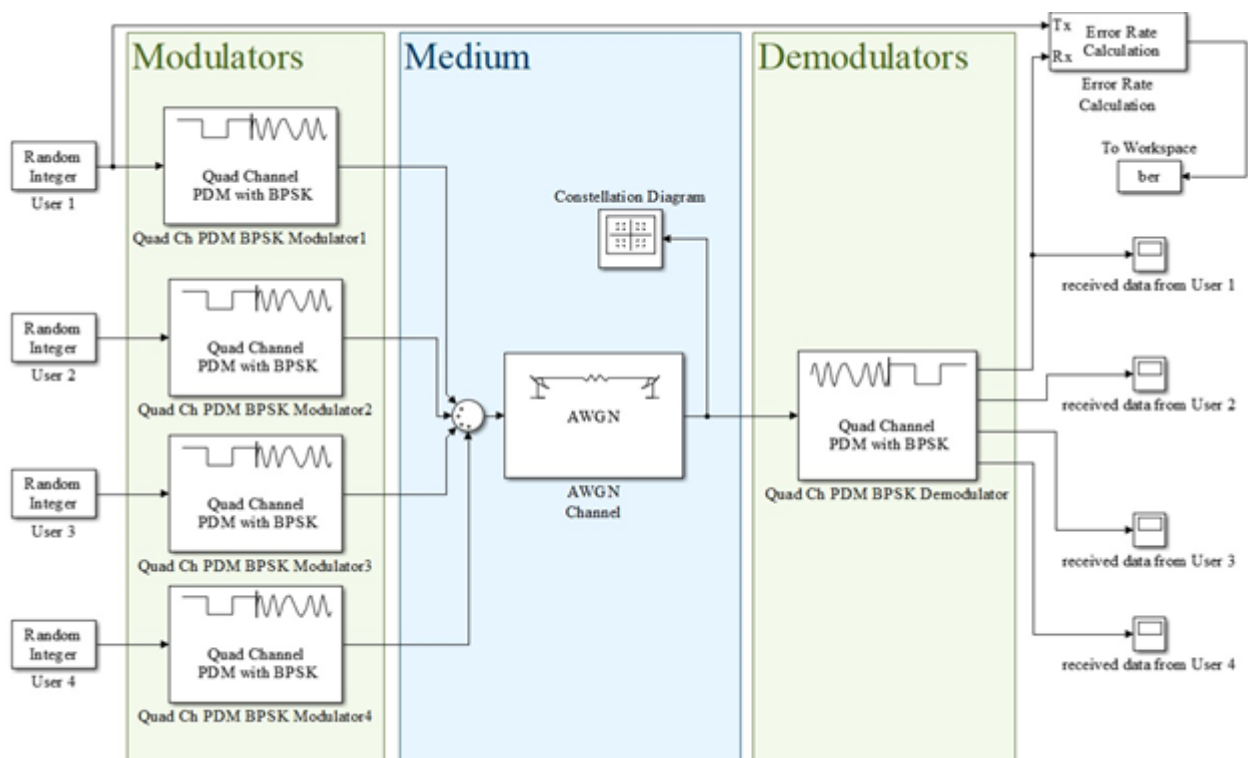
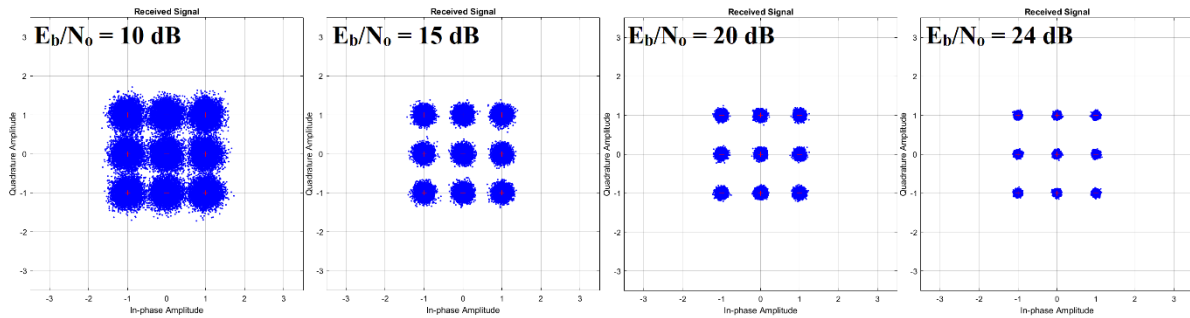


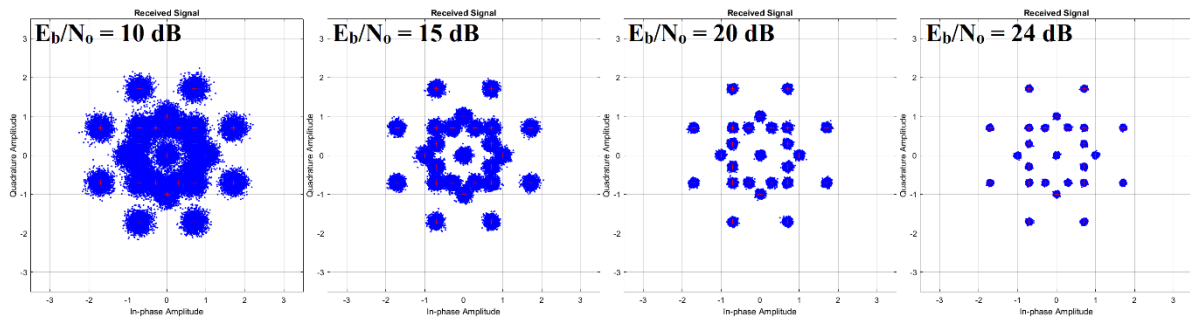
Figure 4. Quad-channel PDM-BPSK Simulation

For “A = signal amplitude assigned to the channels” and “f = operating frequency”, the PDM simulations have been performed with the parameters given below and the resulting clustering diagrams are given in Figure 5.

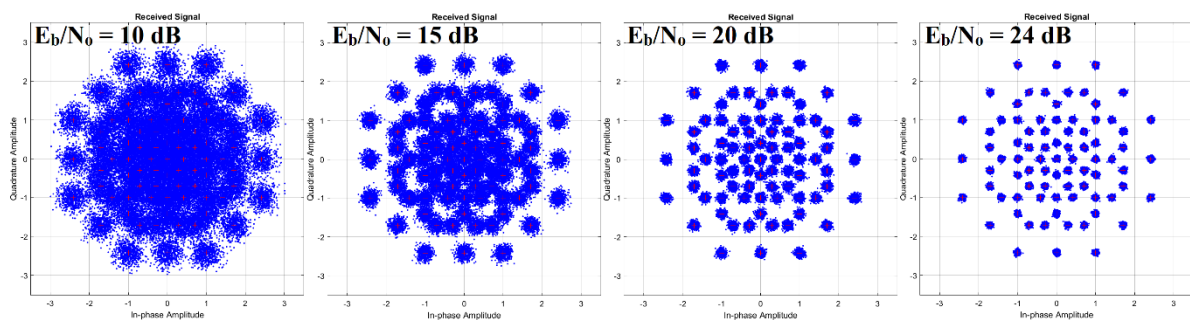
A : 1 V
 f : 100 Hz
 Sample time : 1 μ s
 Symbol period : 1 μ s
 Run Time : 1 s
 E_b/N_o : 10 dB, 15 dB, 20 dB, 24 dB



(a) Dual-channel PDM-BPSK



(b) Dual-channel PDM-QPSK



(c) Quad-channel PDM-BPSK

Figure 5. Constellation diagrams of PDM structures for different E_b/N_o values

As seen in Figure 5, the symbol signals approach each other as the value of E_b/N_o decreases. In this case, the desired performance under a certain value can not be achieved because of the overlap. Symbol signals received for $E_b/N_o = 15$ dB for Dual-channel PDM-BPSK, $E_b/N_o = 20$ dB for Dual-channel PDM-QPSK and $E_b/N_o = 24$ dB for Quad-channel PDM-BPSK are severely separated from each other and grouped within specified tolerance limits.

The Bit Error Rate Analysis Tool (BERTool) tool has been used to calculate BER values corresponding to different E_b / N_0 values with the parameter values specified in the simulations. BER curves for all three PDM structures are shown in Figure 6.

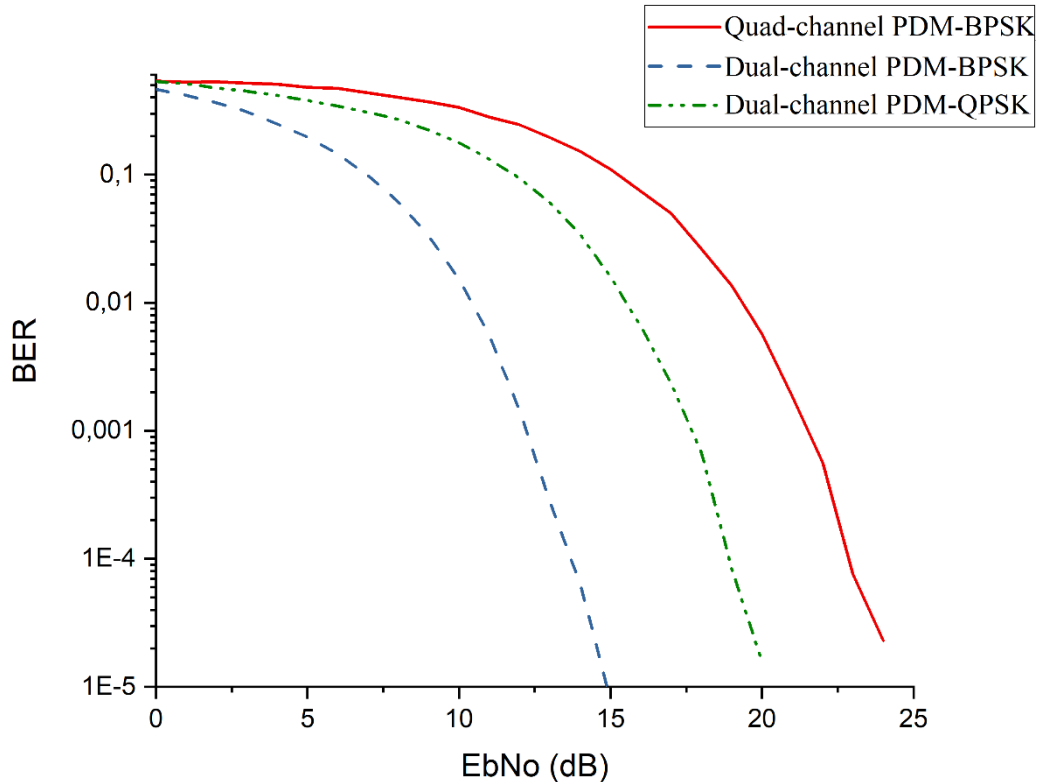


Figure 6. BER performance comparison of PDM structures

As it seen from the graph; as the number of channels increases, the required E_b / N_0 is increasing. Also when higher level modulation is used in PDM, it is seen that the required E_b / N_0 value increases. The reason for this is that when the number of channels increases or the modulation level is increased, the symbol signals that come up are close to each other and their tolerances decrease. The comparison data obtained in the study are summarized in Table 1.

Table1. Pdm Techniques Comparison

	Bit/Symbol Rate	Modulation	Symbol	E_b/N_0 dB (BER=10 ⁻⁵)	Channel
Dual -channel PDM-BPSK	2	BPSK	9	15	2
Dual-channel PDM-QPSK	4	QPSK	25	20	2
Quad-channel PDM-BPSK	4	BPSK	81	24	4

4. Conclusion

In this study, a comparative analysis of PDM, a new multiplexing technique, has been introduced. For this purpose, a graphical user interface has been designed by using MATLAB environment and clustering diagrams of each structure are obtained. Using the MATLAB / Simulink environment, the simulations of these three structures are made and the results of the simulations operated in the same parameters are shared. Tolerance ranges are compared over clustering diagrams and bit error rate curves obtained by simulations are shared.

As seen in the study two independent channels are obtained in Dual-channel PDM-BPSK and Dual-channel PDM-QPSK techniques and 4 independent channels are obtained by Quad-channel PDM-BPSK technique. The Dual-channel PDM-BPSK technique requires 25 percent less energy than the Dual-channel PDM-QPSK technique and the Quad-channel PDM-BPSK technique needs 20 percent more energy than the Dual-channel PDM-QPSK technique. In Dual-channel PDM-BPSK and Quad-channel PDM-BPSK techniques, 1 bit can be transmitted from channels simultaneously, while Dual-channel PDM-QPSK technique can be transmitted by 2 bits simultaneously.

As a result, in this study; with the simple structure of the Dual-channel PDM-BPSK, it is seen to be the least energy-require technique. The small number of symbols processed in this case has a great contribution. In this technique, each channel can transmit 1 bit data at the same time. The Quad-channel PDM-BPSK provides the highest number of channels and is also disadvantageous in terms of energy demand. This is the result of the processing of 81 symbols in the Quad-channel PDM-BPSK structure. In this technique, channels can transmit 1 bit data at the same time. Finally, the energy requirement in the Dual-channel PDM-QPSK structure has a value between the two other techniques. In addition, since the channels can transmit 2-bit data at the same time, it can be seen that it comes forward with a symbol / bit rate.

5. References

- [1] White, C., *Data Communications and Computer Networks: A Business User's Approach*, Course Technology Cengage Learning, USA, 2015
- [2] Ryan, M. J., Frater, M., *Communications and Information Systems*, Argos Press P/L, Canberra, Australia, 2002
- [3] Patranabis, D., *Telemetry Principles*, Tata McGraw Hill Education, New Delhi, India, 1999
- [4] Schiller, J. H., *Mobile Communications*, Pearson Education, London, England, 2003
- [5] Stallings, W., *Data and Computer Communications eight edition*, Pearson Education Inc., New Jersey, USA, 2007
- [6] Çıbuk, M., Protocol Design And Implementing for Web Based Bio-Telemetry Applications via Wimax/Ieee802.16 Networks, Ph. D. thesis, Firat University, Elazığ, Türkiye, 2009
- [7] Li, Y. G., Stuber, G., *Orthogonal frequency division multiplexing for wireless communications*, Springer Science & Business Media., Berlin, Germany, 2006
- [8] Al-Tamimi, A. K., Exponential Effective Signal to Noise Ratio Mapping (EESM) Computation for Wimax Physical Layer, Master of Science Thesis, Washington University, Washington, 2007
- [9] Prasad, R., *OFDM for Wireless Communications Systems*, Artech House, Boston&London, England, 2004
- [10] Kaur, S., Bharti, G., Orthogonal Frequency Division Multiplexing in Wireless Communication Systems : A Review, *Int. J. Adv. Res. Comput. Eng. Technol.*, 1 (2012), 3, pp. 125–129



- [11] Rashmi, R., Sarala, S. M., OFDM : Modulation Technique for Wireless Communication, *Int. J. Innov. Res. Adv. Eng.*, 1 (2014), 1, pp. 1–5
- [12] Arrano, H. F., Azurdia-Meza, C. A., OFDM: Today and in the Future of Next Generation Wireless Communications, 2016 IEEE Central America and Panama Student Conference (CONESCAPAN), Guatemala City, Guatemala, 2016, Vol. 1, pp. 1–6
- [13] Hoffmann, C., Code Division Multiplexing, Ph. D thesis, Massachusetts Institute of Technology, Massachusetts, USA, 2004
- [14] Jordan, R., Abdallah, C. T., Wireless. Communications and An Overview, *IEEE Antennas Propag. Mag.*, 44, (2002), 1, pp. 185–193
- [15] Fan, P., Multiple Access Technologies for Next Generation Mobile Communications, *ITS Telecommunications Proceedings*, 2006 6th International Conference, Chengdu, China, 2006, Vol. 1, pp. 10–11
- [16] Geylani, M., Çıbuk, M., Multichannel Approach with Phase Based Multiplexing in Wireless Communication and Its Feasibility, International Conference on Multidisciplinary, Science, Engineering and Technology (IMESET'17 Bitlis), Bitlis, Turkey, 2017, Vol. 1, p. 267
- [17] Geylani, M., Çıbuk, M., Phase Division Multiplexing with 4-level PSK Modulation and Simulation, IDAP 2018: International Conference on Artificial Intelligence and Data Processing'18, Malatya, Türkiye, 2018
- [18] Geylani, M., Improving a New Time-Independent Transmission Technique Using Hybrid Multiplexing Methods in Wireless Sensor Network, Master Thesis, Bitlis Eren University, Bitlis, Türkiye, 2018
- [19] Tomasi, W., Atakay, M., *Elektronik İletişim Teknikleri*, MEB Yayınları, Ankara, Türkiye, 2002
- [20] Sharma, D. K., *et al.*, Analog & Digital Modulation Techniques: An Overview, *Tech. Int. J. Comput. Sci. Commun. Technol.*, 3, (2018), 1, pp. 551–561



ENERGY POTENTIAL OF ANIMAL BIOMASS IN TURKEY

K. SAKA^{1*}, İ. H. YILMAZ², A. S. CANBOLAT³, Ö. KAYNAKLI³

¹Vocational School of Yenişehir Ibrahim Orhan, Bursa Uludağ University, Bursa, Turkey,

²Department of Automotive Engineering, Adana Science and Technology University, Adana, Turkey

³Department of Mechanical Engineering, Bursa Uludağ University, Bursa, Turkey

*Corresponding author; kenansaka@uludag.edu.tr

Received: 1 March 2018; Accepted: 12 July 2018

In this study, animal biomass energy potential of Turkey was presented in detail based on the countrywide livestock. Animal biomass resources were examined under three major groups: bovine, small ruminant, and poultry. Bovine animals were described in terms of three different cattle species, buffalo and other species (horse, donkey, camel, mule and pig). Sheep and goat were considered as two subspecies of small ruminant. Poultry consisted of two different chicken species, turkey, goose and duck. The status of animal biomass in Turkey and its exploitation by use of anaerobic digestion and consequent combustion of methane produced for energy production were presented. A detailed analysis was made to determine which animal species has high energy potential of biomass. The potential of energy, waste and the production depending on every single subspecies were indicated in the analyses. The waste coefficients for species were obtained from the biomass energy potential atlas of Turkey and the animal production data reported by the Turkish Statistical Institute. Additionally, energy potential changes in recent years for every single species were calculated. According to the results, bovine animals possess 67.1% of total energy potential, and among bovine animals, cattle has the highest energy potential with 61%. Results indicated that 1.36 million tons of oil equivalent would be exploited by the animal biomass potential of Turkey according to the 2016 data.

Key words: Animal Biomass, Energy Potential, Waste, Species, Turkey

1. Introduction

As a renewable energy source, biomass comes out in different forms (animal, vegetable, municipal solid and forestry) based on biological diversity. This biomass diversity has drawn various communities' attention towards the utilization of bioenergy including biodiesel, bioethanol, biogas, bio

methanol and bio oil especially in developed countries as stressed by Demirbas [1]. A considerable part of the research studies made involves the evaluation of nationwide biomass potential.

India has surplus agricultural and forest area which comprises about 500 million metric tons of biomass availability per year. Renewable energy is contributed 10.5% of total generation out of which 12.83% power is being generated using biomass. In India total biomass power generation capacity is 17,500 MW. At present power being generated is 2665 MW which include 1666 MW by cogeneration [2].

The estimated total amount of biomass resource available for energy in Bangladesh in 2012–2013 is 90.21 million tons with the annual energy potential of 45.91 million tons of coal equivalent. The recoverable amount of biomass (90.21 million tons) in 2012–2013 has an energy potential of 1344.99 PJ which is equivalent to 373.71 TWh of electricity [3].

Alberta's wealth of biomass resources is estimated at 458 PJ potential. Agriculture is a major source for biomass feedstock supply in Alberta. Also, biomass-based energy development has been slow, and its contribution for provincial energy supply has so far been low. Utilization of agricultural and forest biomass resources for energy production can avoid 11-15% of GHG emissions and also substitute 14-17% of final energy demand by 2030. In addition, biomass has the potential to substitute 29% of total electricity consumption or 28% of Alberta total internal load [4].

The most promising biomass feed stocks in Central America are residue based; animal (manure), forest and agricultural origin. Around 250 PJ/year could be available for the energy sector, which is equivalent to 34% of primary energy supply for Central America. It is concluded that in the short term promoting and implementing improved cooking stoves will give the largest improvement in the efficiency of biomass use, whereas on the long term small combustion plants seem to be the best choice for transforming Central America's biomass into a clean and sustainable energy carriers, boosting economy and industrial development. The introduction of improved cooking stoves will result in an annual saving in the range of 4–8 Mt of fuel wood (59–113PJ). Moreover, even when the investment cost of the cooking stoves is considered, improved cooking stoves yield economic savings to fuel wood consumers compared to traditional stoves [5].

The total final energy which could be generated from 22,208,455 t/y of residual biomass assessed in Italy, is equal to 4.57 Mtoe, nearly 2.7% of the gross Italian energy consumption in 2013 and the total savings of GHG emissions coming from this bioenergy generation, are close to 52 Mt CO₂ for the entire Italian territory per year [6].

Rapeseed can be considered for biodiesel production in Croatia because it provides a positive energy return compared with the energy used to produce it. Considering rapeseed oil for biodiesel and meal for animal feed, the energy ratio of the rapeseed production was 3.16, the net energy gain was 50.56 GJ/ha, and the energy productivity was 49.23 L/GJ. The major energy inputs were fertilizers, with 64.9%, and fuel consumption, with 22.8% of the total energy input. On the other hand, labor was an insignificant energy input, with less than 0.1% of the total. Because the reduction of fertilizers would decrease production yields, the reduction of energy input might first be possible with regard to fuel consumption for field operations, especially in soil tillage and transport. The production of rapeseed oil for biodiesel can be a good alternative for Croatian farmers and can have economic, environmental and energy benefits for Croatia [7].

There have been a number of research studies on the determination of biomass potential in Turkey. Sürmen [8] emphasized the significance of biomass for Turkish economy and estimated the

firewood share on the overall energy production to be 21%. Sustainability of biomass was discussed and biomass gasification processes were recommended for Turkey's power generation [9-10].

Yelmen and Cakir [11] emphasized that Turkey has remarkable potential of biomass while it has poor fossil fuel resources. According to the 2004 data, animal waste derived biogas energy potential of Turkey was estimated to be 3 billion m³ per annum [12]. This potential was predicted to be 2.18 billion m³ per annum according to the 2009 data in case of evaluating 121 million tons of animal waste [13]. Balat et al. [14] revealed that the total biomass energy potential of Turkey was about 32 Mtoe of which 17 Mtoe could be evaluated as usable biomass. Erdogdu [15] reported the annual waste amount of animal biomass in terms of animal species. Yilmaz et al. [16] investigated the energy recovery from municipal solid waste in Turkey as landfill gas collection between 2012–2023. The results indicated that about 1% of the energy deficit of the country would be met if all the municipal solid waste potential were put into practice by sanitary landfilling till 2023.

The aim of this study is to determine the animal biomass potential of Turkey in terms of 16 animal species which were classified under three main groups as bovine, small ruminant and poultry. The number of animal for each species was taken from the Turkish Statistical Institute (TurkStat) database, and the corresponding waste production amount based on each species was calculated using the Biomass Energy Potential Atlas (BEPA) of Turkey. The energy exploitation from animal biomass was considered to be methane combustion produced as a result of anaerobic digestion. Additionally, the variation of energy potential between 2010–2016 was demonstrated.

2. Biomass Energy Potential Atlas of Turkey

BEPA of Turkey [17, 18] has been prepared by General Directorate of Renewable Energy (YEGM). In this study, the waste coefficients for each animal species and the energy potentials obtained from BEPA were used as material data. In BEPA, biomass waste resources were classified into four different groups as animal, vegetable, municipal solid and forestry. For every single town within the border of the Republic of Turkey, the total amount of biomass production, the total amount of waste production and the total amount of energy potential based on the waste type are presented in detail. The biomass energy potential of each city of the country is defined to be the cumulative result of those towns locating under the corresponding city. BEPA has a user- friendly and provides online data since 2014 as schematically shown in Fig. 1 but it should be noted that the country population data is compatible with the data two year ago, i.e. 2012 due to the time lag resulting from the colossal biomass data processing. This study takes into consideration the most recent data of animal reproduction reported by TurkStat [19].

3. Waste and Energy Value

There are three main parameters for the calculation of energy potential: the animal production rate, the amount of waste per animal, the amount of energy per unit waste. The energy potential is calculated by multiplying these three parameters. The annual produced waste depends on many factors such as feeding habits, animal physiology, and weather conditions however the waste production for each animal species was taken to be averaged values for simplifying the analyses. Otherwise, collecting real data is not easy in countrywide scale. Energy exploitation from animal manure was considered to be performed by anaerobic digestion which provides to produce methane. The detail of the calculations

is given in our previous study [20] to produce energy from methane. The waste production coefficients and equivalent heating values (as tons of oil equivalent (toe)) used in this study are given in Table 1.



Figure 1. Distribution of culture cattle for cities in Turkey using BEPA interface

Table 1. The Waste Production per Animal and Energy Values per Unit Waste

Species	Waste (kg/year)	Energy (toe/tons)	Species	Waste (kg/year)	Energy (toe/tons)
Domestic cattle	5475	0.0062	Donkey	2737	0.0037
Crossbred cattle	6570	0.0075	Sheep	1095	0.0028
Culture cattle	9125	0.0093	Goat	730	0.0019
Buffalo	7300	0.0087	Hen (Broiler)	27	0.0281
Horse	5475	0.0062	Laying hen	55	0.0281
Mule	4380	0.0049	Turkey	38	0.0281
Pig	730	0.0093	Goose	47	0.0281
Camel	10220	0.0093	Duck	47	0.0281

The annual waste production by crossbred cattle and culture cattle constitutes 81.9% of the countrywide animal waste production. The waste production for bovine was reported to be 20 kg per day by Avcioğlu and Türker [13]. This corresponds to 7300 kg/annum which agree well with the buffalo data given in Table 1.

4. Results and discussion

It is significant to discuss the contribution of the animal species to the total animal biomass production. There is a direct relationship between animal population and waste production which increases with increasing animal weight. Thus, biomass energy potential is rather related to the amount of waste than the number of animals. The animal species becomes a significant parameter as the animal population increases.

Table 2 shows the details of animal biomass and its energy potential according to the 2016 data. The calculations indicated that the waste production by bovine, small ruminant and poultry is 67.2%,

25.4% and 7.4%, respectively. The energy profit from the associated waste production is 67.1%, 8% and 24.9%, respectively. It is clearly seen that although the waste production by small ruminant is higher than that of poultry, its equivalent energy potential is lower than the poultry. 16 livestock were considered to analyze but few of them made considerable effect on the biomass energy potential. Cattle species have the highest contribution to the overall energy exploitation from the animal biomass.

Table 2. The production and waste and energy potential based on animal species in Turkey.

	Production Ratio (%)		Animal count	Waste Percent (%)		Waste (tons/year)	Energy Percent (%)		Energy (toe/year)
Domestic Cattle	11.9		1733292	8.6		9489773	6.4		58836
Culture Cattle	45.3		6588527	54.8		60120308	61		559118
Crossbred Cattle	39.6		5758336	34.5		37832267	30.9		283742
Buffalo and oth.	3.1		454679	2.1		2293573	1.7		15612
Total Bovine	100	3.7	14534834	100	67.2	109735923	100	67.1	917310
Sheep	75		30983933	81.8		33927406	86.9		94996
Goat	25		10345299	18.2		7552068	13.1		14348
Total Sheep	100	10.6	41329232	100	25.4	41479474	100	8.0	109345
Laying Hen	32.6		108689236	49.4		5977908	49.4		167979
Broiler	66.1		220322081	49.1		5948696	49.1		167158
Turkey and oth.	1.4		4529945	1.5		184262	1.5		5177
Total Poultry	100	85.7	333541262	100	7.4	12110866	100	24.9	340315
Total		100	389405328		100	163326265		100	1366971

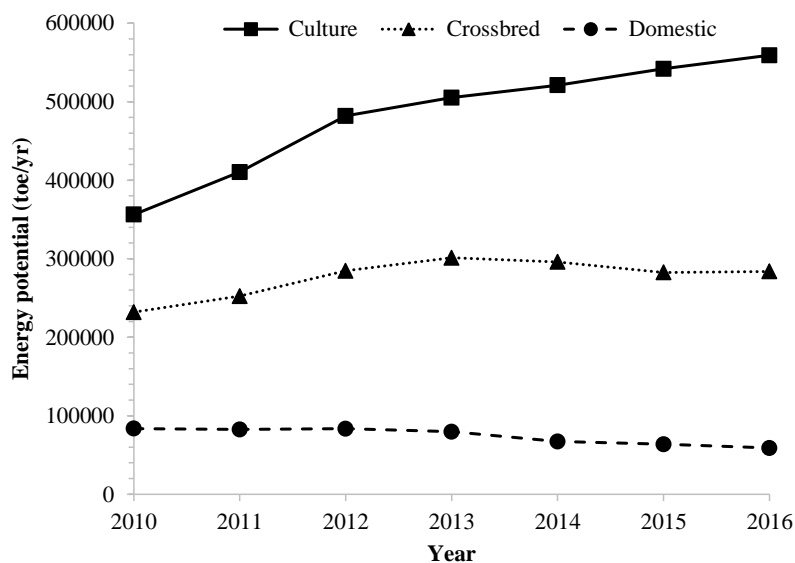


Figure 2. Energy potentials of cattle species.

The culture cattle have the share of 61% on the overall energy potential among total bovine in the countrywide. This potential is significant to be exploited especially in the southwestern part of Turkey as seen from Fig. 1. 1.36 Mtoe would be exploited by the animal biomass potential of Turkey according to the 2016 data.

Another point that was focused in this study is the change of biomass energy potential with time. This would provide to estimate the energy potential in the coming years. As seen from Fig. 2, while the energy potential of culture cattle has an increasing trend, the energy change in the crossbred cattle is almost constant in recent years. On the other hand, the trend for the domestic cattle has decreased recently. It is clearly seen that the energy potential of culture cattle is 6 times and 2 times higher than that of the crossbred and domestic type, respectively. The trend for the buffalo and other bovine animals was not given in the figure due to their low energy content.

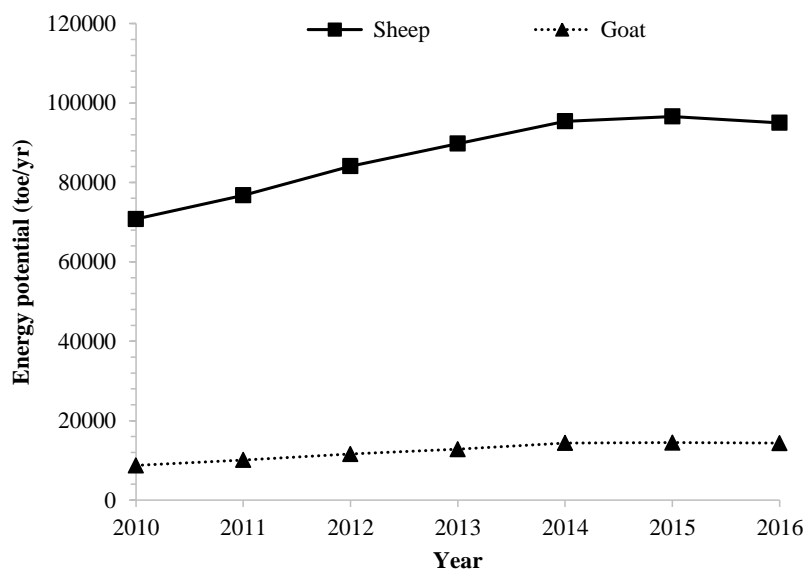


Figure 3. Energy potentials of small ruminants.

Fig. 3 shows that the rate of energy potential for small ruminants has stabilized in recent years. The contribution of sheep on the energy potential is 6.5 times higher than the goat even though the production ratio of sheep is 3 times higher than the goat. It should be noted that sheep production is statistically analyzed as domestic and merino according to the TurkStat data, and the goat species is classified into two groups as ordinary and Angora. While the sheep count for domestic and merino is 93.1% and 6.9%, respectively according to 2016, the goat count for ordinary and Angora is 98% and 2%, respectively. For this reason, the waste production by individual species was considered to be equal each other.

Fig. 4 shows the energy potentials in terms of poultry by years. The curves of broiler hen and laying hen have similar trends and increase almost linearly in recent years. The reason why the energy trends of these species are close to each other is related to the equivalent population to waste ratio. The energy potential of other poultry including turkey, duck and goose is relatively low with respect to the former ones.

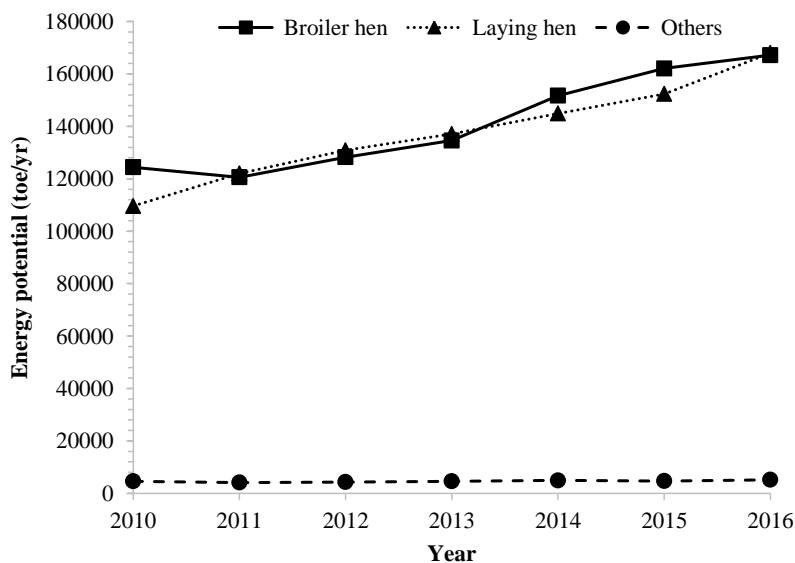


Figure 4. Energy potentials of poultry.

5. Conclusions

This study presents the status of animal biomass in Turkey and its exploitation by use of anaerobic digestion and consequent combustion of methane produced for energy production. Animal biomass resources were examined under three major topics: bovine, small ruminant, and poultry. Bovine animals were described in terms of three different cattle species, buffalo and other species (horse, donkey, camel, mule and pig). Sheep and goat were considered as two subspecies of small ruminant. Poultry consisted of two different chicken species, turkey, goose and duck. Results indicated that 1.36 Mtoe (million tons of oil equivalent) would be exploited by the animal biomass potential of Turkey according to the 2016 data. 67.1%, 8.0% and 24.9% of this potential would be obtained respectively from the biomass of bovine, small ruminant and poultry. Cattle species have the highest contribution to the overall energy exploitation from the animal biomass. The culture cattle have the share of 41% on the overall energy potential among livestock (16 species available) in the countrywide. The waste energy potential of small ruminants has leveled off while the energy exploitation from the bovine and poultry has been increasing in recent years.

6. References

- [1] Demirbas, A. (2009). Biofuels from Agricultural Biomass. *Energy Sources, Part A: Recovery, Utilization, and Environmental Effects*. 31:1573–1582.
- [2] Kumar, A., Kumar, N., Baredar, P., and Ashish, S. (2015). A review on biomass energy resources, potential, conversion and policy in India. *Renewable and Sustainable Energy Reviews*. 45:530–539.
- [3] Halder, P. K., Paul, N., and Beg, M. R. A. (2014). Assessment of biomass energy resources and related technologies practice in Bangladesh. *Renewable and Sustainable Energy Reviews*. 39:444–460.
- [4] Weldemichael, Y., and Assefa, G. (2016). Assessing the energy production and GHG (greenhouse gas) emissions mitigation potential of biomass resources for Alberta. *Journal of Cleaner Production*. 112:425–4264.



- [5] Cutz, L., Haro, P., Santana, D., and Johnsson, F. (2016). Assessment of biomass energy sources and technologies: The case of Central America. *Renewable and Sustainable Energy Reviews*. 58:1411–1431.
- [6] Paiano, A., and Lagioia, G. (2016). Energy potential from residual biomass towards meeting the EU renewable energy and climate targets. The Italian case. *Energy Policy*. 91:161–173.
- [7] Filipović, D., & Krička, T. (2006). An Energy Analysis of Rapeseed Production for Biodiesel in Croatia. *Strojniški vestnik-Journal of Mechanical Engineering*, 52(10), 680.
- [8] Sürmen, Y. (2003). The Necessity of Biomass Energy for the Turkish Economy. *Energy Sources*. 25: 83–92.
- [9] Demirbas, A. (2006). Sustainable Biomass Production. *Energy Sources, Part A: Recovery, Utilization, and Environmental Effects*. 28:955–964.
- [10] Demirbas, A. (2006). Biomass Gasification for Power Generation in Turkey. *Energy Sources, Part A: Recovery, Utilization, and Environmental Effects*. 28:433–445.
- [11] Yelmen, B., and Çakir, M. T. (2016). Biomass potential of Turkey and energy production applications. *Energy Sources, Part B: Economics, Planning, and Policy*. 11:428–435.
- [12] Saracoglu, N. (2010). The Biomass Potential of Turkey for Energy Production: Part I. *Energy Sources, Part B: Economics, Planning, and Policy*. 5:272–278.
- [13] Avcioglu, A. O., and Türker, U. (2012). Status and potential of biogas energy from animal wastes in Turkey. *Renewable and Sustainable Energy Reviews*. 16:1557–1561.
- [14] Balat, M., Acici, N., and Ersoy G. (2006). Trends in the Use of Biomass as an Energy Source. *Energy Sources, Part B: Economics, Planning, and Policy*. 1:367–378.
- [15] Erdogdu, E. (2008). An expose´ of bioenergy and its potential and utilization in Turkey. *Energy Policy*. 36:2182 – 2190.
- [16] Yılmaz, İ. H., Abdulvahitoğlu, A., and Kılıç, M (2017). Evaluation of energy potential for municipal solid waste in Turkey. In: 5th International Conference on Sustainable Solid Waste Management. 21–24 June, Athens, Greece.
- [17] <http://bepa.yegm.gov.tr>
- [18] Saka, K., and Yılmaz, İ. H. (2017). Agricultural biomass potential in Turkey. *International Journal of Management and Applied Science*, 3(2), 79–81.
- [19] <http://www.tuik.gov.tr>
- [20] Yılmaz, İ. H., and Saka, K. (2018). Exploitable biomass status and potential of the Southeastern Anatolia Region, Turkey. *Energy Sources, Part B: Economics, Planning, and Policy*, 13(1), 46–52.



TRIANGLE FUZZY TRANSFORM BASED AUTOMATIC NOISE AND COLOR IMAGE REDUCTION METHODS

Türker TUNCER

*¹ Department of Digital Forensics Engineering, Technology Faculty, Firat University, Elazig, Turkey

* Corresponding author; E-mail: turkertuncer@firat.edu.tr

Received: 4 September 2018; Accepted: 29 December 2018

Noise reduction and image reduction are very important research area for image processing and computer vision. Many papers have been proposed for noise and image reductions. In this paper, novel triangle fuzzy sets transform (F-transform) is proposed for color image denoising and reduction. The proposed methods consist of histogram extraction, threshold points calculation, fuzzy sets construction and fuzzy transformation phases. Firstly, histogram of the image is extracted, maximum points of histogram are calculated, and these points are considered as threshold points. Fuzzy sets are created using threshold points. Then, F-transform is applied on the overlapping and non-overlapping blocks of the images for image denoising and reduction respectively. The main objective of the presented method are to remove random noises of the images and color image reduction with satisfactory visual quality. In order to evaluate triangle fuzzy sets based F-transform applications, variable noise intensities and block sizes are used. Mean absolute error (MAE), peaks signal noise-to-ratio (PSNR) and penalized function (PEN) are utilized for obtaining numerical results. Numerical simulations and comprasions clearly illustare that the proposed triangle F-transform is good transformation for random noises removing and image reduction.

Key words: Triangle fuzzy transform, Image denoising, Image reduction, Image processing.

1. Introduction

In the literature, many transformations for instance Discrete Wavelet Transform (DWT), Discrete Cosine Transform (DCT), Fractional Fourier Transform (FrFT), Fast Fourier Transform (FFT) have been proposed for image reduction, compression, watermarking, recognition and classification [1-4]. Fuzzy transform (F-transform) is one of them and it was presented by Perfilieva in the 2006 [5]. F-transform have been used very large area in the image processing such as image reduction, compression,



noise reduction. Martino et al. proposed a color image reduction method using F-transform [6]. They used cosine fuzzy set to implement fuzzy transformation and they utilized color images as test images. Mean square error (MSE) and penalty function (PEN) were considered as evaluation criteria. Manchanda and Sharma presented a F-transform based image fusion method [7]. The images were divided into $M \times N$ size of non-overlapping blocks and F-transform was applied on each blocks. Then, the F-transform values were fused using weighted method. Chandrasekharan and M presented a F-transform based image enhancement algorithm [8]. In their letter, they used a triangle like fuzzy set and this fuzzy set called as modified triangle fuzzy set. They compared their method to other enhancement methods and this paper proved that the F-transform is successful for contrast enhancement. Manchanda and Sharma suggested a medical image fusion method using F-transform and this F-transform was used cosine fuzzy sets [9]. To evaluate their method, MRI, CT and PET datasets were used. Gregori et al. proposed an image noise reduction method using fuzzy averaging filter with correction step [10]. They used color images for evaluation and peak signal noise-to-ratio (PSNR) was utilized as performance metric. They presented visual and numerical results to show success of the method. Martino et al. presented compressed image segmentation method. The presented compression process was implemented using F-transform and segmentation process used fast generalized fuzzy c-means (FGFCM) [11]. Martino and Sessa proposed a fragile watermarking method for tampered areas localization. This method consisted of image coding using F-transform, watermark insertion, tamper detection and localization phases. This paper illustrated that F-transform is well method for image authentication [12]. Martino and Sessa presented image compression and decompression method using discrete F-transform and they proved that using theorems [13]. Mockor and Hurtik investigated relationships between similarity relations and lattice-valued F-transform [14].

In this paper, a triangle F-transform using triangle fuzzy sets are presented. The triangle fuzzy sets are constructed by using peak points of the histogram. This F-transform is utilized as noise and color image reduction operator in this paper. The main contributions of this paper are given as below.

- In this work, a novel triangle sets based F-transform is presented for noise and image reductions.
- The proposed triangle F-transform used as image compression and noise reduction method. Triangle fuzzy sets are created using histogram of the image. Noise reduction and compression effects were shown in this paper by using two methods with variable parameters. The proposed method was also compared state of art methods. The results proved success of the proposed F-transform.
- A general F-transform algorithms is presented. In this algorithm, overlapping and non-overlapping blocks are used for image and noise reductions respectively.

2. The proposed F-Transform based image noise reduction method

In this method, a novel F-transform is presented and this transform used the classical and the widely used fuzzy set which is called as triangle is used. In this method, 3 triangle fuzzy sets are utilized to calculate transformation. This method consists of histogram extraction, threshold points calculation, fuzzy sets construction, membership degree calculation, fuzzy transformation using these membership degrees and fuzzy image construction phases. The steps of the presented method are given as below.

Step 1: Divide R, G and B channels into cover image.

Step 2: Extract histogram of each channel using Algorithm 1.

Algorithm 1. Pseudo code of the histogram extraction.

<p>Input: Image (I) with size of M x N</p> <p>Output: Histogram of I (histo) with size of 256</p>
<pre> 1: histo=zeros(256); // a vector with size of 1 x 256 and all // of the element are 0. 2: for i=1 to M do 3: for j=1 to N do 4: histo(I(i,j))= histo(I(i,j))+1; 5: endfor 6: endfor </pre>

Step 3: Divide histogram into N parts. $N > 1$. N represents number of the fuzzy sets.

Step 4: Calculate threshold points using Algorithm 2.

Algorithm 2. Pseudo code of the threshold points calculation.

<p>Input: Histogram of the image (histo) with size of 256.</p> <p>Output: Threshold points (thr) with size of N.</p>
<pre> 1: for i=1 to N do 2: counter = ⌊²⁵⁶/_N⌋ 3: [m_i t_i] = max(histo((i - 1) x counter + 1: i x counter)); // Dividing histogram and finding maximum points 4: thr_i = t_i + (i - 1) x counter; // Threshold point calculation. 5: endfor </pre>

Step 5: Calculate membership degrees of the images using threshold points.

$$f(i, j, k) = \begin{cases} \frac{Ch_{i,j}}{thr_k}, Ch_{i,j} \leq thr_k \\ 1 - \left(\frac{Ch_{i,j} - thr_k}{255 - thr_k} \right), Ch_{i,j} > thr_k \end{cases}, i = \{1, 2, \dots, W\}, j = \{1, 2, \dots, H\} \quad (1)$$

Where $Ch_{i,j}$ pixel of the channel, thr_k is threshold point, i and j are indices of the image, W is width of the image (channel), H represents height of the image and k is indice of the threshold points and $k = \{1, 2, \dots, N\}$. Eq. 1 defines triangle fuzzy sets and a sample of it is shown in Fig. 1.

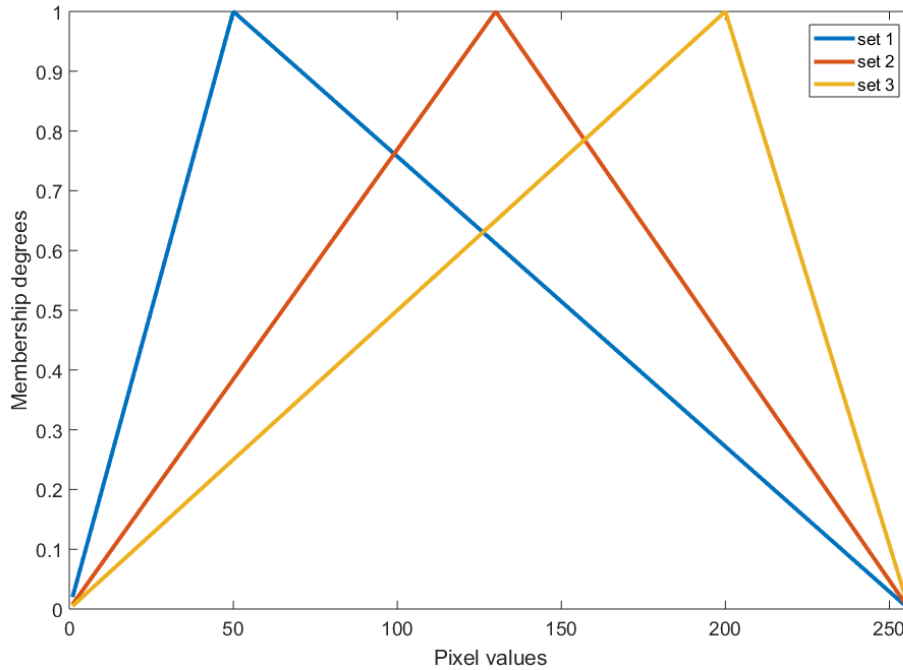


Fig. 1. The 3 triangle fuzzy sets.

Step 6: Divide image into $b \times b$ size of overlapping blocks using noise intensity.

$$b = \begin{cases} 10I - 1, & 10I - 1 \geq 2 \\ 2, & 10I - 1 < 2 \end{cases} \quad (2)$$

Step 7: Apply F-transform to each overlapping block.

$$Ch_{w,h}^F = \frac{\sum_{i=1}^b \sum_{j=1}^b Ch_{i,j} f_{i,j,1} f_{i,j,1} \dots f_{i,j,N}}{\sum_{i=1}^b \sum_{j=1}^b f_{i,j,1} f_{i,j,1} \dots f_{i,j,N}} \quad (3)$$

$$Ch_{w,h}^F = \text{round}(Ch_{w,h}^F) \quad (4)$$

Step 8: Combine the R, G and B channels and reconstruct fuzzy image.

3. The proposed F-Transform based image reduction method

In here, triangle fuzzy transform based color image reduction is presented. This method is similar to Martino et al.'s [6] method. In Ref. [6], cosine based fuzzy sets are used. In this paper, triangle based fuzzy sets are used to reduce color images. The pseudo code of the presented color image reduction algorithm is given below.

Algorithm 3. Triangle F-Transform based color image reduction

Input: Color image (CI) with size of $W \times H$, block size b .

Output: Reduced Image (RI) with size of $W \times H$.

```

1: Extract histogram of the CI.
2: Divide histogram into N pieces.
3: Calculate threshold points using Algorithm 2 and create fuzzy sets.
4: for k=1 to 3 do
5:   for i=1 to N step by b do
6:     for i=1 to N step by b do
7:        $block = CI(i:i + b - 1, j:j + b - 1, k);$ 
8:       Use Eq. 3-4 and calculate F-transform value  $f$ .
9:        $RI(i:i + b - 1, j:j + b - 1, k) = f \times \begin{bmatrix} 1 & \dots & 1 \\ \vdots & \ddots & \vdots \\ 1 & \dots & 1 \end{bmatrix}$ . This equation describes
       expansion.
10:    endfor
11:  endfor
12: endfor

```

4. Experimental Results

In this section, numerical results of the proposed methods are obtained for performance evaluation and PSNR, MAE and Penalty function (PEN) metrics are considered to get numerical results from test images. Mathematical description of the PSNR, MAE and PEN are given Eq. 5-7. Also, 2 triangle fuzzy sets were used to obtain experiments because the best results are achieved using 2 triangle fuzzy sets.

$$PSNR = 10 \log_{10} \frac{255^2 \times 3WH}{\sum_{k=1}^3 \sum_{i=1}^W \sum_{j=1}^H (I_{i,j,k} - RI_{i,j,k})^2} \quad (5)$$

$$MAE = \frac{\sum_{k=1}^3 \sum_{i=1}^W \sum_{j=1}^H |I_{i,j,k} - RI_{i,j,k}|}{3WH} \quad (6)$$

$$PEN = \frac{\sum_{i=1}^W \sum_{j=1}^H \sum_{k=1}^3 |I_{i,j,k} - RI_{i,j,k}|^2}{3WH} \quad (7)$$

where I is original image and RI reduced image for noise or image reduction.

In order to achieve numerical results, a color image test set is used. The test images used are shown in Fig. 2.

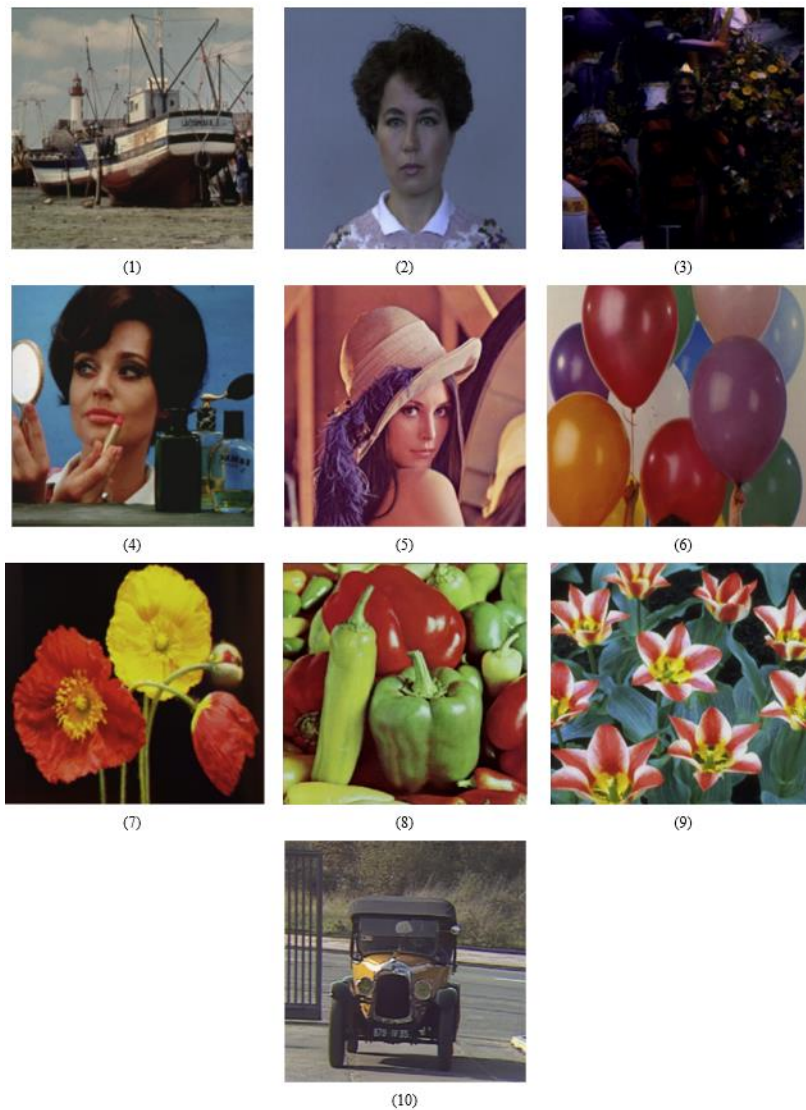


Fig. 2. Colored test images.

1.1. Noise reduction results

Random noises with variable intensities are used to evaluate performance of the proposed triangle based image denoising method. The simulations are implemented on the MATLAB2017a. 10 test images which are shown in Fig. 2 are used to obtain numerical results and they are listed in the Table 1.



Table 1. Statistical results of the proposed noise reduction method with variable noise intensities.

	10%			20%			30%			40%			50%			60%			70%			80%		
	SNR	AE	EN	SNR	AE	EN	SNR	AE	EN	SNR	AE	EN	SNR	AE	EN	SNR	AE	EN	SNR	AE	EN	SNR	AE	EN
	9.49	.66	08.74	8.19	.86	37.05	5.31	.57	40.34	4.77	.24	14.70	2.80	0.76	86.49	1.59	2.71	307.8	0.75	4.28	581.5	0.05	5.68	844.0
	9.40	.31	13.21	8.57	.45	21.90	6.75	.05	89.29	6.63	.75	04.24	5.55	.74	25.47	4.74	.58	31.63	4.13	.30	22.99	3.61	.95	08.38
	0.11	.90	80.71	9.65	.96	90.82	9.13	.09	95.06	7.06	.99	50.96	5.28	.64	34.06	4.10	.04	98.55	3.05	.31	90.31	2.32	0.44	035.0
	9.37	.49	14.35	8.56	.62	27.99	6.21	.18	99.88	5.51	.18	08.45	3.70	.30	75.94	2.46	0.11	024.5	1.46	1.74	264.7	0.73	3.18	501.7
	9.89	.35	85.89	8.62	.54	11.01	5.46	.23	21.80	5.39	.65	14.61	3.39	0.05	29.46	1.94	2.12	154.2	0.94	3.87	446.0	0.12	5.49	725.9
	1.36	.51	33.65	9.79	.68	54.31	6.68	.29	32.69	7.92	.33	85.94	6.17	.77	32.42	4.93	.01	68.88	3.95	.14	16.85	3.03	.30	63.97
	7.60	.93	18.47	7.00	.05	31.46	5.35	.48	99.79	3.41	.94	08.98	1.74	.17	174.7	0.68	0.98	472.2	9.85	2.55	737.2	9.25	3.79	970.9
	7.45	.91	24.57	6.40	.12	59.09	3.99	.86	88.55	2.83	.19	15.384	1.06	2.18	387.3	9.86	4.65	811.3	9.04	6.67	190.3	8.36	8.48	503.9
	7.11	.68	33.68	6.08	.96	75.09	3.63	.78	28.95	1.72	2.64	167.3	9.58	6.91	932.4	8.24	0.44	625.2	7.27	3.43	212.5	6.55	5.97	796.4
0	7.32	.42	47.59	6.67	.59	61.52	4.86	.22	48.07	3.63	.01	99.76	2.07	1.31	157.0	1.14	2.93	436.9	0.49	4.22	663.1	9.97	5.35	864.6

Visual results of samples were shown in Fig. 3 to better understand success of the proposed noise reduction method.

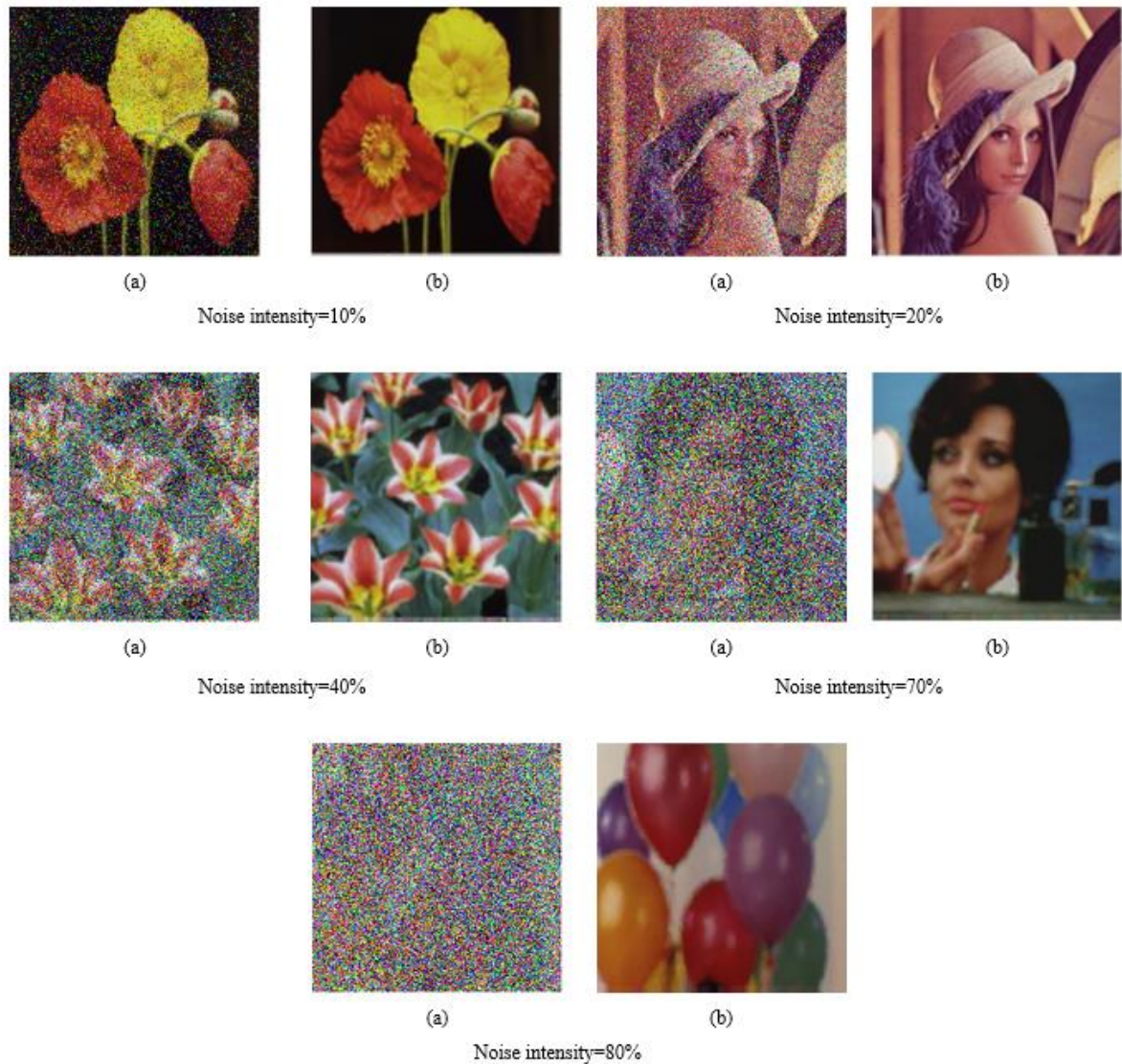


Fig. 3. Visual results aof the some samples (a) noisy image, (b) noise reduced image.

4.2. Image reduction results

2 x 2, 3 x 3, 4 x 4 and 5 x 5 size of non-overlapping blocks are used to evaluate image reduction performance of the proposed triangle based F-transform method. MAE, PSNR and PEN values of the proposed method with these sizes of blocks were listed in Table 2.

Table 2. Results of the proposed image reduction method.

Images	2 x 2			3 x 3			4 x 4			5 x 5		
	PSNR	MAE	PEN	PSNR	MAE	PEN	PSNR	MAE	PEN	PSNR	MAE	PEN
1	26.61	6.94	413.81	24.80	8.58	626.93	22.81	11.07	992.21	22.54	11.58	1502.3



2	34.17	2.24	67.95	31.93	2.86	118.11	30.25	3.57	173.88	29.25	3.94	218.52
3	27.88	4.84	252.35	26.20	6.27	386.07	24.13	8.39	622.16	23.89	8.85	666.49
4	30.20	3.83	151.00	27.78	5.06	263.48	25.71	6.63	426.76	24.96	7.43	509.41
5	27.61	6.04	298.34	26.11	7.07	430.83	24.02	9.29	696.25	23.58	9.74	773.27
6	32.11	3.38	101.03	29.54	4.37	178.65	27.40	5.64	292.28	26.47	6.20	358.57
7	30.34	3.94	140.35	27.49	5.23	265.88	25.56	6.56	410.76	24.44	7.31	524.08
8	23.98	6.39	703.87	23.32	8.21	761.78	21.85	10.41	1161.2	21.31	11.57	1248.7
9	24.74	9.23	621.73	23.83	10.08	796.60	21.65	13.02	1199.7	22.07	12.69	1133.6
10	24.44	8.50	607.42	22.46	11.00	924.29	20.36	14.71	1506.9	19.68	16.24	1726.1

In this section, 2 x 2, 3 x 3, 4 x 4 and 5 x 5 size of blocks are used to image reduction and one pixel is constructed from each block. To compare this method to others, PEN values of methods with 3 x 3 size of blocks are used and comparisons are listed in Table 3.

Table 3. PEN values of the proposed and previously presented methods.

Images	F-Transform	Belikov et al.'s [15] method Algorithm 1	Belikov et al.'s [15] method Algorithm 2	Belikov et al.'s [15] method Algorithm 3	Martino et al.'s [6] method Algorithm 1	The proposed triangle F-transform
1	739.47	703.92	703.51	703.03	654.75	626.93
2	134.49	128.06	127.93	127.78	98.69	118.11
3	432.29	406.82	404.01	401.6	334.43	386.07
4	312.26	299.04	297.66	296.54	253.91	263.48
5	538.45	513.53	512.39	511.12	509.55	430.83
6	201.86	191.65	190.91	190.20	164.20	178.65
7	292.46	278.04	276.68	275.42	272.81	265.88
8	808.90	775.64	774.34	772.98	639.57	761.78
9	1102.79	1048.1	1044.5	1041.3	984.21	796.60
10	1015.14	970.28	968.67	967.22	979.09	924.29
Mean	557.81	531.50	530.06	528.71	482.12	475.26

5. Discussions

Discussions of this study are given as below.

- The proposed noise reduction algorithm is simple as median and mean filters. It achieved very successful results for random noises and Table 1, Fig. 2 proved that this success.
- Results of the proposed image reduction method was listed in the Table 2 and comparisons were given in the Table 3. This method was compared to 3 state of art methods using PEN values and 10 colored test images. The average PEN value of the proposed method was calculated as 475.26. It is the best value among them. Table 3 clearly demonstrated that the proposed method also achieved the best PEN values for 5 test images.

6. Conclusions and recommendations

In this study, a novel triangle based F-transform is proposed and its applications, which are image denoising and reduction, are presented with two novel methods. In the noise reduction method non-overlapping blocks are used. This method uses no correction steps and successful results are achieved using the proposed triangle F-transform based noise reduction method. Random noises were used to implement simulations with 10-80% noise intensities. The proposed denoising method is a basic method and it is better than mean and median filters for random noises. By using non-overlapping blocks, a novel image reduction method is presented and the comparison results have been clearly demonstrated that the proposed image reduction method is a good image decomposition method.

In the future studies, novel applications for instance perceptual hash, image watermarking, etc. methods will be proposed and novel F-transforms will be proposed using other fuzzy sets.

References

- [1] Goel A., Vishwakarma V.P., Fractional DCT and DWT hybridization based efficient feature extraction for gender classification, *Pattern Recognition Letters* 95 (2017) 8–13.
- [2] Zhang Q., Uniqueness guarantees for phase retrieval from discrete windowed fractional Fourier transform, *Optik* 158 (2018) 1491–1498.
- [3] Strain J., Fast Fourier transforms of piecewise polynomials, *Journal of Computational Physics* 373 (2018) 346–369.
- [4] Avcı E., Tuncer T., Ertam F., Çok katmanlı görüntü steganografi, 7. Uluslararası Bilgi Güvenliği ve Kriptoloji Konferansı, 2014.
- [5] Perfilieva I., Fuzzy transforms: Theory and applications, *Fuzzy Sets and Systems* 157 (2006) 993 – 1023.



- [6] Martino F.D., Hurtik P., Perfilieva I, Sessa S., A color image reduction based on fuzzy transforms, *Information Sciences* 266 (2014) 101–111.
- [7] Manchanda M., Sharma R., Multifocus Image Fusion Based on Discrete Fuzzy Transform, IEEE WiSPNET 2017 conference, 2017, 775-779.
- [8] Chandrasekharan R., S. M, Fuzzy Transform for Contrast Enhancement of Nonuniform Illumination Images, *Ieee signal processing letters*, vol. 25, no. 6, june 2018.
- [9] Manchanda M., Sharma R., An improved multimodal medical image fusion algorithm based on fuzzy transform, *Journal of Visual Communication and Image Representation* 51 (2018) 76–94.
- [10] Gregori V., Morillas S., Roig B., Sapena A., Fuzzy averaging filter for impulse noise reduction in colour images with a correction step, *Journal of Visual Communication and Image Representation* 55 (2018) 518–528.
- [11] Martino F.D., Loia V., Sessa S., A segmentation method for images compressed by fuzzy transforms, *Fuzzy Sets and Systems* 161 (2010) 56 – 74.
- [12] Martino F.D., Sessa S., Fragile watermarking tamper detection with images compressed by fuzzy transform, *Information Sciences* 195 (2012) 62–90.
- [13] Martino F.D., Sessa S., Compression and decompression of images with discrete fuzzy transforms, *Information Sciences* 177 (2007) 2349–2362.
- [14] Mockor J., Hurtik P., Lattice-valued F-transforms and similarity relations, *Fuzzy Sets and Systems* 342 (2018) 67–89.
- [15] Beliakov G., Bustince H., D. Paternain, Image reductions using means of discrete product lattices, *IEEE Trans. Image Process.* 21 (3) (2012) 1070–1083.



CLASSIFICATION OF AMYOTROPHIC LATERAL SCLEROSIS AND HEALTHY ELECTROMYOGRAPHY SIGNALS BASED ON TRANSFER LEARNING

*Abdulkadir ŞENGÜR^{*1}, Ümit BUDAK², Yaman AKBULUT³*

^{*1}Electrical and Electronics Engineering Dept., Technology Faculty, Firat University, Elazig, Turkey

²Electrical and Electronics Eng. Dept., Engineering Faculty, Bitlis Eren University, Bitlis, Turkey

³Informatics Dept., Firat University, Elazig, Turkey

*Corresponding author; E-mail: ksengur@gmail.com

Received: 16 December 2018; Accepted: 29 December 2018

This paper investigates the usage of transfer learning in amyotrophic lateral sclerosis (ALS) disease detection. ALS is a dangerous disease which affects the nerve cells in brain and spinal cord. Electromyogram (EMG) is an important measure for analysing of the electrical level of the muscles. EMG based early ALS disease detection system helps the physicians and patients. The proposed work uses EMG signals in discrimination of the ALS and healthy persons. The EMG signals are initially segmented with a overlapped window and each segment is converted to the spectrogram images. The obtained spectrogram images are resized and fed into the pre-trained convolutional neural networks model. The pre-trained model is fine-tuned with the problem at hand. The R002 dataset which is obtained from www.emglab.net is used during the experimental works. Accuracy, sensitivity and specificity measures are used to evaluate the obtained achievement. According to these measures, 97.70% accuracy, 97.97% sensitivity, and 97.29% specificity values are recorded. We further compare the obtained results with some of the existing results that were obtained on the same dataset. The comparisons show that proposed method is outperformed.

Key words: EMG signals, ALS disease, Transfer learning, Convolutional neural networks, Pre-trained models.

1. Introduction

Electromyography is an essential tool for physicians who monitor and evaluate the electrical activity of the muscles [1]. Electromyogram (EMG) is an electrical signal which is useful in various fields such as exercise physiology and medical sciences [2]. EMG signals have been used in detection of the amyotrophic lateral sclerosis (ALS) disease [3]. ALS is a dangerous disease which affects the nerve cells in brain and spinal cord. Thus, the patients can not control his/her muscles and cramping of muscles, nasal speech and difficulty in chewing or swallowing can be seen frequently.

Computer aided diagnosis (CAD) systems help physicians in many fields. EMG based CAD systems are also in demand for detection of various disease such as ALS. Doulah et al. [4] classified EMG signals into normal and ALS classes based on features that were obtained with mel-frequency cepstral coefficient. K-nearest neighbor (K-NN) classifier was adopted in the classification phase of the proposed work. The proposed method achieved 92.50% accuracy. Mishra et al. [5] used empirical mode decomposition (EMD) for classification of the EMG signals. Six different features were considered which were obtained from the EMD of the EMG signals. Least-Square Support Vector Machine (LS-SVM) technique was used in the classification stage of the work. Authors reported 95.00% classification accuracy for their work. Sengur et al. [6] used time-frequency images and convolutional neural networks (CNN) for differentiating of the EMG signals into ALS and normal classes. An end-to-end CNN model was trained with spectrogram images of the randomly sampled EMG signals. The achievement of the proposed method was 96.69%. Fattah et al. [7] used discrete wavelet transform (DWT) for EMG signal analysis. The authors used frame of the EMG signals instead of the whole EMG signal for discriminating of the ALS diseases. Several statistical measures such as maximum and average values on the DWT coefficients were used as features. The k-NN classifier was used for classification and 100% classification accuracy was presented by the authors. Pal et al. [8] used various features such as spectrogram, root-mean-square, entropy, and kurtosis for detection of the ALS from EMG signals. Merlo et al. [9] proposed a fast and reliable method for EMG signal analysis. The authors used wavelet transform for feature extraction. The on and off timing of skeletal muscles at the time of movement was investigated. Sengur et al. [10] proposed time-frequency analysis methods for EMG signal classification. Authors used spectrogram, WT, and Wigner Ville distribution methods. CNN and reinforcement sample learning strategy were then employed to classify these features.

In this paper, a deep learning architecture is used for EMG signal classification. Specifically, the transfer learning (TL) is considered due to its simplicity. TL is the current trend in deep learning, where knowledge of a pre-trained network is shared or transfer to another network [11]. In TL, first, a CNN model is trained by a larger dataset then this pre-trained model is again trained by a smaller dataset to obtain fine tuning for improving the predictive performance of CNN model. The AlexNet model is used as pre-trained CNN model [12]. The color images, that are fed to TL model, are obtained via spectrogram representation of the EMG signals. An overlapping window is used to sample the EMG signals for producing the input images. The input images are then resized to 227×227 . The TL is trained with by using the stochastic gradient descent with momentum. The R002 dataset which is obtained from www.emglab.net [13], is used during the experimental works. Accuracy, sensitivity and specificity measures are used to evaluate the obtained achievement. According to these measures, 97.70% accuracy, 97.97% sensitivity, and 97.29% specificity values are recorded. We further compare the obtained results with some of the existing results that were obtained on the same dataset. The comparisons show that the proposed method is outperformed.

2. Material and Methods

2.1. Convolutional Neural Networks

With the recent developments in deep learning, applications with convolutional neural networks (CNNs) become a shining title for researchers. Generally speaking, CNNs were introduced as a category of feed-forward neural networks [12, 14]. CNNs are compact structures where feature extraction and

classification is handled in one structure. CNNs consist of multiple layers such as convolution, pooling, and fully connected layers. Convolution layer contains a bunch of filters which are convolved across the width and height of the input volume in the forward pass. These filters' coefficients are assigned randomly in the beginning and then filter coefficients are adapted during the training procedure. Pooling layer aims to create a non-linear down-sampling. In other words, pooling partitions the input volume into a set of non-overlapping rectangle sub-regions and for each sub-region, the considered operation is applied for obtaining the output. Fully connected layer is responsible for classification procedure. Neurons in fully connected layer have full connections to all activations in the previous layer.

2.2. Transfer Learning

Using a pre-trained CNN model either for feature extraction or fine-tuning is called transfer learning [15]. Transfer learning uses the knowledge of a pre-trained network, which was trained with millions of labeled images, for a new problem where the number of input image is limited. In the application of the transfer learning, most of the layers of the pre-trained CNN model are saved except the last three layers namely fully connected layer, softmax layer, and classification output layer.

3. Proposed Method

The illustration of the proposed method is given in Fig. 1. As seen in Fig. 1, the input EMG signals are initially sampled with an overlapped window for segmentation of the EMG signals. The overlapped window is used for acquiring more EMG segments. In other words, data augmentation is handled with overlapped windowing procedure.

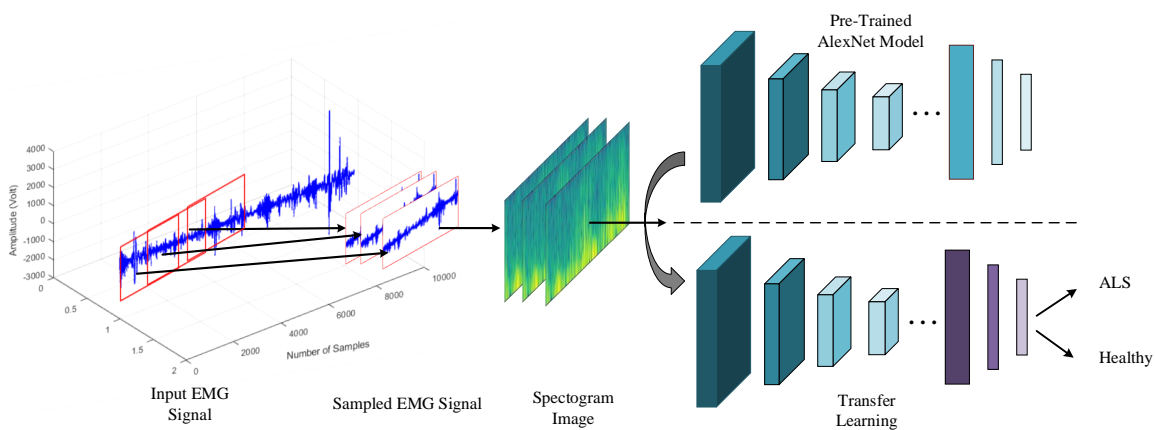


Figure 1. The proposed transfer learning methodology for EMG signal classification

The original EMG signals have around 260,000 samples and the length of the sampling window is chosen as 10,000 samples. The sampled EMG signals are then converted into the color images by applying the time-frequency (T-F) transformation. The short time Fourier transform is considered for T-F image transformation. The constructed T-F images are resized to 227×227 . The AlexNet model is considered as a pre-trained CNN model which was trained on ImageNet challenge [12]. AlexNet is known to be the first deep CNN model that was introduced by Krizhevsky et al. [12]. AlexNet model is totally comprised of 25 layers where 5 of them contain learnable weights and last three layers cover fully connected layers. In AlexNet architecture, rectified linear units, normalization, and max-pooling

layers come after the convolutional layers and convolutional layers use varying kernel sizes. The last three layers of the AlexNet model are discharged because that layers were configured for 1,000 classes ImageNet challenge. These three layers are fine-tuned for the EMG signal classification problem where the number of classes is 2.

4. Experimental Works and Results

The efficiency of the transfer learning is showed on the dataset that was collected by the University of Copenhagen in 2001 [16]. Six males and four females were used for collecting of the healthy EMG signals and four males and four females ALS patients were used for ALS diseased EMG signal collection. The healthy group has an age interval from 21 to 37 years old and ALS group covers the age interval from 35 to 67 years old. A standard needle electrode was used for the signal acquisition. Sampling rate of EMG signals was almost 24 kHz and digitized by A/D convertor of 16-bit resolution. Recorded signals were filtered at 2 Hz and 10 kHz by high- and low-pass filters, respectively.

The dataset contains totally 202 EMG signals of which 89 of them were collected from ALS patients and 133 of them were collected from healthy persons. An overlapping window is used to sample the EMG signals for producing the input spectrogram images as shown in Fig. 1. In spectrogram creation of the EMG signals, we used Hamming window of with 48 ms and overlap 32 ms and the number of the FFT was chosen as 512. The parameters for the spectrogram were determined heuristically during the experimental works. After these sampling procedures, 8,842 spectrogram images were constructed for ALS class and 13,420 spectrogram images were recorded for healthy class. Fig. 2 shows sample spectrogram images from both ALS and healthy classes. While the first row of the Fig. 2 shows the ALS EMG images, the second row shows the healthy EMG images.

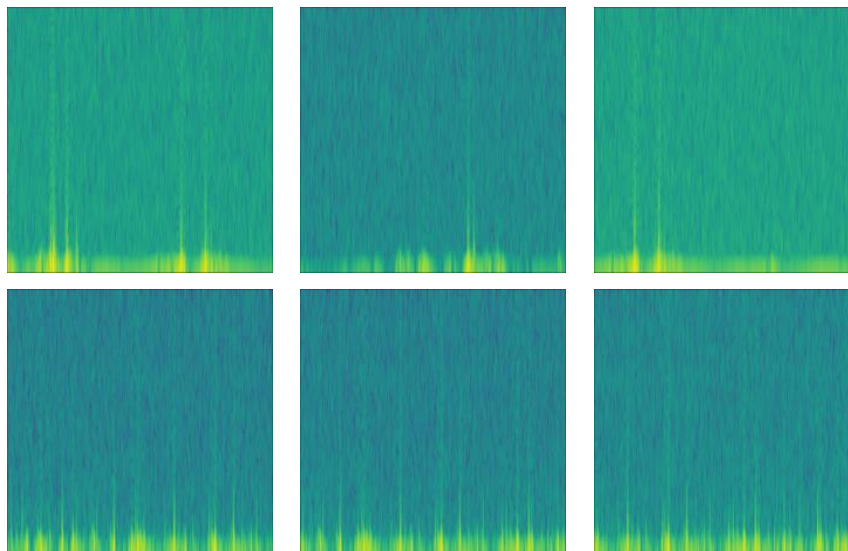


Figure 2. Spectrogram images for the ALS and healthy classes. The first row shows sample images from ALS class and the second row shows sample images from healthy class

For fine-tuning of the CNN model, the mini batch size was chosen as 10 and the initial learning rate was assigned as 0.0001. The initial learning rate was chosen small enough to slow down learning in the transferred layers. The maximum epoch number was set to 7 and the CNN model was trained by

stochastic gradient descent with momentum. The training procedure is ended around 6,000 iterations. Fig. 3 shows the training progress of fine-tuned AlexNet model. While the first row shows the deviation of the accuracy against iterations, the second row shows the loss deviation against iterations. It is worth to mentioning that cross validation test was not applied for transfer learning. The 75% data was used for fine-tuning of the AlexNet model and the rest 25% was used for testing the fine-tuned CNN model.

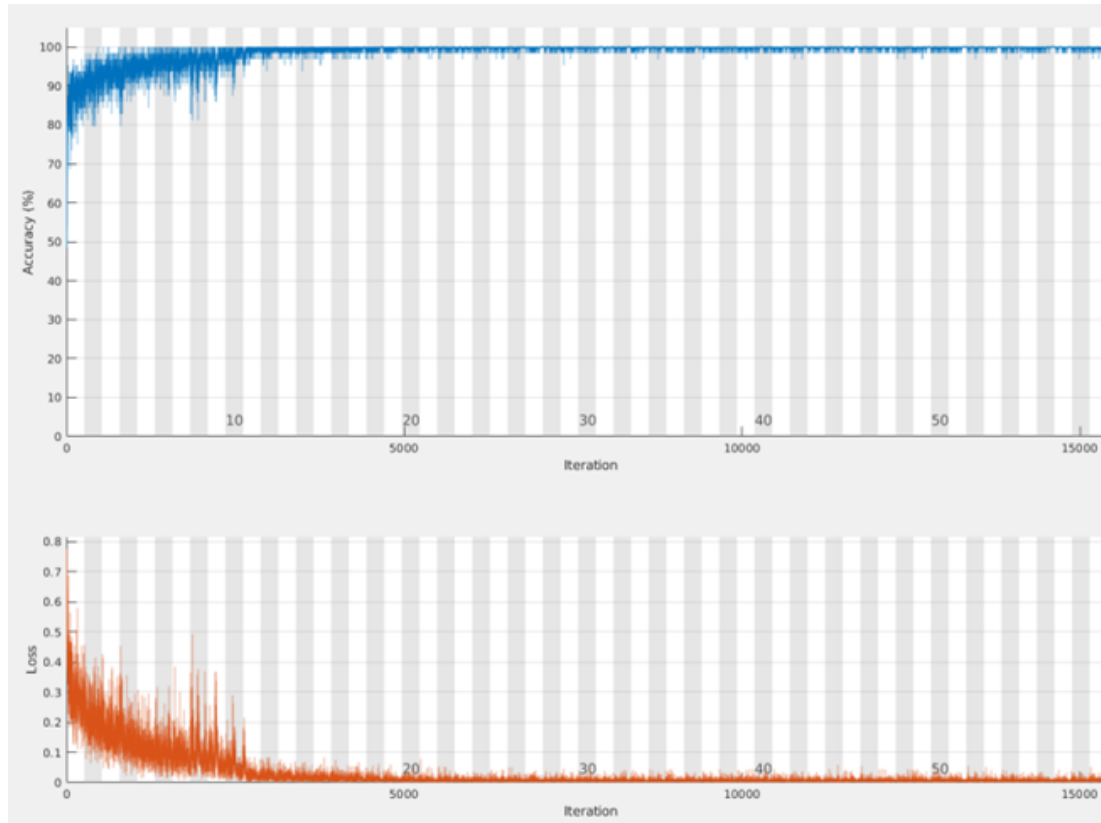


Figure 3. The training progress of fine-tuned AlexNet model

The obtained results were evaluated based on sensitivity, specificity and accuracy criterions respectively as shown in Table 2. In addition, the confusion matrix is given in Table 1.

Table 1. The confusion matrix

	ALS	Healthy
ALS	2158	60
Healthy	68	3287

As seen in Table 2, 97.70% accuracy, 97.29% specificity, and 97.97% sensitivity values were obtained.

Table 2. Performance criteria of proposed method

Method	Sensitivity	Specificity	Accuracy
Transfer learning	97.97%	97.29%	97.70%

Performance comparison of the proposed method with some other methods from literature was given in Table 3. As seen in Table 3, the proposed method outperformed for sensitivity and accuracy evaluation metrics and Sengur et al.'s method produced best specificity value. The proposed method's accuracy was 0.9%, 2.7%, and 5.2% higher than Sengur et al.'s, Mishra et al.'s and Doulah et al.'s methods, respectively.

Table 3. Performance comparison with other methods. The bold case shows the best values

Method	Sensitivity	Specificity	Accuracy
Doulah et al. [4]	76.00%	98.00%	92.50%
Mishra et al. [5]	93.00%	92.50%	95.00%
Sengur et al.[6]	94.80%	98.80%	96.80%
Proposed method	97.97%	97.29%	97.70%

5. Conclusions

In this paper, transfer learning is used to detect ALS disease from EMG signals. EMG signals are segmented with an overlapped window and then transformed into the time–frequency images. The spectrogram images were used as input of CNN. Therefore the input images were scaled with 227×227 dimensions. The pre-trained AlexNet model is used for fine tuning. For fine-tuning of the CNN model, the mini batch size was chosen as 10 and the initial learning rate was assigned as 0.0001. The initial learning rate was chosen small enough to slow down learning in the transferred layers. The maximum epoch number was set to 7 and the CNN model was trained by stochastic gradient descent with momentum. The obtained classification results are evaluated based on some metrics such as accuracy, sensitivity, and specificity. The evaluation metrics show the efficiency of the transfer learning in detection of the ALS disease. We further compare the obtained results with some of the published results. Comparisons show that the proposed method is outperformed. It is worth to mentioning that the fine-tuning procedure is depended on the number of input data. In addition, the training procedure is time-consuming and necessitates strong GPU devices.

References

- [1] Fuglsang- Frederiksen, A., The utility of interference pattern analysis, *Muscle & Nerve: Official Journal of the American Association of Electrodiagnostic Medicine*, 23(1), 2000, pp. 18-36.
- [2] Fukuda, T. Y. *et al.*, Root mean square value of the electromyographic signal in the isometric torque of the quadriceps, hamstrings and brachial biceps muscles in female subjects, *Journal of Applied Research*, 10(1), 2010, pp. 32-39.
- [3] Fattah, S. A. *et al.*, Evaluation of different time and frequency domain features of motor neuron and musculoskeletal diseases, *Int. J. Comput. Appl.*, 43(23), 2012, pp. 34–40.
- [4] Doulah, A. B. M. S. U., Fattah, S. A., Neuromuscular disease classification based on mel frequency cepstrum of motor unit action potential, *In Electrical Engineering and Information & Communication Technology (ICEEICT), 2014 International Conference on IEEE*, pp. 1-4.



- [5] Mishra, V. K. *et al.*, Analysis of ALS and normal EMG signals based on empirical mode decomposition, *IET Science, Measurement & Technology*, 10(8), 2016, pp. 963-971.
- [6] Sengur, A. *et al.*, DeepEMGNet: an application for efficient discrimination of ALS and normal EMG signals, T. Bvrezina, R. Jabłoński (Eds.), *Mechatronics 2017 Recent Technol. Sci. Adv.*, Springer International Publishing, Cham (2018), pp. 619-625, Doi: 10.1007/978-3-319-65960-2_77.
- [7] Fattah, S. A. *et al.*, Identification of motor neuron disease using wavelet domain features extracted from EMG signal, *In Circuits and Systems (ISCAS), International Symposium on IEEE*, 2013, pp. 1308-1311.
- [8] Pal, P. *et al.*, Feature extraction for evaluation of Muscular Atrophy, *In Computational Intelligence and Computing Research (ICCIC), International Conference on IEEE*, December 2010, pp. 1-4.
- [9] Merlo, A. *et al.*, A fast and reliable technique for muscle activity detection from surface EMG signals, *IEEE Transactions on Biomedical Engineering*, 50(3), 20113, pp. 316-323.
- [10] Sengur, A. *et al.*, Classification of amyotrophic lateral sclerosis disease based on convolutional neural network and reinforcement sample learning algorithm, *Health information science and systems*, 5(1), 2017, 9. Doi: 10.1007/s13755-017-0029-6
- [11] Orenstein, E. C., Beijbom, O., Transfer Learning and Deep Feature Extraction for Planktonic Image Data Sets, *In Applications of Computer Vision (WACV), Winter Conference on IEEE*, March 2017, pp. 1082-1088.
- [12] Krizhevsky, A. *et al.*, Imagenet classification with deep convolutional neural networks, *In Advances in neural information processing systems*, 2012, pp. 1097-1105.
- [13] Nikolic, M., Detailed analysis of clinical electromyography signals: EMG decomposition, findings and firing pattern analysis in controls and patients with myopathy and amyotrophic lateral sclerosis, 2001, Doctoral dissertation.
- [14] Simonyan, K., Zisserman, A., Very deep convolutional networks for large-scale image recognition, 2014, *arXiv preprint arXiv:1409.1556*.
- [15] Deniz, E., *et al.*, Transfer learning based histopathologic image classification for breast cancer detection, *Health information science and systems*, 2018, 6(1), 18.
- [16] Detailed analysis of clinical electromyography signals EMG decomposition, findings and firing pattern analysis in controls and patients with myopathy and amy-trophic lateral sclerosis. Ph.D. Thesis, Faculty of Health Science, University of Copenhagen.



RECOGNITION OF IRREGULARLY SHAPED WORDS BY USING FRACTAL DIMENSION

Emre ERKAN^{1}, Muhammet Ali ARSERİM², Mehmet Sıraç ÖZERDEM²*

¹Batman University Vocational School, Batman, Turkey

²Dicle University Engineering Faculty Department of Electric-Electronic Engineering, Diyarbakir, Turkey

* Corresponding author; E-mail: emre.erkana@batman.edu.tr

Received: 14 September 2018; Accepted: 17 November 2018

Abstract— Today, optical character recognition technology is not so advanced as to compete with human perception ability. Parameters such as scene complexity, irregular lighting conditions, skewness, blur and distortion, aspect ratios, perspective impairment, fonts, multilingual environments negatively affect the success of the optical character recognition technology. The aim of this article is to create an algorithm that can resolve irregular words whose characters' scales and rotations are modified. In the algorithm, fractal dimension tool, a fast and stable recognition method, is used. From this viewpoint it is desired to make optical character recognition technology closer to human perception. In order to analyze the algorithm, fractal dimension and image compression data of big, and small alphabetic characters in the tahoma font were recorded in the database. Then, using these characters, irregular word images were obtained. These images, were analyzed by the algorithm built in matlab program and the results were obtained.

Key words: Fractal Dimension, Pattern Recognition, Optical Character

1. Introduction

Optical Character Recognition (OCR) is the process of replacing or converting a document containing text or any text, such as handwriting, printed, or scanned document images, into an editable digital format for deeper and further processing. Today, the recognition of machine characters has largely been solved [1], but OCR technology is not as advanced as to be able to compete with the human perception ability. Effects such as scene complexity, irregular lighting conditions, skewness, blur and distortion, aspect ratios, perspective disturbance, typeface, multilingual environments negatively affect OCR technology's ability [2].

There are many studies on the fractal dimension in the literature, but studies on texts are limited. The foundation is based on fractal dimension; Finding text distortion in the image [3], detection of fonts in Arabic texts [4], detection of which text is written in alphabet [5], text detection and recognition from

mobile video images [6]. However, there is no fractal dimension-based approach that can improve recognition of rotated characters, one of the weaknesses of optical character recognition technology. The aim of this study is to develop an algorithm that can enable the recognition of words that are rotated to their characters. For this purpose, two important applications of the fractal dimension, a powerful and rapid recognition tool; box counting method and image compression are the basis of the designed algorithm [7,8].

2. Phases of the Algorithm

The first phase of the algorithm begins with a character determination process. This determination process is specifically designed for the designed algorithm. The next step is the image compression phase. In this way, images becomes independent from scale and rotation. The third phase is the calculation of the fractal dimension. The final stage is the interpretation of the data and the realization of the character recognition process [7].

Each character is passed through the above mentioned stages in order to analyze the word that forms the image.

This algorithm was developed in the MATLAB program, which was tested for irregular words consisting of large and small alphabetic characters defined in the Tahoma font.

2.1. Determination of Characters

Characterization is specially designed for this algorithm. An example of a Word, formed irregularly is given in Fig.1.

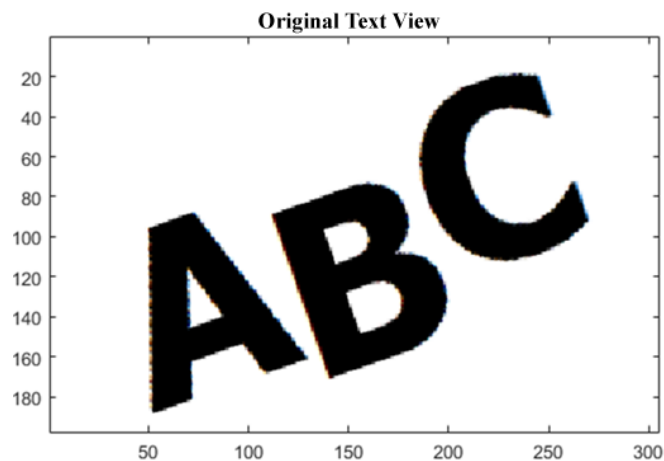


Fig. 1. Irregular vocabulary example

In this example, the image is encoded in binary form. For characterization, the image columns are scanned from top to bottom and from left to right, respectively. The first black pixel detected is used as the starting pixel of the first character boundary to be tested. To obtain the boundaries of the character whose starting point is determined, the boundary pixels of the character in the clockwise direction are found. Thus, the boundary of the character is extracted.

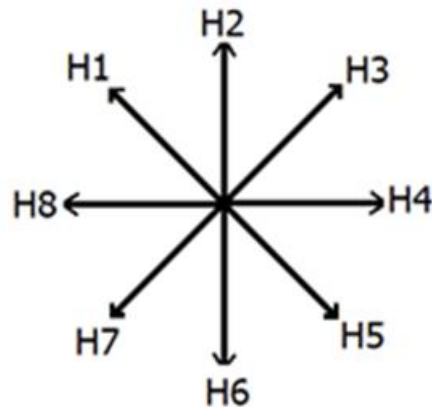


Fig. 2. Directions used when determining the boundary for a character

The directions in Fig. 2 are used when determining the boundaries of the character. Some important situations are need to be known for the boundary detection algorithm. When the starting pixel is detected, the first direction of motion is H6. The determination of the next boundary pixel is depended on the direction of the previous movement.

For example, find the next boundary pixel for the boundary pixel with the final direction of motion H6;

The direction of movement can not be H2, because the aim is to determine the limit of the character in clockwise direction. Since H2 means that the movement is returned to the direction where it comes from. For the clockwise determination of the border, the pixels of the H3-H4-H5-H6-H7-H8-H1 must be tested sequentially. Always if the corresponding pixel is within the boundary of the character, then the direction of the last movement will be through this pixel. For example, when the directions are tested if the pixel in the H5 direction is found to be black, the final direction of motion is determined as H5. This process continues until the starting pixel is the same as the pixel specified after the last transaction. Thus a closed boundary of the character is obtained. Tab. 1. shows the directions in which the pixels should be tested, respectively, according to the direction of the final motion.

Tab.1. Pixel directions to be tested by last motion direction

Last Movement Direction	Pixel Aspects Needed to Test Sequentially
H1	H6-H7-H8-H1-H2-H3-H4
H2	H7-H8-H1-H2-H3-H4-H5
H3	H8-H1-H2-H3-H4-H5-H6
H4	H1-H2-H3-H4-H5-H6-H7
H5	H2-H3-H4-H5-H6-H7-H8
H6	H3-H4-H5-H6-H7-H8-H1
H7	H4-H5-H6-H7-H8-H1-H2
H8	H5-H6-H7-H8-H1-H2-H3

When the algorithm is executed according to the rules in table 1, the boundary in Fig. 3 is obtained.

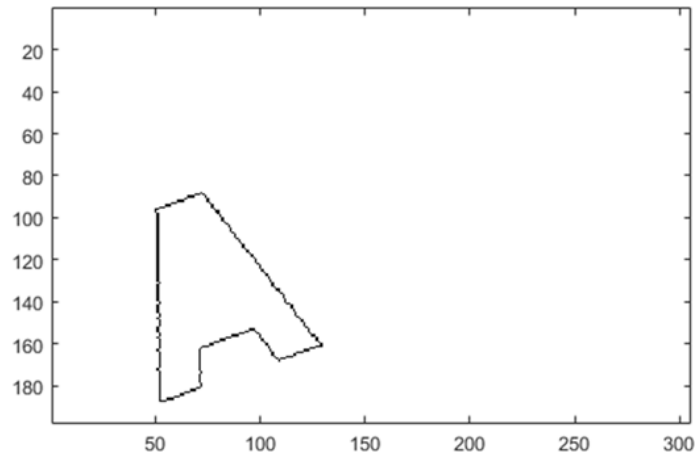


Fig. 3. Determining the boundaries of the first character

The boundary of the first character is shown in the Fig. 3. All the data located in the bounds of the specified character is taken from the original image as in Fig. 4. Thus, the defined character is separated from the original image. For the next character recognition operation, the previously specified character is subtracted from the original image and this is shown in Fig. 5.

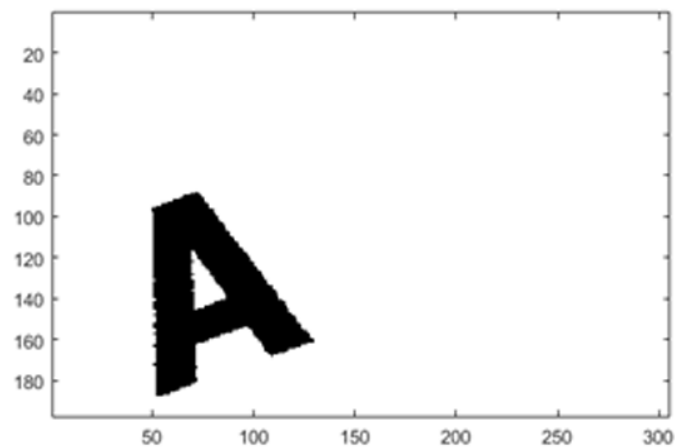


Fig. 4. Retrieving the first character data from the original image

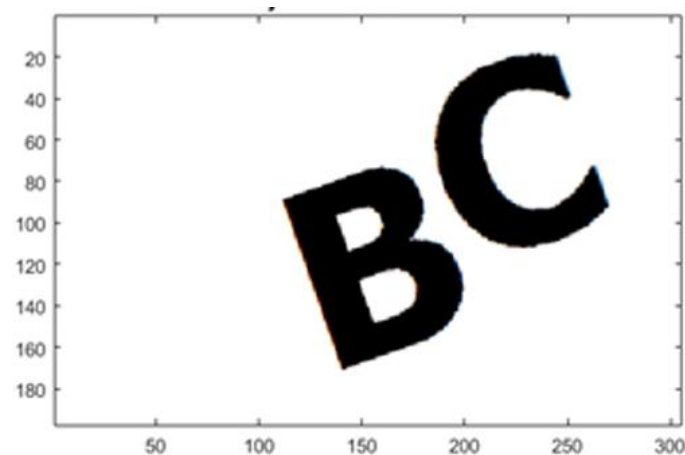


Fig. 5. Previously specified character is removed from the original image for the next step

2.2. Image Compression

It is possible to make the recognition process independent from the scale and the rotation by using picture compression, one of the image processing applications of fractals [9].

In order to make the character independent from the rotation, pre-processing should be done. First, the character specified from the original image is subjected to rotation from 1 to 90 degrees. After each 1 degree rotation, the area associated with the character as in Fig. 6 is calculated as $(x_2 - x_1) * (y_2 - y_1)$ [7].

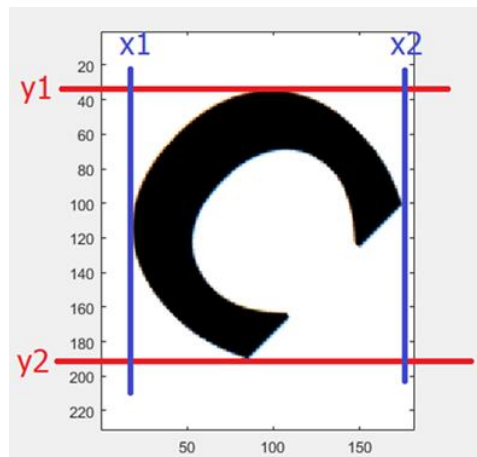


Fig.6. Rotated character

The smallest angle value is obtained as a result of these transformations and the character is rotated by the determined angle value. As a result of this process, 4 different results can be obtained. These results are shown in Fig. 7.

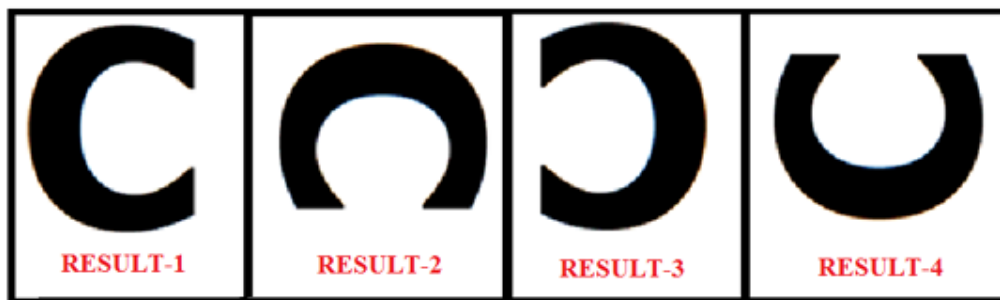


Fig. 7. Cases that may occur after rotation transactions applied to the character

A large number of results means that a large number of transactions are being made in the recognition phase. the number of results can be reduced by half with a simple process; If the character's width is greater than the height, the character is repeated with a rotation of 90 degrees, otherwise it is left in its current position. In this way, the number of results is reduced to two, which is shown in Fig. 8 [7].



Fig. 8. Reduction of results

In the final stage of image compression, the domain of the character is found; the result obtained by applying rotation is placed as in Figure 9, which is equal to the size of a 256x256 Pixel white image, and the width is centered on it. A 256x256-Pixel white image can be larger or smaller. As this field grows, the domain of the character is better calculated. However, the growth of this area means the increase in the transaction load.

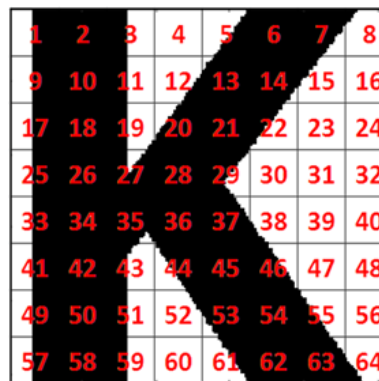


Fig. 9. Finding the character domain

Then the resulted image is divided into equavelent sections consisting of 8x8 64 squares and enumerated as in Fig. 9. Section overlapping with character is assigned "1" whereas "0" is assigned to non-overlapping parts. Thus, the 64 bit character domain data is generated and this data is stored in the database for using in the recognition phase.

2.3. Finding a Fractal Dimension with Box Counting Method

The box counting method can be used not only to find the fractal size of the fractal, but also to detect fractal size of non-fractal objects and characters [10].

The image is usually divided into parcels of 32x32, 16x16, 8x8, 4x4 or 2x2 pixels to find the fractal dimension of an object or a character. The smaller the size of the section, the more accurate the calculated fractal dimension will be [11,12,13].

$$Fractal\ Dimension = \frac{\log(N)}{\log\left(\frac{1}{s}\right)} \quad (1)$$

where N is the number of sections affected by the image, whereas 1/s represents the inverse of the parcel fields.

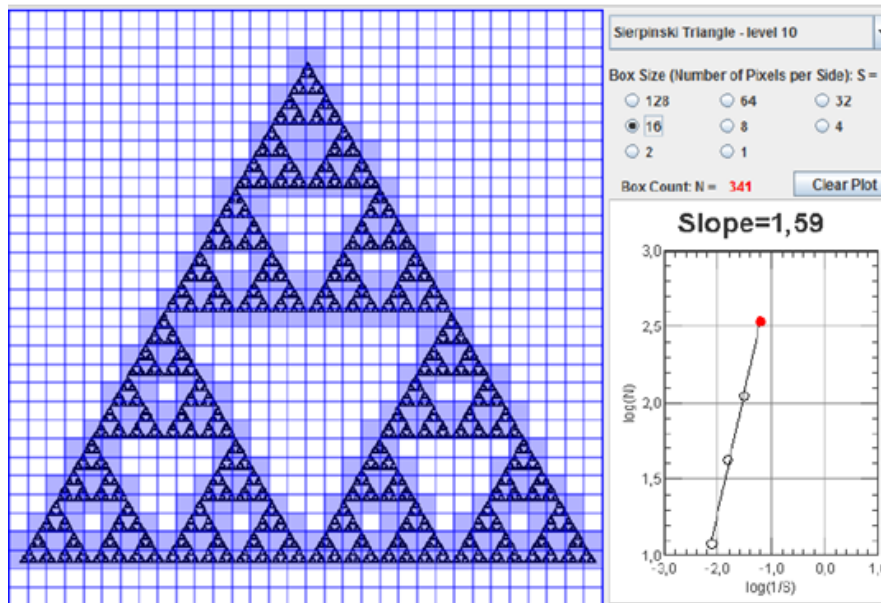


Fig. 10. 16x16 Pixel parcelled image

In Fig. 10 and Fig. 11, the fractal dimension is calculated for different section sizes. the fractal dimension is equal to the slope in the chart as shown in the shapes,. The bigger the slope, the more fractal the object is. The complexity of the image increases as the fractness increases.

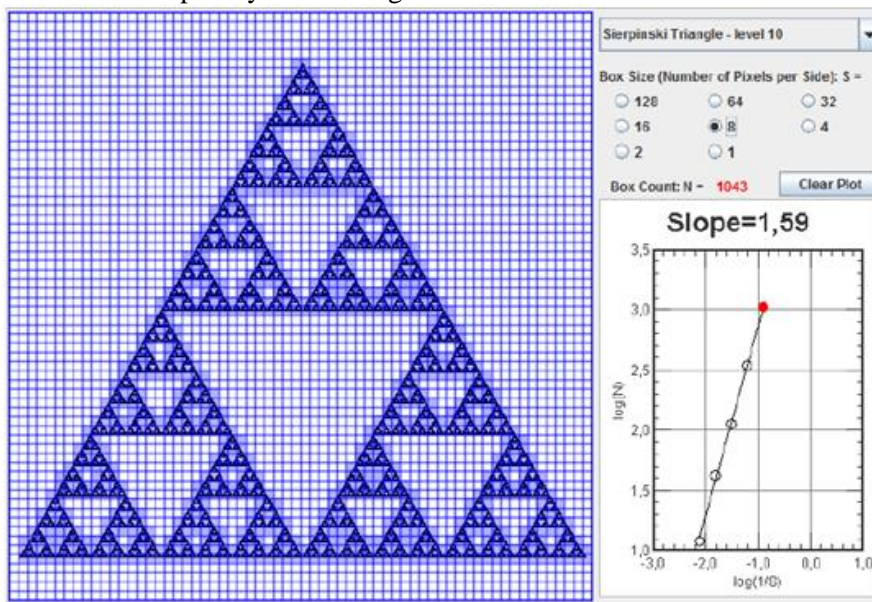


Fig. 11. 8x8 Pixel parcelled image

When it is desired to define a character or object, decision made just by looking at the fractal size or only the domain is not the right approach. For this reason, for more accurate results, the 64-bit domain data and the character's fractal dimension are stored in the database when defining characters.

2.4. Character Recognition

In the first step of the algorithm, the character is determined and the fractal dimension of the detected character is calculated. Then, the characters that have similar fractal dimensions are compared with the

both normal, and 180 degrees rotated domains, shown as in Fig. 12, of the character, found in recognition process.

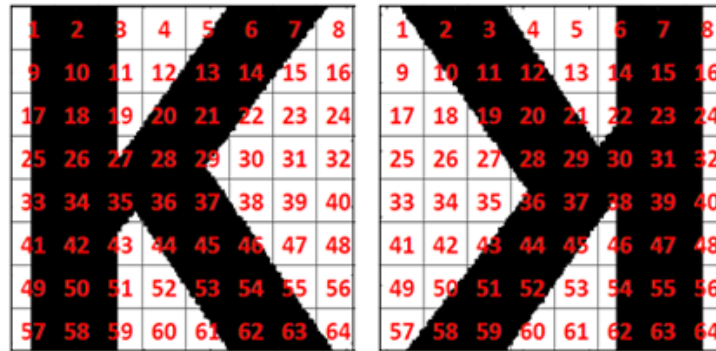


Fig. 12. Domains for the character

As a result of this comparison the character is assigned to the domain of a character with respect to which the character is most similar, with a condition that it does not exceed a specific error margin. The same actions are repeated for all characters that make up the image. By combining the characters that are resolved sequentially, the irregular word is solved.

3. Conclusions

In order to test the algorithm, sample irregular words were used in Tahoma font. The generated images can be seen in Fig. 13, 14, 15, 16. The characters that make up the words in different scales, different rotations, case sensitive, various locations were tested. No interference was performed to eliminate noise in the algorithm and noise-free images were used for the test.

As a result of the tests, it is observed that this algorithm based on fractal size has achieved successful results. Thanks to this algorithm, optical character recognition technology can be made more stable against character rotation. Thus, optical character recognition technology is projected to be one step closer to human perception.

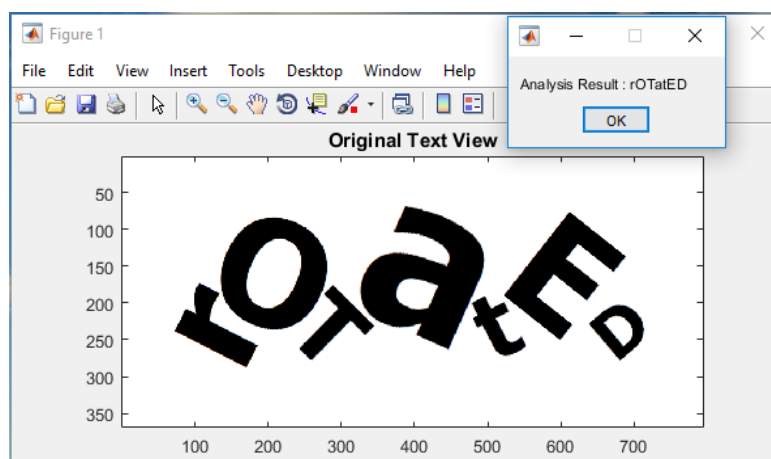


Fig. 13. Resolving of the irregular 'rOTatED' word

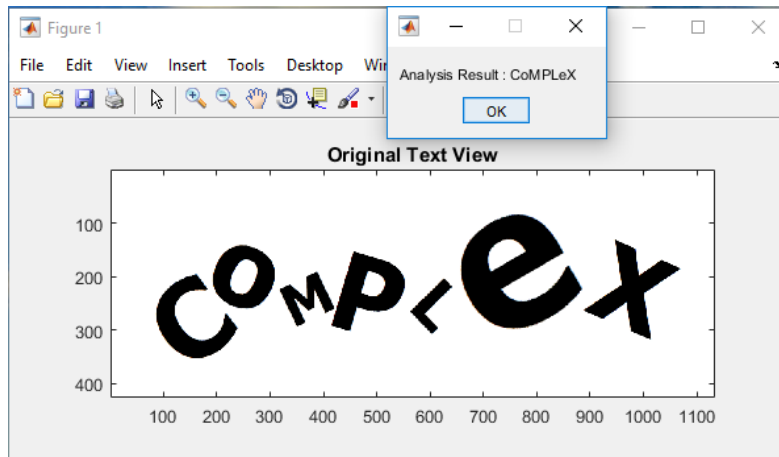


Fig. 14. Resolving of the irregular 'CoMPLeX' word

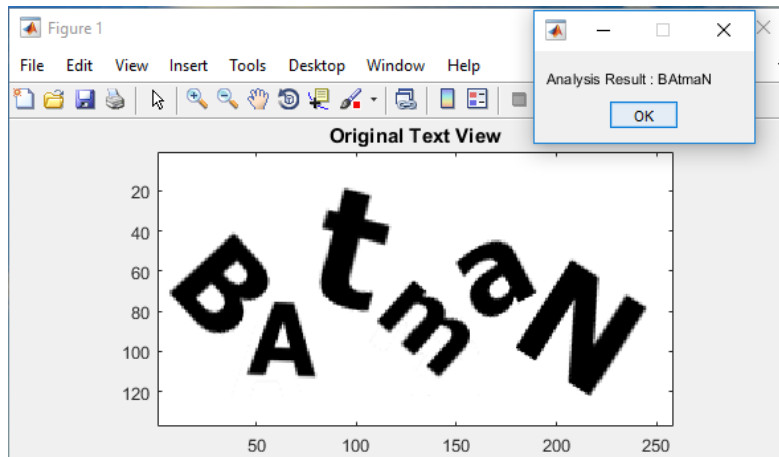


Fig. 15. Resolving of the irregular 'BATmaN' word

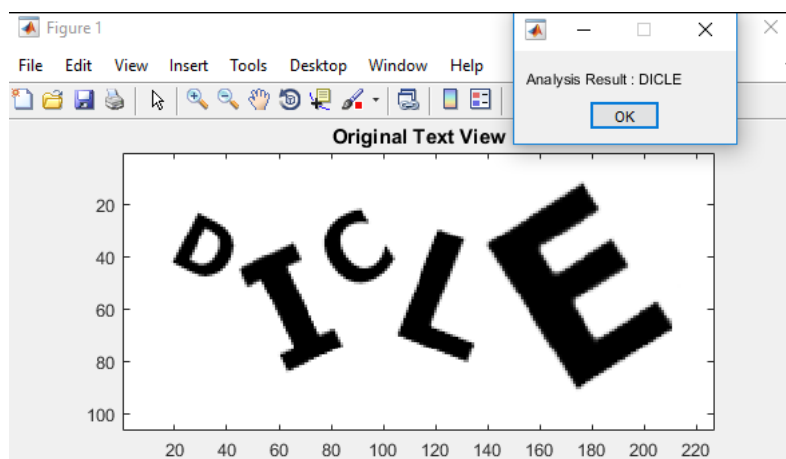


Fig. 16. Resolving of the irregular 'DICLE' word



References

- [1] Hamad K.A., Kaya M., A Detailed Analysis of Optical Character Recognition Technology, *International Journal of Applied Mathematics, Electronics and Computers*, 4 (Special Issue) (2016), pp.244-249, ISSN: 2147-82282147.
- [2] Vamvakas G., Gatos B., Perantonis S.J., Handwritten Character Recognition through Two-Stage Foreground Sub-Sampling, *Pattern Recognition*, 8 (2010), pp.2807-2816, DOI No: 10.1016/j.patcog.2010.02.018.
- [3] Yu C.L., Tang Y.Y., Suen C.Y., Document Skew Detection Based on the Fractal and Least Squares Method, *Proceedings of 3rd International Conference on Document Analysis and Recognition*, Montreal, Quebec, Canada, 1995, Vol. 1, pp. 1149-1152.
- [4] Moussa S.B., Zahour A., Benabdelhafid A., Alimi A.M., New Features Using Fractal Multi-Dimensions for Generalized Arabic Font Recognition, *Pattern Recognition Letters*, 5 (2010), pp.361-371, DOI No: 10.1016/j.patrec.2009.10.015.
- [5] Moussa S.B., Zahour A., Benabdelhafid A., Alimi A.M., Fractal-Based System for Arabic/Latin, Printed/Handwritten Script Identification, *2008 19th International Conference on Pattern Recognition*, Tampa, FL, USA, 2008, Vol. 1, pp. 978-981, DOI No: 10.1109/ICPR.2008.4761838.
- [6] Shivakumara P., Wu L., Lu T., Tan C.L., Blumenstein M., Anami B.S., Fractals Based Multi-Oriented Text Detection System for Recognition in Mobile Video Images, *Pattern Recognition*, 68 (2017), pp.158-174, DOI No: 10.1016/j.patcog.2017.03.018.
- [7] G. Neil, K. M. Curtis, Shape Recognition Using Fractal Geometry, *Pattern Recognition*, Vol. 30, No. 12 (1997), pp. 1957-1969.
- [8] Les T., Kruk M., Osowski S., Objects Classification Using Fractal Dimension And Shape Based On Leaves Classification, *ResearchGate*, June 2013.
- [9] D. C. Popescu and H. Yan, Fractal-Based Method for Colour Image Compression, *J. Electronic Imaging*, Vol.4(1) (1995), pp.23-30.
- [10] Fractal Dimension- Chapter 2, <http://fractalfoundation.org/OFC/OFC-10-1.html> [Access February 7, 2018].
- [11] M. Sonaka, V. Hlavac and R. Boyle, *Image Processing, Analysis and Machine Vision*, Chapman and Hall Computing, London, 1993.
- [12] M. Cusenza, *Fractal Analysis of the EEG and Clinical Applications*, Università Degli Studi Di Trieste, Trieste, Italy, 2012.
- [13] Buczkowski S., Kyriacos S., Nekka F., Cartilier L., The Modified Box-Counting Method: Analysis of Some Characteristic Parameters, *Pattern Recognition*, 4 (1998), pp.411-418, DOI No: 10.1016/S0031-3203(97)00054-X



NEW SWARM INTELLIGENCE BASED OPTIMIZATION ALGORITHMS FOR THE OPTIMIZATION OF MICROGRIDS

Tuba TANYILDIZI AĞIR^{*1}, *Zafer AYDOĞMUS*², *Bilal ALATAS*³

^{*1}Lecturer, University of Batman, Vocational High School Electronic Communication Technology Program

²Prof. Dr., University of Firat, Technology Faculty, Department of Electrical-Electronics Engineering

³Assoc. Prof. Dr., University of Firat, Engineering Faculty, Department of Software Engineering

* Corresponding author; E-mail: tanyildizituba@gmail.com

Received: 26 September 2018; Accepted: 22 November 2018

The need for new energy sources has increased due to reasons such as the development of technology, the increase in electricity demand, the decrease of fossil resources, and environmental pollution. Renewable energy sources are self-renewing, friendly, and clean energy sources. Microgrids are small power energy networks consisting of renewable and non-renewable energy sources, batteries, inverters, and loads. They can be operated connected to the network and independently from the network. Metaheuristic methods are algorithms that can achieve optimum results in the search space. In this study, optimization of a microgrid composed of a wind turbine, solar panel, diesel generator, inverter, and loads has been investigated with multi-objective hybrid metaheuristic algorithms. Optimization is aimed at reducing emissions, increasing reliability, and optimizing energy resources. Swallow Swarm Optimization (SSO) and Hybrid Particle Swallow Swarm Optimization (HPSSO) with different iterations and populations are compared for the first time.

Key words: *Microgrid, Metaheuristic algorithms, SSO, HPSSO.*

1. Introduction

Scientists have been in search of different power networks due to increasing social demands and insufficient existing power networks, and in order to improve reliability and quality [1]. For these reasons, significant changes have occurred in the electrical systems of developed countries. These changes have increased the use of renewable energy sources. However, in recent years, importance has been given to the use of renewable energy to ensure a broad liberalization of the electricity market and to preserve the quality of energy supplied to consumers [2].

Distributed production units have arisen due to environmental problems, market regulation, incentive policies, and the increase in global electricity demand. Distributed production units have many advantages such as increasing reliability, reducing power losses, improving power quality, and integration of renewable energy sources. However, these production units also have negative effects such as network security, system voltage, power system control, and power balance [3].

Renewable energy sources are often used as an alternative energy source in modern power systems. [4]. These energy sources are solar, wind, geothermal, biomass, and tidal. Many countries aimed at exceeding 20% of the power consumption used by renewable energy sources by 2020 [5]. As these energy sources have many advantages, these resources have some disadvantages such as proper working with other

production units. Some of the disadvantages caused by these sources are system voltage and frequency regulation, maintenance, and protection of renewable energy sources, network-dependent and grid-independent mode control arrangement [4].

Microgrid consists of distributed energy sources, storage units, inverter, and loads. These networks significantly increase the reliability of power systems in case of a power cut or if part of the network requires electricity. A well-designed distribution system can deal with load and systemic failures [6]. A microgrid can operate as connected to the network or independent of the network. Each distribution unit is connected to the microgrid via an interface inverter. The primary responsibility of the interface inverter is to regulate the frequency and amplitude of the output voltage, and thus to provide active and reactive power sharing. However, it can be used to improve the power quality of these inverters by selecting an appropriate control scheme [7]. A general power system uses battery energy storage units to avoid power outages and power fluctuations caused by environmental factors. Renewable energy is converted to DC and stored with energy storage elements and then converted to AC. This approach can easily adapt to existing electrical installations and accelerate the use of renewable energy [5].

Most engineering optimization problems are often difficult to solve, and many methods try to solve these complex problems. In these problems, the search space depends on the problem size. For this reason, traditional optimization methods do not provide a suitable solution for complex non-linear problems. For this reason, many metaheuristic algorithms are designed to solve such type of problems. Researchers have used metaheuristic algorithms to come up with complex problems such as timing problems, data clustering, image and video processing, and constructing neural networks [8]. The metaheuristic algorithms are global optimization methods that mimic natural phenomena and social behaviors. For example, biological evolution, thermal annealing, animal behavior, improvised music, swarming behavior, and so on. Two important features of these optimization methods are diversification and intensification. Diversification allows the optimizer to discover the search space more efficiently [9]. Intensification serves to explore the best available solutions and to select the best candidate designs. Specific objectives of the development of modern metaheuristic algorithms are to solve problems faster, to solve complex problems and to obtain more robust methods. Nevertheless, nature is a major source of inspiration to propose new metaheuristic approaches [10].

2. Swallow Swarm Optimization

There are three types of particles in this algorithm. The explorer particle, the aimless particle, and the leading particle. These particles move parallel to each other and are always in interaction. Every particle in the colony is responsible for directing the colony to a better state. Fig. 1 shows the particle types.

- **Explorer particle:**

The most important part of the colony is the explorer particles. Their primary responsibility is to make an exploration of space. The swallow emits a different tone of voice when the extract reaches the point of the candle and plays a role as chief leader [11].

- **Aimless particles:**

These particles are the worst particles when compared to other particles in the colony. The responsibilities of them in the group are randomly researching and exploration of the problem space. However, they have not any information about the position of the head leader and the local leader [12]. The equation of the update step for the aimless particle is shown in Eq. 1. In this equation, O_i^k represents the aimless particle, $rand$ is a random number between 0 and 1; min_s is the lower limit of variables, and max_s is the upper limit of the variables.

$$O_i^{k+1} = O_i^k + [rand(-1,1) * \frac{rand(min_s,max_s)}{1+rand()}] \quad (1)$$

- **Leading particles:**

These particles are called leaders in the SSO algorithm. Their location and quantities may vary at each level. These particles can be distributed or collected in the search space. The local leader is defined as the best leader of the sub-colonies. In the swallow, thousands of members colony are divided into a series of sub-colonies. These sub-colonies have a leader. This leader can be changed repeatedly by wiser and more powerful swallows. Lead swallow is the closest to food and resting places. The task of this leader is to guide other colony members [13]. The position update step of a principal leader is shown in equation Eq. 2. The acceleration coefficient update step equation is expressed in Eq. 3 and Eq. 4. Position update step equation and explorer particle update step equation are shown in Eq. 5 and Eq. 6 respectively. In these equations, VHL_i is velocity vector of head leader, α_{HL} is acceleration coefficient, e_{best} is the best value of the particle, e_i is the explorer particle, β_{HL} is used for acceleration coefficient, HL_i is a head leader, and VLL_i is local leader.

$$VHL_{i+1} = VHL_i + \alpha_{HL}rand()(e_{best} - e_i) + \beta_{HL}rand()(HL_i - e_i) \quad (2)$$

$$\left\{ \begin{array}{l} \alpha_{HL} = if(e_i = 0 || e_{best} = 0) \rightarrow 1.5 \\ \alpha_{HL} = if(e_i < e_{best}) \&\& ((e_i) < HL_i) \rightarrow \frac{rand()e_i}{e_i \times e_{best}} \quad e_i, e_{best} \neq 0 \\ \alpha_{HL} = if(e_i < e_{best}) \&\& ((e_i) > HL_i) \rightarrow \frac{2 \times rand()e_{best}}{1/(2 \times e_i)} \quad e_i \neq 0 \\ \alpha_{HL} = if(e_i > e_{best}) \rightarrow \frac{e_{best}}{1/(2 \times rand())} \end{array} \right. \quad (3)$$

$$\left\{ \begin{array}{l} \beta_{HL} = \{if(e_i = 0 || e_{best} = 0) \rightarrow 1.5 \\ \beta_{HL} = if(e_i < e_{best}) \&\& (e_i < HL_i) \rightarrow \frac{rand()e_i}{e_i \times HL_i} \quad e_i, HL_i \neq 0 \\ \beta_{HL} = if(e_i < e_{best}) \&\& (e_i > HL_i) \rightarrow \frac{2 \times rand()HL_i}{1/(2 \times e_i)} \quad e_i \neq 0 \\ \beta_{HL} = if(e_i > e_{best}) \rightarrow \frac{HL_i}{1/(2 \times rand())} \end{array} \right. \quad (4)$$

$$V_{i+1} = V_{HL_{i+1}} + V_{LL_{i+1}} \quad (5)$$

$$e_{i+1} = e_i + V_{i+1} \quad (6)$$

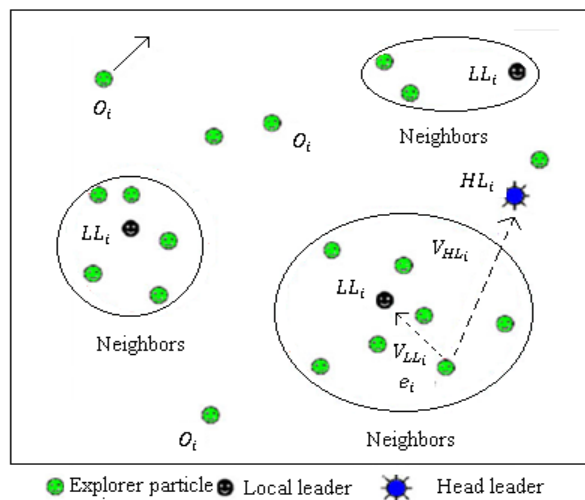


Figure 1. Types of particles [13]

3. Hybrid Particle Swallow Swarm Optimization (HPSSO)

HPSSO contains two key features of the SSO added to the basic PSO equation when specific sub-colonies and particles for specific tasks are considered. Similar to SSO, there are leaders (head leader, local leader), explorers and aimless particles. The size of the population is determined by the aimless particles and sub-colonies. The HPSSO starts with a random speed set and a random set of particles in the search area. The position and speed of each particle are constantly updated to search for the optimal solution. The best particle is identified as the head leader. The next particles are set from top to bottom in the position of local leaders. Aimless particles are selected from the worst individuals from top to bottom. The remaining particles are set as explorers. Each explorer particle occurs when the updated velocity vector is added to the current position of this particle. Compared to the PSO, it contains an additional term to describe the contribution of local leaders [14]. The position update step equation is shown as Eq. 7, and speed update step equation is shown as Eq. 8.

$$X_i^{k+1} = X_i^k + V_i^{k+1} \quad (7)$$

$$V_i^{k+1} = \omega V_i^k + c_1 r_1 (P_i^k - X_i^k) + c_2 r_2 (P_g^k - X_i^k) + c_3 r_3 (P_{l(i)}^k - X_i^k) \quad (8)$$

$P_{l(i)}^k$ is the local leader of the lower colony of the i th particle, r_3 is a random number in the range (0,1). c_3 is the learning factor that controls proximity perception and ω is the inertia weight that controls the effect of the previous velocity.

In each iteration, the position of a particle within a sub-colony can be changed to move away from the current local leader and join another group. The distance between each explorer particle and a local leader is used to determine the sub-colony of each explorer particle in the group of the nearest local leader [15]. Distance update is shown in Eq. 9 and Eq. 10.

$$dist_{i,j} = |X_i - P_{i,j}|, j = 1, 2, \dots, N_{sub-colony} \quad (9)$$

$$dist_{i,j} = \sqrt{(X_i^1 - P_{i,j}^1)^2 + (X_i^2 - P_{i,j}^2)^2 + \dots + (X_i^{n_g} - P_{i,j}^{n_g})^2} \quad (10)$$

n_g is the number of design variables. $dist_{i,j}$ is the distance between the explorer particle i and the local leader j . Three possible options are taken for aimless particles.

- As in SSO, they only make a random search.
- They perform a local search in the area of the local leader.
- They dynamically search within the region where the global leader is located.

If option two is chosen, the number of aimless particles coincides with the number of sub-colonies, and aimless particles may not identify each sub-colony. In this case, the distance between the worst particle and the local leaders is the criterion for the assignment of the aimless particle.

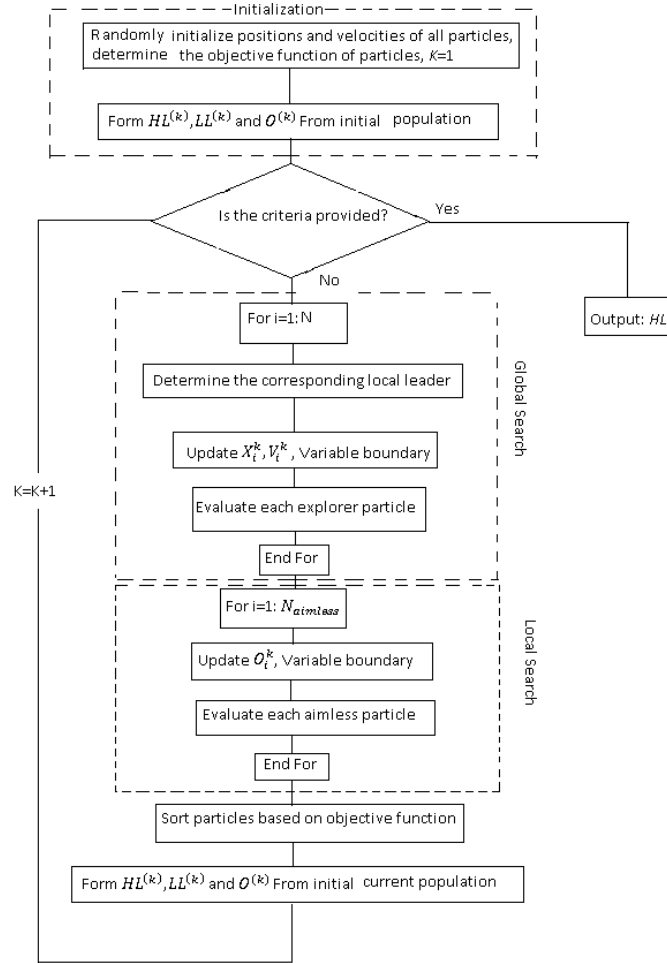


Figure 2. Flowchart of the HPSSO algorithm [14]

4. Simulation Results

4.1. Fitness Function

The fitness function provides the most appropriate solution for multi-objective optimization. The fitness function is given in Eq. 11. In this equation, P_L represents the sizing of distributed energy sources, LPSP is power supply loss, and RF is an environmental factor. The upper and lower limit of the problem are given in Eq. 12.

$$A = \frac{1}{(0.6*LPSP)+(0.2*RF)+(0.2*P_L)} \quad (11)$$

$$\begin{cases} 0 < P_{solar\ power\ plant} \leq 8000 \\ 0 < P_{wind\ turbine} \leq 4500 \\ 0 < P_{diesel\ generator} \leq 1500 \end{cases} \quad (12)$$

4.2. Comparison of SSO and HPSSO in terms of iteration

SSO and HPSSO algorithms were executed with different number of iterations as 100, 250, and 400 in three different cases. Each algorithm was executed 30 times and the mean values were taken. The fitness value graph for SSO algorithm with 100 iterations has been demonstrated in Fig. 2. The power values of the microgrid, renewable and non-renewable energy sources, the battery and the residual load to be supplied

are shown in Table 1. These initial values are values that algorithms do not optimize. The algorithm parameter is $n_{population}=100$.

Table 1. The initial power values

Problem parameters	Values
$P_{residence\ load}$	1000 kW
$P_{battery}$	4000 kW
$P_{battery\ load}$	3600 kW
$P_{solar\ power\ plant}$	8000 kW
$P_{wind\ turbine}$	4500 kW
$P_{diesel\ generator}$	1500 kW

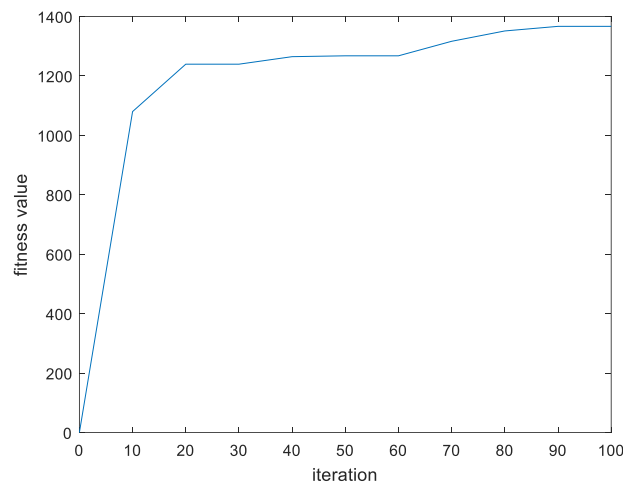


Figure 3. The fitness values obtained from the SSO algorithm in case of maximum 100 iterations

When the SSO algorithm is executed with 100 iterations, the obtained optimized power values for the solar power plant, the wind turbine, and the diesel generator are 4708.24 kW, 2355.65 kW, and 3076.029 kW respectively.

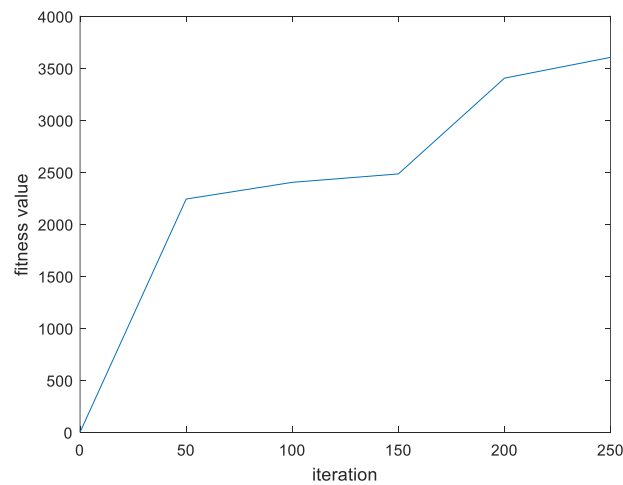


Figure 4. The fitness value graph for the SSO algorithm when the maximum number of iterations equals to 250

The obtained power values for the solar power plant, the wind turbine, and the diesel generator are 4625.96 kW, 2587.776 kW, and 3162.65 kW respectively after 250 iterations of SSO. In Fig. 3, the fitness values versus iteration numbers are shown.

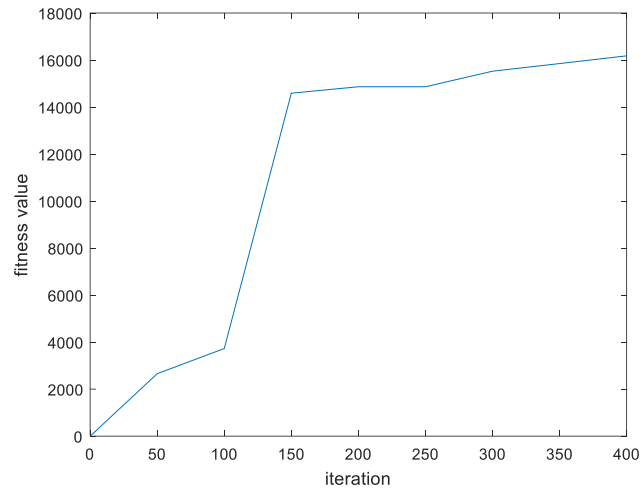


Figure 5. The fitness value for $n_{iteration} = 400$ in the SSO algorithm

When the SSO algorithm is executed with $n_{iteration} = 400$; the power values of the solar power plant, the wind turbine, and the diesel generator are 4988.17 kW, 2807.22 kW, 2692.87 kW. In Fig. 4, the fitness value versus the number of iterations is shown for $n_{iteration} = 400$.

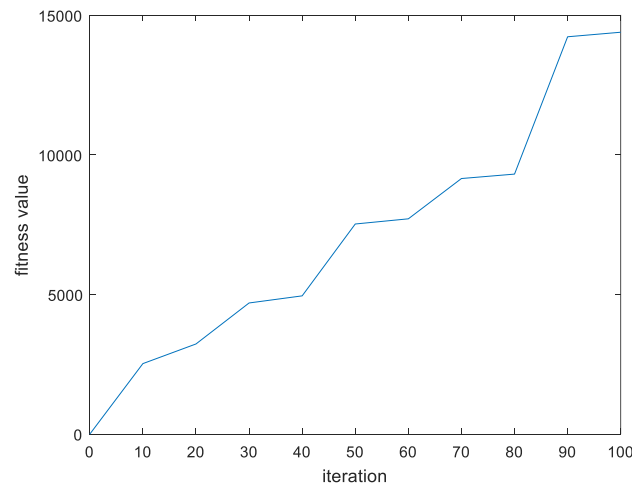


Figure 6. The fitness value for $n_{iteration} = 100$ in the HPSSO algorithm

The obtained optimized power values for the solar power plant, the wind turbine, and the diesel generator are 3594 kW, 2294.029 kW, and 3826.79 kW after 100 iterations of HPSSO. In Fig. 5, the fitness value and the number of iterations is shown for $n_{iteration} = 100$.

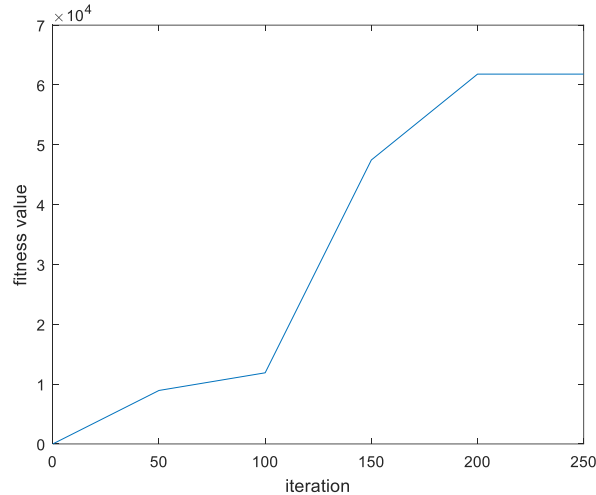


Figure 7. The fitness value graph for the HPSSO algorithm when the maximum number of iterations equal to 250

When the HPSSO algorithm is run with $n_{iteration} = 250$, the optimized power values for the solar power plant is the wind turbine is and the diesel generator is 3776.21 kW, 2462.21 kW, and 3675.81 kW respectively. In Fig. 6, the fitness value versus the number of iterations is demonstrated for the HPSSO algorithm.

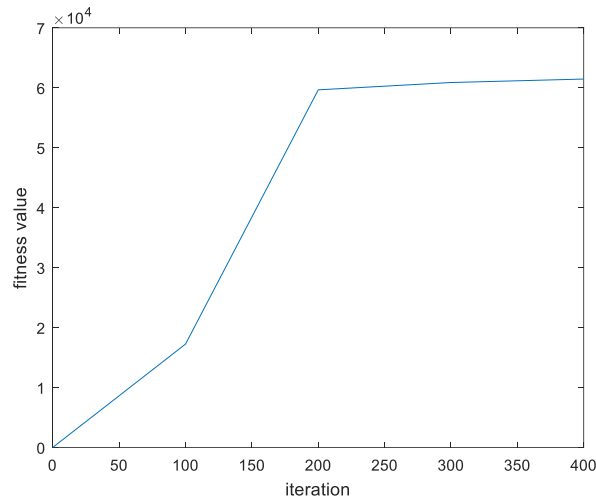


Figure 8. The fitness value for $n_{iteration} = 400$ in the HPSSO algorithm

The values of 3219.8 kW, 2173.37 kW, and 4253.42 kW have been obtained from the optimized power values for the solar power plant, the wind turbine, and the diesel generator respectively when the HPSSO algorithm is executed with 400 iterations. In Fig. 7, the fitness value versus the number of iterations is demonstrated for the HPSSO algorithm. Power values for different iterations of the SSO and HPSSO algorithms are given in Table 2. As seen in Table 2, as the number of iterations is increased in SSO algorithm, the power values of the solar power plant and wind turbine are increased. The best results in the HPSSO algorithm are achievable for $n_{iteration} = 60$.

Table 2. Comparison of iteration values of SSO and HPSSO

	Solar Power Plant	Wind Turbine	Diesel Generator
$n_{iteration_{SSO}} = 100$	4708.24 kW	2355.65 kW	3076.029 kW
$n_{iteration_{HPSSO}} = 100$	3594 kW	2294.029 kW	3826.79 kW
$n_{iteration_{SSO}} = 250$	4625.96 kW	2587.776 kW	3162.65 kW
$n_{iteration_{HPSSO}} = 250$	3776.21 kW	2464.21 kW	3675.81 kW
$n_{iteration_{SSO}} = 400$	4988.17 kW	2808.22 kW	2692.87 kW
$n_{iteration_{HPSSO}} = 400$	3219.8 kW	2173.37 kW	4253.42 kW

4.3. Comparison of SSO and HPSSO in terms of population

Three different population number values were selected as 20, 60, and 100 for the SSO and HPSSO algorithms. Each algorithm was run 30 times and mean values were taken. Table 1 presents the problem parameters. The maximum number of iterations is selected as 400.

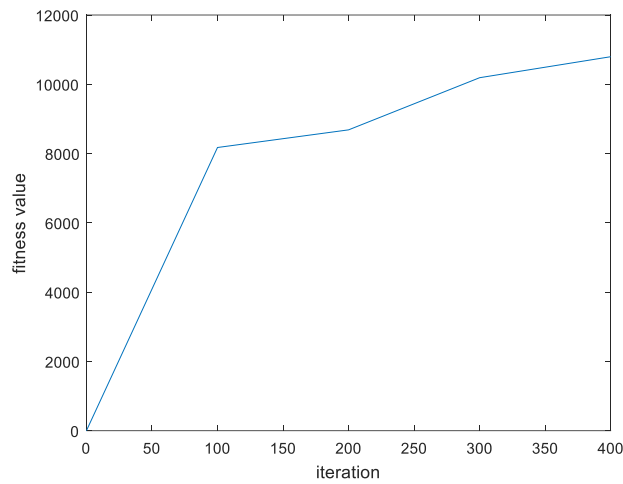


Figure 9. The fitness value for $n_{population} = 20$ in the SSO algorithm

When the number of population of SSO algorithm is selected as 20; the obtained power values for the solar power plant, the wind turbine, and the diesel generator are 5948.833 kW, 2502.78 kW, and 2218.05 kW respectively. Fig. 8 shows the fitness value versus the iterations for the SSO algorithm.

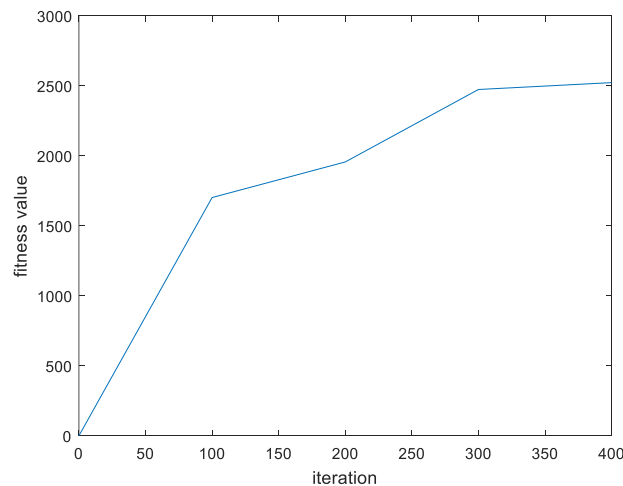


Figure 10. The fitness value changes for a maximum number of population 60 in the

SSO algorithm

The values of 6193.61 kW, 2761.58 kW, and 1861.651 kW have been obtained for optimized power values for the solar power plant, the wind turbine, and the diesel generator with SSO algorithm using 60 search agents. Fig. 9 shows the fitness value and the number of iterations for $n_{population} = 60$.

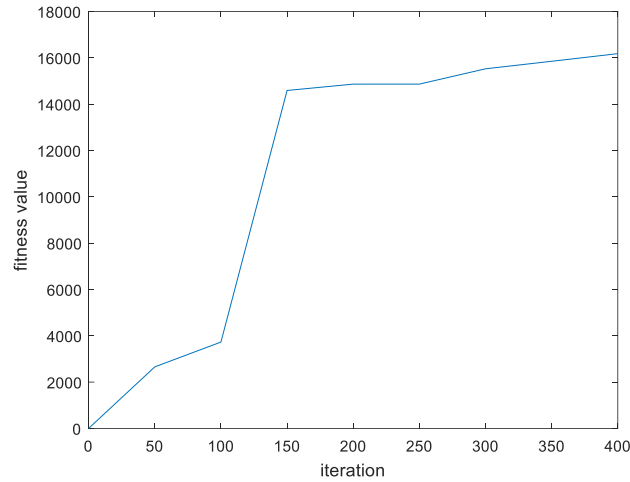


Figure 11. The fitness value change with 100 individuals in the SSO algorithm

When the SSO algorithm is executed with $n_{population} = 100$; the values of 4988.17 kW, 2807.22 kW, 2692.87 kW have been obtained for the power values of the solar power plant, the wind turbine, and the diesel generator respectively. Fig. 10 shows the fitness value and the number of iterations for $n_{population} = 100$.

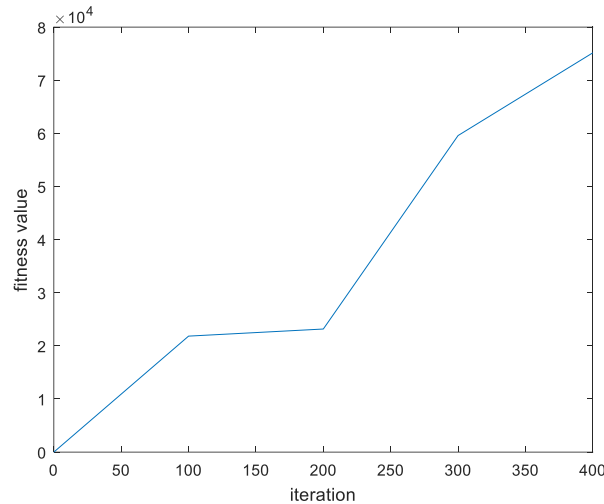


Figure 12. The fitness values change with 20 individuals in the HPSSO algorithm

When the HPSSO algorithm is run with 20 individuals; the optimized power values for the solar power plant, the wind turbine, and the diesel generator are 2649 kW, 1959.511 kW, and 4947.75 kW are obtained respectively. Fig. 11 shows the fitness value and the number of iterations for $n_{population} = 20$.

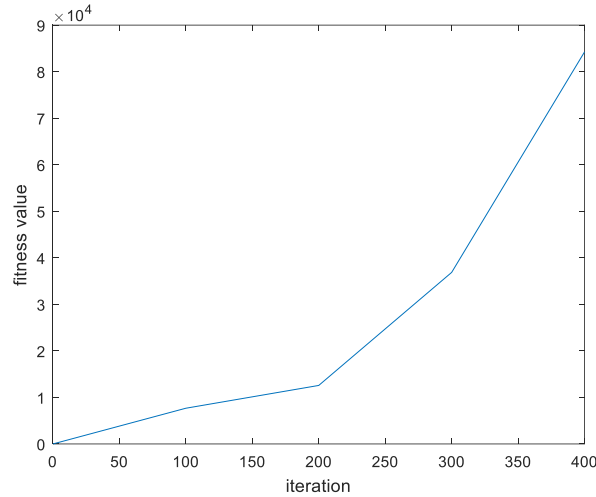


Figure 13. The fitness values change in the HPSSO algorithm with 60 individuals

When the HPSSO algorithm is run with 60 individuals; the values of 2577.43 kW, 1641.04 kW, and 5375.14 kW have been obtained for the optimized power values of the solar power plant, the wind turbine, and the diesel generator. Fig. 12 shows the fitness value and the number of iterations for $n_{population} = 60$.

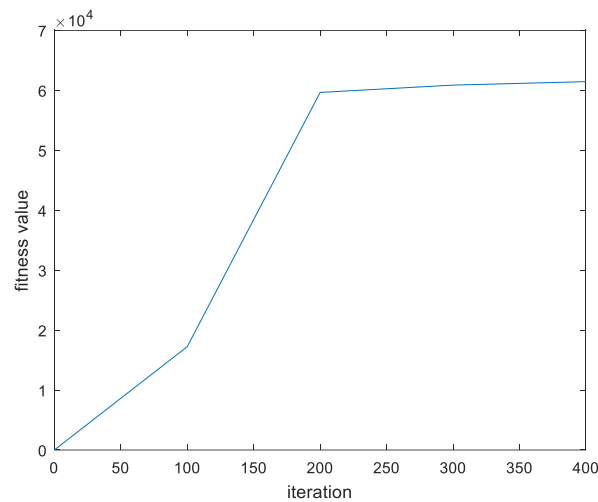


Figure 14. The fitness value change with 100 individuals in the HPSSO algorithm

When the HPSSO algorithm is executed with 100 individuals; the values of the power values for the solar power plant, the wind turbine, and the diesel generator are 3219.8 kW, 2173.37 kW, and 4253.42 kW are obtained. Fig. 13 shows the fitness value and the number of iterations for $n_{population} = 100$.

The power values for the different population size of the SSO and HPSSO algorithm are given in Table 3. The HPSSO algorithm yields better results as the population size increases. The SSO algorithm achieved good results for all population values However, this algorithm has given the best results for $n_{population} = 60$.

Table 3. Comparison of population values of SSO and HPSSO

	Solar Power Plant	Wind Turbine	Diesel Generator
$n_{population\ SSO} = 20$	5948.83kW	2502.78kW	2218.05kW
$n_{population\ HPSSO} = 20$	2649kW	1959.51kW	4947.75kW
$n_{population\ SSO} = 60$	6193.61kW	2761.58kW	1861.651kW
$n_{population\ HPSSO} = 60$	2577.43kW	1641.04kW	5375.14kW
$n_{population\ SSO} = 100$	4988.17kW	2807.22kW	2692.87kW
$n_{population\ HPSSO} = 100$	3219.8kW	2173.37kW	4253.42kW

5. Conclusions

In this study two new metaheuristic algorithms, namely SSO and HPSSO, have been designed as solution search methods for the problem reducing the emission, increasing reliability, and optimizing the sizing of the microgrid for the first time. A microgrid consisting of 8 MW solar panel, 4.5 MW wind turbine, 15 MW diesel generator, and 4 MW battery has been taken into consideration. The microgrid feeds a 10MW network. In Turkey, the inductive reactive penalty limit is 33% for facilities with a connection power of less than 50KVA. In our system, there is a residence as a load and this ratio is not exceeded and only active power is taken into consideration and all calculations are made accordingly.

The results have been obtained by running SSO and HPSSO algorithms on three different iterations as 100, 250, and 400. The SSO algorithm has given the best solution with 400 iterations. The best results of 4988.17 kW, 2808.22 kW, and 2692.87 kW for the solar panel, wind turbine, and diesel generator respectively have been achieved. The best results have been obtained from the HPSSO algorithm for 250 iterations. These obtained results for the solar panel, wind turbine, and diesel generator are 3776.21 kW, 2464.21 kW, and 3675.81 kW respectively. Comparing SSO and HPSSO in terms of different iteration values, SSO algorithm has been found to optimize energy resources better.

The powers of the solar power plant, wind turbine, and diesel generator are also aimed to be optimized by the SSO and the HPSSO with three different population sizes like 20, 60, and 100. The SSO algorithm obtained optimal results when the population size has been set at 60. These results are 6193.61 kW, 2761.58 kW and 1861.651 kW for the solar power plant, wind turbine, and diesel generator respectively. In the HPSSO algorithm, when the number of population is increased, and the yield is also increased. This algorithm has found the results of 3219.8 kW, 2173.37 kW, and 4253.42 kW for the solar power plant, wind turbine, and diesel generator using 100 individuals. The SSO algorithm yielded better results with less population when compared with HPSSO. This also simplifies the process and shortens the process time.

Novel and efficient metaheuristic algorithms are still being proposed for efficient results for many types of problems. Their new, adaptive, hybrid versions with optimized parameters may be used for the optimizing of the microgrids. Furthermore, this type of optimization, in fact, contains many objectives and thus efficient real multi-objective and many-objective versions of these metaheuristic algorithms may also be designed for these types of problems. SSO and HPSSO are two new metaheuristic algorithms. These algorithms have been applied by using the different parameters. Both algorithms have shown very good significant improvement. These algorithms can improve the solution quality of many complex problems. They can also be applied to different engineering problems.

References

- [1] Wang, Z., *et al.*, Intelligent Multi-Agent Control for Integrated Building and Micro-Grid Systems. *In Innovative Smart Grid Technologies (ISGT), 2011 IEEE PES, 2011*, pp.1-7.



- [2] Aziza, M., & Walling, F., Multi-objective Particle Swarm Optimization of Hybrid Micro-Grid System: A Case Study in Sweden, *Energy*, 2017, Vol.123, pp. 108-118.
- [3] Fossati, J. P., *et al.*, A Method for Optimal Sizing Energy Storage Systems for Microgrids. *Renewable Energy*, 2015, Vol.77, pp.539-549.
- [4] Bevrani, H., *et al.*, Intelligent Frequency Control in an AC Microgrid: Online PSO-Based Fuzzy Tuning Approach. *IEEE Transactions on Smart Grid*, 2012, Vol. 3(4), 1935-1944.
- [5] Chen, Y. K., *et al.*, Design and Implementation of Energy Management System with Fuzzy Control for DC Microgrid Systems. *IEEE Transactions on Power Electronics*, 2013, Vol. 28(4), 1563-1570.
- [6] Seung, C., *et al.*, Agent based Particle Swarm Optimization for Load Frequency Control of Distribution Grid, *In Universities Power Engineering Conference (UPEC), 2012 47th International*, 2012, pp. 1-6.
- [7] Eilaghi, S. F., *et al.*, Optimal Voltage Unbalance Compensation in a Microgrid Using PSO Algorithm. *In Power India International Conference (PIICON), 2016 IEEE 7th*, 2016, pp.1-6
- [8] Yazdani, M., & Jolai, F., Lion Optimization Algorithm (LOA): A Nature-inspired Metaheuristic algorithm. *Journal of Computational Design and Engineering*, 2016, Vol. 3(1): pp.24-36.
- [9] Gandomi, A. H., *et al.*, Mixed Variable Structural Optimization Using Firefly Algorithm, *Computers & Structures*, 2011, Vol. 89(23-24), pp. 2325-2336.
- [10] Gandomi, A. H., & Alavi, A. H., Krill Herd: A New Bio-inspired Optimization Algorithm. *Communications in Nonlinear Science and Numerical Simulation*, 2012, Vol. 17(12), pp. 4831-4845.
- [11] Revathi, K., & Krishnamoorthy, N., The Performance Analysis of Swallow Swarm Optimization Algorithm, *2015 2nd International Conference on IEEE*, 2015, pp. 558-562.
- [12] Bouzidi, S., & Riffi, M. E., Discrete Swallow Swarm Optimization Algorithm for Travelling Salesman Problem, *In Proceedings of the 2017 International Conference on Smart Digital Environment*, 2017, pp. 80-84.
- [13] Neshat, M., *et al.*, Swallow Swarm Optimization Algorithm: A New Method to Optimization, *Neural Computing and Applications*, 2013, Vol. 23(2), pp.429-454.
- [14] Kaveh, A., *et al.*, Hybrid PSO and SSO Algorithm for Truss Layout and Size Optimization Considering Dynamic Constraints, *Structural Engineering and Mechanics*, 2015, Vol. 54(3), pp. 453-474.
- [15] Sam C., & Ali, A., A., 2015. Identification of Crack in a Cantilever Beam using Improved PSO Algorithm, *International Journal for Innovative Research in Science & Technology*, 2015, Vol.1(11), pp. 454- 461.